University of California
Santa Barbara

Modeling Complex Electrokinetic Nanofluidic Systems

A dissertation submitted in partial satisfaction
of the requirements for the degree

Doctor of Philosophy
in
Mechanical Engineering

by

Christopher Craig McCallum

Committee in charge:

Professor Sumita Pennathur, Chair
Dr. Dirk Gillespie
Professor Carl Meinhart
Professor Eckart Meiburg

June 2017

The Dissertation of Christopher Craig McCallum is approved.

Dr. Dirk Gillespie

Professor Carl Meinhart

Professor Eckart Meiburg

Professor Sumita Pennathur, Committee Chair

May 2017

Modeling Complex Electrokinetic Nanofluidic Systems

Christopher Craig McCallum

For my family

Acknowledgements

First, I would like to thank my advisor, Professor Sumita Pennathur for her inexhaustible support and encouragement. I have truly enjoyed the past five years and have had the great privilege to work with Prof. Pennathur and many other fantastic scientists in the lab. Furthermore, I would like to thank Dr. Dirk Gillespie for his expertise and advice. It has been a pleasure to have had the opportunity to collaborate with such an incredible scientist.

I would like to also thank my Ph.D. committee members, Professor Carl Meinhart and Professor Eckart Meiburg. Thank you for spending time to provide support and useful comments and questions to allow me to better fine-tune my research plan and guide my Ph.D.

I would like to of course thank all members of the UCSB Nanolab with whom I have had the pleasure of working with over the past five years. Thank you to Maria, Tom, Travis, Tyler, Elijah, Adam, Neeraja, Alex R., Sameh, Kjeld, Pete, Logan, Seth, Mike, Jin, Pascal, Karen, Alex D., Sean, Charlie, Xavier, Alex C., Tim, Chris, Kaela, Amanda, Kristen, Madelein, Trevor, Andrew, Kristi, Meron, Sam, Josh, Marco, Tylar, Renhao, Bethany, Robbie, Ben, John, and Yanxian. I am grateful for the engaging discussion and camaraderie.

I would also like to thank all of my friends and fellow graduate students for helping to provide an appropriate work-life balance. I am truly grateful for the welcoming and collaborative environment of UCSB.

Lastly, I would like to thank Amanda and my family for their endless encouragement. Grad school is not always easy, and I am truly appreciative that I can always count on you in tough times.

Curriculum Vitæ
Christopher Craig McCallum

Education

June 2017	Ph.D. in Mechanical Engineering, University of California, Santa Barbara.
May 2012	B.S. in Mechanical Engineering, University of Wisconsin, Madison

Publications

McCallum, C., Pennathur, S., Gillespie, D. (2017). Two-Dimensional Electric Double Layer Structure with Heterogeneous Surface Charge. Langmuir, (just accepted)

McCallum, C., and Pennathur, S. (2016). Accounting for electric double layer and pressure gradient-induced dispersion effects in microfluidic current monitoring. Microfluidics and Nanofluidics, 20(1), 13.

Loessberg-Zahl, J., Janssen, K. G. H., McCallum, C., Gillespie, D., and Pennathur, S. (2016). (Almost) Stationary Isotachophoretic Concentration Boundary in a Nanofluidic Channel Using Charge Inversion. Analytical Chemistry, 88(12), 6145-6150.

Crisalli, P., McCallum, C., and Pennathur, S. (2015). Label free detection of nucleic acids by modulating nanochannel surfaces. Chem. Commun., 51(12), 2335-2338.

Wynne, T. M., McCallum, C., Del Bonis-O'Donnell, J. T., Crisalli, P., and Pennathur, S. (2015). Hybridization Thermodynamics of DNA Oligonucleotides during Microchip Capillary Electrophoresis. Analytical Chemistry, 87(5), 2811-2818.

Published Abstracts and Presentations

McCallum, C., Lin, Y., de Rutte, J., Chen, I., Pennathur, S. (2016). Confinement Effects on Non-Equilibrium DNA Hybridization in Micro and Nanofluidic Channels. Presented at The 20th International Conference on Miniaturized Systems for Chemistry and Life Sciences (muTAS 2016). Dublin, Ireland, October 9-13, 2016.

McCallum, C., Gillespie, D., Pennathur, S. Accounting for Finite Size of Ions in Nanofluidic Channels Using Density Functional Theory. Presented at APS Division of Fluid Dynamics, Vol 61, 20. Portland, Oregon, November 20-22, 2016.

McCallum, C., and Pennathur, S. (2015). Modelling nanofluidic field amplified sample stacking with inhomogeneous surface charge. Presented at APS Division of Fluid Dynamics, Vol

60, 21. Boston, MA, November 22-24, 2015.

McCallum, C. and Pennathur, S. Accounting for electric double layer and pressure-gradient induced dispersion effects in microfluidic current monitoring. Presented at 89th ACS Colloid and Surface Science Symposium, Carnegie Mellon University, Pittsburg, PA, June 15-17, 2015.

McCallum, C. and Pennathur, S. Accounting for electric double layer and pressure-gradient induced dispersion effects in microfluidic current monitoring. 2015 SoCal Micro and Nanofluidics Symposium, Huntington Library, San Marino, CA, June 11, 2015.

McCallum, C., Gillespie, D. and Pennathur, S. Accounting for Finite Size of Ions in Nanofluidic Channels. Presented at 2014 SoCal Micro and Nanofluidics Symposium, Getty Villa, Los Angeles, CA, June 16, 2014.

Relevant Skills
Matlab, Comsol Multiphysics, Mathematica, Data Analysis, LaTeX

Relevant Websites
https://www.linkedin.com/in/chris-mccallum-b2593742/
https://engineering.ucsb.edu/ nanolab/

Work Experience

Sept 2012 - June 2017	Graduate Student Researcher, University of California, Santa Barbara.
Sept 2012 - June 2015	Teaching Assistant, University of California, Santa Barbara (Dynamics, Fluid Mechanics, Thermosciences, and Structures (FEA)).
May 2011 - Sept 2012	Undergraduate Research Assistant, University of Wisconsin, Madison

Editorial And Reviewing Duties

Sept 1-2, 2016	Chair, SoCal Micro and Nanofluidics Symposium, UC Irvine, Applied Innovation, Irvine, CA
	Journal article reviewer:
2015 - 2017	Analytical Chemistry
2016 - 2017	American Institute of Physics (AIP) Advances
2015 - 2017	Microfluidics and Nanofluidics

Teaching Experience

Feb 2017	Guest Lecturer, University of California, Santa Barbara. Physics of Transducers - Electrokinetics
2012 - 2015	Teaching Assistant, University of California, Santa Barbara

Awards and Honors

2014	UCSB Dept of Mechanical Engineering Summer 2014 Fellowship
2012	UCSB Dept of Mechanical Engineering Departmental Fellowship
2012	Holbrook Fellowship - UCSB
2010	Faustin Prinz Undergradute Research Fellowship and Gary and Marlene Borman Scholarship - UW
2010-2012	UW Leadership - Polygon Representative for Pi Tau Sigma, honor society
March 29, 2007	Eagle Scout, Glacier's Edge Council, Madison, WI

Abstract

Modeling Complex Electrokinetic Nanofluidic Systems

by

Christopher Craig McCallum

The electrical double layer (EDL) nano-structure at the interface between electrolytes and charged surfaces dominates the performance of a myriad of electrokinetic and electrochemical processes. A complete understanding of the EDL nano-structure allows for a predictive tool for various systems such as supercapacitors, desalination, and nano-particle manipulation. My work involves developing theoretical models to elucidate the nano-structure of the EDL and the consequent effects on fluid flow and species transport in such systems. These include models explaining dispersion of ions in channels with thick EDLs, surface-charge-based ion conductivity changes, nanofluidic-based DNA hybridization, nanofluidic isotachophoresis, charge inversion due to large ions, and nanofluidic systems with heterogeneous surface charges. Collectively, these studies have enriched our understanding of complex electrokinetic nanochannel transport.

First, I describe a model for the EDL in nanofluidic channels, showing experimentally validated theoretical regimes where dispersion and/or significant EDL size might affect experimental results, as well as methods to account for these effects. Understanding these effects is essential to accurately interpret experiments as well as design of future experiments and subsequent applications. This model can further explain other micro- and nanoscale electrokinetic transport physics. For example, 1) this theory can explain nanochannel conductivity changes due to changes in surface charge, 2) accounting for reaction terms, it can accurately model non-equilibrium DNA hybridization as well as the effect of nano-confinement on such hybridization in electrokinetic capillary electrophoresis-based systems, 3) it can predict an

isotachophoretic-like standing front in nanochannels with surface-charge-inverting complex ionic species that induce fluid flow reversal, and 4) it can describe behavior with heterogeneous surface charge.

To explain the behavior of nanofluidic systems with heterogeneous surface charge and complex ionic species, I refined the model by accounting for hard-sphere ion size and more complex near-field screening effects using classical Density Functional Theory. I conducted a theoretical study to explore heterogeneous surface charge in nanochannels with embedded, addressable electrodes that allow us to fully probe EDL structure. I developed a more complete EDL model and performed a systematic theoretical study of EDL nano-structure by varying ion diameter, valence, and concentration, as well as surface charge in order to elucidate EDL nano-structure, fluid flow, and species transport in nanochannels. Thus far we have preliminary model validation using custom-fabricated nanochannels with complex ions, and further experiments will both interpret nanochannel physics through theory as well as improve the model via experimental feedback, overall enabling a more complete predictive theory for future experimental and application design.

Contents

List of Figures

List of Tables

Chapter 1

Transport in Electrokinetic Nanofluidic Systems

The electrical double layer (EDL) nano-structure at the interface between electrolytes and charged surfaces largely determines the performance of a myriad of electrokinetic and electrochemical processes, including fuel cells, batteries, biologically-relevant ion-selective channels, supercapacitors, and desalination. Moreso, while planar, impermeable, and uniformly charged walls have been predominantly studied for these applications, heterogeneous surfaces are of notable interest because many of the applications require surfaces that can be tuned and exploited for ion manipulation. For example, researchers have built heterogeneous wall charge systems to finely manipulate electrokinetic devices to enhance micromixing [8] and mimic biological nanopores for single molecule detection [9] [10] [11]. Therefore, a complete understanding of the EDL nano-structure as well as fluid flow at heterogeneously-charged surfaces would allow for a robust predictive tool to drive experiments, as well as, ultimately, superior device development and characterization. In this chapter, I will first introduce the EDL and theories used to predict the structure, after which I will introduce electrokinetic transport, with emphasis on electroosmotic flow (EOF) and challenges of nanoflu-

idic transport.

1.1 Background

1.1.1 Electric Double Layers

In systems with charged surfaces, counterions are attracted to the surface, creating a region of excess counterions called the electric double layer (EDL). For example, in a silica or PDMS nanochannel, walls are negatively charged, attracting positive counterions to the wall as shown in Figure 1.1. Electrokinetic systems, the behavior of which is governed by this EDL structure, have been studied since the 1800's by Reuss [12], motivated initially by the interaction between colloidal particles in aqueous solution and applied electric fields. This motion of particles under and applied field is called electrophoresis. Further study investigated electroosmosis, bulk fluid motion induced by an applied potential, which motivated EDL theory. Gouy [13] and Chapman [14] independently explored EDL structure, which set up the so-called Poisson-Boltzmann equation used ubiquitously in the field. Debye and Huckel linearized this formulation [15], with initial improvement attempts in the point-wise continuum approximation performed by Stern [16] and Bikerman [17], as well as charge asymmetry improvements by Grahame [18]. Although the Poisson-Boltzmann formulation lacks applicability at high surface charge or for size-asymmetric ionic species, its overall efficacy is well-established and ubiquitous in contemporary electrokinetics.

The Poisson-Boltzmann Model of the EDL

For dilute, size- and charge-symmetric ionic species, the composition of the EDL is governed by a balance between electromigration and diffusion of the ions, for which a continuum approximation suffices. Specifically, for a system in chemical equilibrium the electromigrative

and diffusive fluxes balance,

$$0 = -\rho_i \nu_i z_i \nabla\psi - D_i \nabla\rho_i, \tag{1.1}$$

where ρ_i is the concentration of species i, ν_i is the mobility ($\nu_i = \frac{D_i z_i e_0}{kT}$, where e_0 is the elementary charge, k is the Boltzmann constant, and T is the system temperature), z_i is the valence, ψ is the transverse electrostatic potential, and D_i is the species' diffusivity. This equation can be solved for the one-dimensional concentration away from a single charged surface yielding a Boltzmann distribution:

$$\rho_i = \rho_i^{\text{bath}} \exp\left(-\frac{z_i e_0 \psi(z)}{kT}\right), \tag{1.2}$$

where ρ_i^{bath} is the species concentration far from the wall ($\rho_i(z) \to \rho_i^{\text{bath}}$, and $\psi \to 0$ as $y \to \infty$).

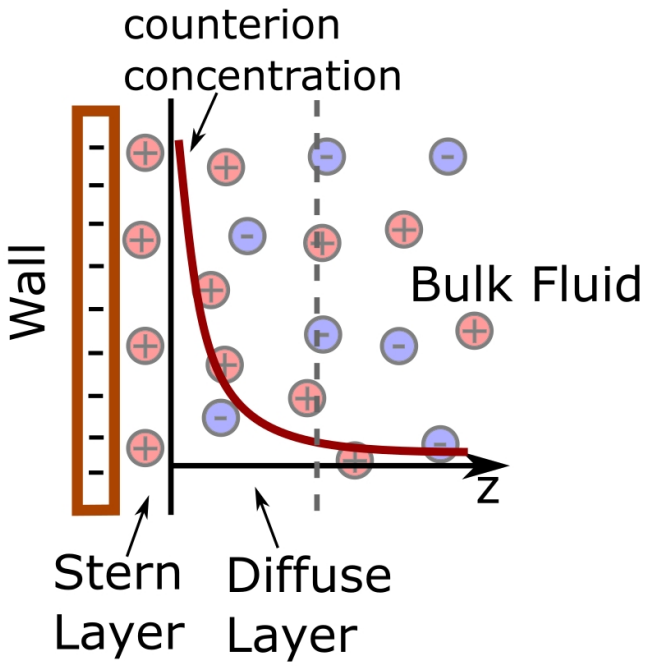

Figure 1.1: Different regions at the solid-liquid interface with the Gouy-Chapman-Stern model. Immediately next to the wall resides a layer of immobile ions (called the Stern layer), after which is the diffuse layer of excess counterions, and the bulk, neutral fluid far from the wall.

The electrostatic potential of the system is determined from Gauss' theorem:

$$\epsilon_0 \epsilon_r \nabla^2 \psi = -\rho_E, \tag{1.3}$$

where ϵ_0 is the vacuum permittivity, ϵ_r is the relative permittivity of the solution in the channel, and ρ_E is the volume charge density ($\rho_E = \sum_i^N z_i e_0 \rho_i$). A commonly used theory allows for an immobile layer of ions next to the wall, the Stern layer, after which a diffuse layer exists, followed by bulk fluid as shown in Figure 1.1. Combining Equations 1.2 and 1.3, we can write the non-linear Poisson-Boltzmann equation to solve for both ion concentration and electrostatic potential:

$$-\epsilon_0 \epsilon_r \nabla^2 \psi = e_0 \sum_i^N z_i \rho_i^{\text{bath}} exp\left(-\frac{z_i e_0 \psi}{k_B T}\right) + \sigma \delta(z), \tag{1.4}$$

where σ is the surface charge of the wall, and δ is the Dirac delta function. The characteristic length-scale of the EDL is the Debye length, λ_D,

$$\lambda_D = \left(\frac{\epsilon_0 \epsilon_r kT}{e_0^2 \sum_i^N z_i^2 \rho_i^{\text{bath}}}\right)^{1/2} \tag{1.5}$$

and is determined by linearizing Equation 1.4. Notably, the Debye length, generally $1 - 100$ nm, scales with $(\rho_i^{bath})^{-1/2}$.

The Poisson-Boltzmann equation is a non-linear ODE and can be solved with ease using a finite difference numerical approach. While it remains numerically inexpensive and straightforward to solve, the solution produced is only valid in the limit of dilute species and low surface charge because of the continuum nature of the setup. Ions have finite size, and, therefore, more accurate theories have been developed to account for finite ion size as well as more complex electrostatic effects.

Theories That Account For Finite Size and Near-Field Electrostatics

Recently, there has been study at the limit of Poisson-Boltzmann at high concentration and high surface charge when ion size effects cannot be neglected, thus requiring a more complete theory. Potentially applicable theories include Monte Carlo (MC) [19] [20] or Molecular Dynamics (MD) simulations [21] [22] [23] [24], Density Functional Theory calculations [25] [26] [27] [28]), strongly-correlated liquid theory (SCL) [29], and certain modified Poisson-Boltzmann methods [30] [31] [32] [33] [34]. Density functional theory is a particularly useful and efficient means of exploring nanofluidic electrokinetics because of the low computational cost and high accuracy relative to MC simulations [35] [36].

Density Functional Theory

Density functional theory is a continuum model that accounts for finite ion size and near-field screening effects by creating weighted densities, and remains as accurate, yet far more computationally efficient, relative to MC and MD. All continuum theories give each species a chemical potential of the form:

$$\mu_i(\mathbf{r}) = kT \ln\left(\Lambda_i^3 \rho_i(\mathbf{r})\right) + \mu_i^{\text{ex}}(\mathbf{r}) + z_i e_0 \psi(\mathbf{r}) + \mu_i^{\text{ext}}(\mathbf{r}), \tag{1.6}$$

where Λ_i is the thermal de Broglie wavelength, μ_i^{ex} is the excess chemical potential (which is made up the hard-sphere and screening components ($\mu_i^{\text{ex}} = \mu_i^{\text{HS}} + \mu_i^{\text{SC}}$), and μ_i^{ext} is any external potential (such as a hard, charged wall, giving a large penalty for approaching the wall too closely). The inhomogeneous system of interest is in chemical equilibrium with a homogeneous, electroneutral bath fluid ($\mu_i^{\text{bath}} = \mu_i(\mathbf{r})$), meaning the species' density can be

written:

$$\rho_i(\mathbf{r}) = \rho_i^{\text{bath}} \exp\left(-\frac{\Delta\mu_i^{\text{ex}}\left[\{\rho_k(\mathbf{r})\};\mathbf{r}\right]}{kT}\right) \cdot \exp\left(-\frac{z_i e_0 \psi\left[\{\rho_k(\mathbf{r})\};\mathbf{r}\right]}{kT}\right) \cdot \exp\left(-\frac{\mu_i^{\text{ext}}(\mathbf{r})}{kT}\right), \tag{1.7}$$

for which the braces indicate that the excess potentials are functionals of the density, and where $\Delta\mu_i^{\text{ex}} = \Delta\mu_i^{\text{HS}} + \Delta\mu_i^{\text{SC}}$ is the difference in excess chemical potential between the system and the bath. The resulting fixed point equation can be solved via optimized Picard iteration quite efficiently [37].

Furthermore, DFT accurately calculates the ensemble average ion density and electrostatic potential profiles for a system in chemical equilibrium with a bath by taking into account hard-sphere (HS) and screening (SC) excess free energy components. Given their finite size, ion cannot overlap each other or the hard wall, and the HS contribution accounts for the pressure work necessary to insert a hard sphere. The SC component accounts for electrostatic correlations beyond the mean-field potential of inserting an ion within a screening length of other ions. Therefore, both components check for other ions within a radius or a screening length, thereby leading to convolutions as in Equation 1.8, which are solved efficiently via Fast Fourier Transforms. Specifically, we use the White Bear functional [26] for the HS component and the functionalized Mean Spherical Approximation (fMSA) [7] for the SC component.

Since the excess chemical potentials are functionals of the densities, we must compute the densities numerically. The excess chemical potentials are calculated via convolutions, which are, in general,

$$\int f(\mathbf{r}')\omega(\mathbf{r}-\mathbf{r}')\mathbf{dr}', \tag{1.8}$$

where $f(\mathbf{r}')$ is either the true ρ_i or weighted ion density (as in Equation 1.13). The DFT weight functions [26] [7] are

$$\omega_i^{(2)}(\mathbf{r}) = \delta\left(|\mathbf{r}| - R\right) \tag{1.9}$$

$$\omega_i^{(3)}(\mathbf{r}) = \theta\left(R - |\mathbf{r}|\right) \tag{1.10}$$

$$\omega_i^{(\mathrm{V2})}(\mathbf{r}) = \frac{\mathbf{r}}{|\mathbf{r}|}\delta\left(|\mathbf{r}| - R\right) \tag{1.11}$$

$$\omega_i^{(\mathrm{SC})}(\mathbf{r}) = \frac{1}{|\mathbf{r}|}\left(|\mathbf{r}| - \lambda_{ij}\right)^2 \cdot \theta\left(R_{ij} - |\mathbf{r}|\right), \tag{1.12}$$

where δ denotes the Dirac delta function, θ denotes the Heaviside function, and R is the radius of interest. This radius is either R_i (the radius of ion species i) or the screening length, $\lambda_i = R_i + \frac{1}{2\Gamma}$, where Γ is the screening parameter [27], which, in the limit of point charges, is equal to $\kappa/2$, where κ is the Debye-Huckel screening parameter, and where $\lambda_{ij} = \lambda_i + \lambda_j$ and $R_{ij} = R_i + R_j$.

The hard-sphere weighted densities, n_α, are found via convolution

$$n_\alpha(\mathbf{r}) = \sum_i \int \rho_i(\mathbf{r})\omega_i^{(\alpha)}(\mathbf{r} - \mathbf{r}')d^3\mathbf{r}', \tag{1.13}$$

which are then convolved again to give the components of the excess free energy functional. The most accurate hard-sphere functional is the White Bear functional [26], which builds on earlier Fundamental Measure Theory [38]. Practically, the weight functions give the ions surface area ($\omega_i^{(2)}$) and volume ($\omega_i^{(3)}$), which ultimately determine the energy associated with inserting a single hard-sphere into an inhomogeneous arrangement of hard-spheres. Moreso, the weighted density n_3 corresponds to the packing fraction of the fluid.

The screening component uses a newly developed electrostatic functional that builds on the Mean Spherical Approximation [39] by formulating a weighted averaged density-based functional and screening parameter [7]. This method improves on the bulk fluid method by

allowing the screening parameter to vary with position, while also improving on the computational expense of the RFD functional [28]. This screening functional accounts for short-range electrostatic correlations by determining the potential associated with overlapped charged shells. The shell size is determined via Newton iterations, and, in this formulation, varies with averaged density, and hence, position.

The two components, hard-sphere and screening, determine the excess free energy, and thus contribute to the final density profiles. These ion density and electrostatic potential are the primary terms used to quantify the electric double layer, and, ultimately, fluid flow in electrokinetic systems.

1.2 Electrokinetic Transport

Fluid flow at the micro- and nanoscale (i.e., low Reynolds number) is dominated by viscous forces, making it difficult to drive fluids with pressure. Because the required pressure to drive flow scales with channel height to the fourth power, pressure becomes a less effective means of transport for sub-microscale systems. However, electrokinetic (EK) flow, fluid flow induced by the application of an electric field, serves as an effective substitute at this scale since the flow rate depends only on the applied electric field strength.

The field of electrokinetics has seen a myriad of applications over the last hundred years [13] [14] [15] [17] [18], primarily because it has become the workhorse tool for separations of biological systems, as in capillary electrophoresis [40] [41] [42], desalination and energy technology. These technologies take advantage of microfluidic transport, although recently nanofluidics has shown considerable potential because the higher surface area to volume ratio enables enhanced sensitivity. Furthermore, nanofluidic platforms enable faster throughput and smaller sample volumes, and devices can be easily integrated into hand-held platforms for extra-laboratory applications, such as biological diagnostics [43]. Moreso, nanochannels with

thick EDLs relative to channel height [44] [45], can be exploited to, for example, perform separations at the nanoscale [46] or to concentrate sample as in Field Amplified Sample Stacking (FASS) [47] [48], isotachophoresis (ITP) [49] [50], ion concentration polarization (ICP) [51], or isoelectric focusing [52], among other unique phenomena.

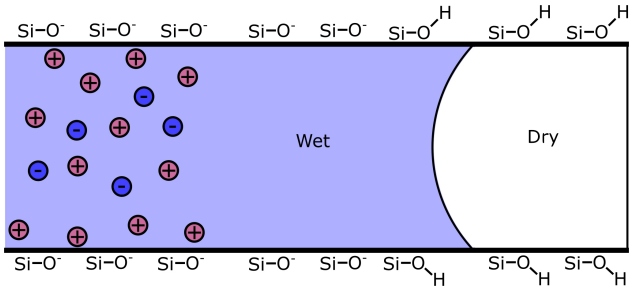

Figure 1.2: Surface charge in silica channels is due to the deprotonation of silanol groups. As the fluid enters the channel, the surface releases protons, acquiring negative surface charge, thus attracting the positive to the surface. [1]

1.2.1 Electroosmotic Flow

Once the electrostatic potential and ion density distributions are found, the electroosmotic flow (EOF) can be obtained from the Navier-Stokes equations,

$$0 = -\nabla p + \mu\nabla^2 u - \rho_E \nabla\Phi \tag{1.14}$$

$$0 = \nabla \cdot u \tag{1.15}$$

where p is the pressure, μ is the viscosity, u is the velocity, and Φ is the total electrostatic potential, which can be decompose into axial x direction and transverse z direction components,

$$\Phi = \psi(z) + V(x), \tag{1.16}$$

where $V(x)$ is the applied voltage through the channel and L is the channel length.

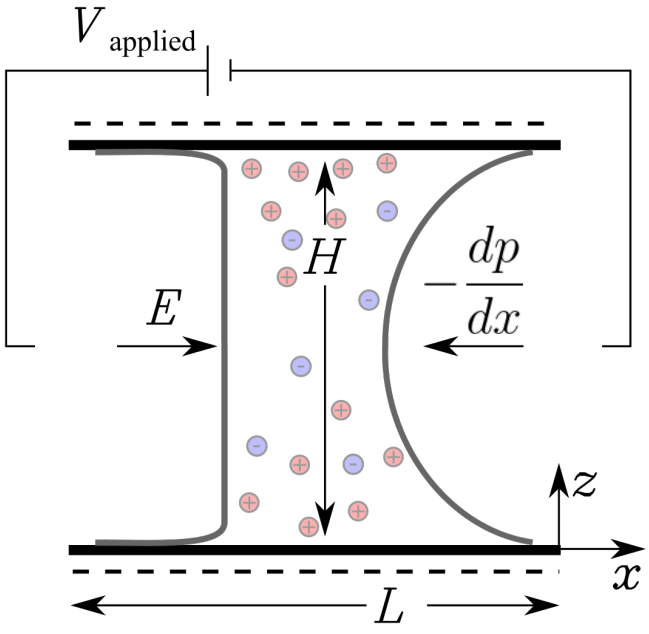

Figure 1.3: Schematic of electroosmotic flow (EOF) and pressure-driven flow (PDF) in a microfluidic device.

The resulting fluid flow distribution can be found as

$$u(z) = -\frac{1}{2\mu}\frac{\partial p}{\partial x} z\,(H - z) - \frac{\epsilon_0 \epsilon_r E \zeta}{\mu}\left(1 - \frac{\psi(z)}{\zeta}\right), \tag{1.17}$$

where the velocity is decoupled into pressure-driven and EOF velocities, where $\frac{\partial p}{\partial x}$ is the constant applied pressure gradient, H is the channel height, E is the applied electric field ($E = V_{\text{applied}}/L$), and ζ is the zeta potential (the electrostatic potential at the fluid slip plane) [53]. Qualitative differences of EOF in micro- and nanochannels are shown in Figure 1.4. When $\lambda_D \ll H$ as in microchannels, the EDL is negligible, and the resulting flow is a plug profile. However, if $\lambda_D \approx H$, as in nanochannels, the EDLs are finite and may overlap, resulting in deviation from the microfluidic plug flow.

As a practical example, species of the same mobility can be separated from one another if they have different charge by combining EOF and pressure-driven flow as shown in Figure 1.3. A more negatively-charged species will prefer the center of the channel, and thus move at a different mean speed than a species that can travel nearer to the wall [53]. Therefore, the two

species will inevitably separate from one another.

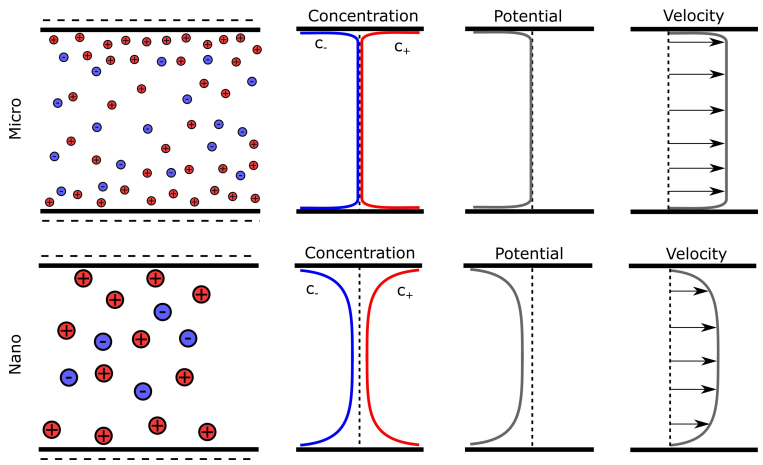

Figure 1.4: Difference in concentration, electrostatic potential, and velocity profiles for microchannels vs nanochannels.

1.2.2 Challenges at the Nanoscale

While electrokinetics serves well to transport fluid at the nanoscale, and the high surface area to volume ratio enables enhanced solution characterization sensitivity, macro-scale properties such as permittivity and viscosity changes, and in ultra-confined nanoslits, the ion-scale structure of the EDL can drastically change fluid transport. Furthermore, the continuum approximation of Navier-Stokes can break down at this scale. Thus, variation in macro-scale properties, as well as ion-scale structure must be acknowledged in order to accurately model the system.

Ion-scale EDL structure plays an increasingly important role as the size of the channel decreases [35]. Especially for channels smaller than 10 nm, high surface charge or high ionic strength will significantly affect device performance since two EDLs may overlap creating strong ion layering [36]. Additionally, non-continuum physics may substantially affect fluid flow and ion transport. Studies have shown that high local ion density can increase fluid viscosity and reduce ion diffusivity [54] [55] [56]. However, fluid flow in ultra-confined parallel-plate channels yields apparent viscosity very near to bulk values [57]. Therefore, even though

the continuum approximation may not necessarily hold, its use is quite valid for these geometries. Furthermore, slip length and slip velocity at the solid/electrolyte interface is governed primarily by molecular-scale roughness and interaction energies [58]. The slip length is not easily predicted, but it can be tuned to best match experiments and theory. Lastly, the apparent dielectric constant will decrease due to highly oriented water molecules in extended nanospaces and should be accounted for [59]. Overall, though, use of continuum EOF modeling in conjunction with Density Functional Theory calculations shows excellent agreement with more robust (yet computationally intensive) MD or MC simulations [35] [23] [7].

Additionally, EDL confinement effects as well as reservoir entrance and exit effects must be accounted for. EDL hydrodynamic and electrostatic effects can alter molecule conformation, shape, and function under confinement or even prevent molecules of interest from entering a nanochannel. pH gradients and concentration polarization can also develop quite easily, thus changing the electrolyte composition within the channel and affecting expected results. These are mentioned for completeness, although this work is primarily concerned with the structure of the EDL and its effect on the fluid flow profile.

As discussed, significant developments in modeling electrokinetic systems have enabled greatly-enhanced experimental understanding. These models are constantly tuned with the aid of new experimental results such that more complete theories can be used as predictive tools. This synergistic approach combining experiments and theory is ever-evolving. Much of the work explored was primarily experimental followed with a theoretical approach to better understand the system. Other work, however, is nearly all computational/theoretical with brief experimental confirmation or even purely theoretical with hopes for use as a predictive tool.

1.3 Thesis Outline

My thesis focuses on 3 major aspects of modeling complex electrokinetic nanofluidic systems:

1. Chapter 2 shows how theory and modeling can predict experimental phenomena, particularly regarding dispersion in current monitoring experiments. For this project, I performed both experiments and simulations, extracting useful parameters by matching the two.

2. Chapter 3 illustrates for three different projects that theory can greatly enhance our understanding of experiments. In all projects I performed simulations and aided in calculations to elucidate experimental results. I used theory to better understand nanochannel conductivity changes based on DNA-induced surface charge changes, DNA hybridization kinetics under non-equilibrium conditions in micro- and nanochannels, and isotachophoretic-like conditions in nanochannels with complex, charge inversion-inducing species.

3. Chapters 4 and 5 cover a theoretical investigation into electric double layer ion structure and fluid flow, respectively, at the planar interface between regions of different surface charge. I performed Density Functional Theory calculations to systematically probe the structure of the electric double layer and employed COMSOL to calculate the resulting fluid flow to aid in future experimental design. Additionally, Chapter 5 shows simulation results from a collaboration that uses the more computationally-accessible Poisson-Nernst-Planck to propose a sample pre-concentration technique in heterogeneous nanochannels. We hope that these results can be used to predictively to highlight potential experimental conditions that are worth exploring.

Chapter 2

Apply Voltage, Measure Current

An effective means of determining the flow rate and/or ζ-potential [60] in micro- and nanofluidic systems is the solution displacement method, also known as current monitoring (CM), when one solution in the channel is displaced by a different concentration, yielding a linear change in current versus time [61] [42].

Dissimilar solution concentrations and finite electric double layers (EDLs) cause deviations to typical current versus time, diminishing the utility of such a method. Current monitoring has been explored in microchannels for both low and high concentration ratio, γ. Zare et al [61] [40], Sze et al [42], and Driehorst et al [62] all utilize current monitoring to determine flow velocity and channel properties, focusing on $\gamma \sim 1$. Mampallil et al [63] and Lenzi et al [64] focus on cases in which γ is high; however, neither study properly accounts for diffusion and dispersion. Both diffusion and dispersion affect solute transport when γ is high, and will lead to erroneous estimates of ζ potential [63]. Situations of high γ are of high importance in the field, as explored by Bharadwaj and Santiago [47], Devasenathipathy et al [65], and Sustarich et al [48]. Furthermore, all analysis thus far has focused on microchannels, for which the EDL is thin. None have focused on the case in which the EDLs overlap considerably, such as in a nanochannel. In a nanochannel, the physics becomes more complicated because of

the non-uniform velocity profile, and, hence, the effect of EDL thickness on the time-varying species concentration and velocity in current monitoring has yet to be fully characterized in nanochannels.

In this chapter, I theoretically and experimentally investigate the effects of varying displacing/displaced electrolyte concentration ratios and channel height on the observed channel current and flow rate, as well as apparent dispersion, by simulating the time-dependent Stokes equation coupled with Poisson-Nernst-Planck and current conservation. Furthermore, the theory is validated with micro- and nanochannel experiments, showing a robust theoretical model that matches both micro- and nanochannel systems. I find that current monitoring in finite EDL nanochannel systems and small concentration ratios can be approximated with a simple function, predicting ζ-potential to within 10% even without *a priori* knowledge of channel surface charge. However, as concentrations become more dissimilar, dispersion due to induced pressure gradients greatly affects the shapes of the current monitoring curves. I show that typical microchannel and nanochannel experiments can easily span a wide range of dispersion regimes based on Peclet number, from pure axial diffusion to pure convective dispersion. I explain the shapes of the curves based on the regime of dispersion, and give practical guidelines for CM with high concentration ratios. [66]

2.1 Theory

The model assumes a two-dimensional channel bounded by two charged walls, an inlet, and outlet and is filled with a two species ionic solution. The two-dimensional approximation is used for this study because the width to height ratio is large. However, the effective dispersion of the system is underestimated due to the presence of channel side walls in actual experiments [67]. This effect is negligible for the case of a microchannel, but requires consideration when investigating nanochannels.

2.1.1 Governing Equations

The governing equation for the rate of change of the concentration of the ionic species is given by the Nernst-Planck equation,

$$\frac{\partial c_i}{\partial t} + \mathbf{u} \cdot \nabla c_i = D_i \nabla \cdot \left(\nabla c_i + \beta z_i e_0 c_i \nabla \Psi \right), \tag{2.1}$$

where c_i is the species concentration, $\mathbf{u}$ is the velocity vector, D_i is the diffusivity, β is the inverse of the Boltzmann constant times temperature, $1/(k_B T)$, z_i is the valence, e_0 is the elementary charge, and Ψ is the electric potential. This work considers an electrolyte that is monovalent and symmetric, and ions that are small enough to be considered point charges. The Nernst-Planck equation is coupled with the Poisson equation, relating charge density and electrostatic potential,

$$\epsilon \nabla^2 \psi = -\rho_E, \tag{2.2}$$

where ϵ is the total permittivity and ρ_E is the volumetric charge density, which has the form $\rho_E = e_0 \left(c_+ - c_- \right)$. The bulk fluid motion is determined by the Stokes equation,

$$\begin{aligned} 0 &= -\nabla p + \mu \nabla^2 \mathbf{u} + \rho_E \mathbf{E} \\ 0 &= \nabla \cdot \mathbf{u}, \end{aligned} \tag{2.3}$$

where ρ_w is the density of water, p is the pressure, μ is the viscosity, and $\mathbf{E}$ is the electric field due to an externally applied potential. Under steady conditions, the bulk fluid velocity is given by the Helmholtz-Smoluchowski, HS, equation, [44] [45]

$$u_{EOF} = -\frac{\epsilon E_0 \zeta}{\mu} \left(1 - \frac{\psi}{\zeta} \right), \tag{2.4}$$

where E_0 is the axial electric field applied through the channel. The electric field through the channel can be obtained using Ohm's Law and current density continuity,

$$\mathbf{J} = \sigma_{\text{EC}}\mathbf{E} \tag{2.5}$$

$$\nabla \cdot \mathbf{J} = 0, \tag{2.6}$$

where $\mathbf{J}$ is the current density in the channel, and σ_{EC} is the electrical conductivity of the solution. Here, the gradient in potential that arises due to free charge, $\nabla\psi$, is assumed to be decoupled from the externally applied electric field, $\mathbf{E} = -\nabla V$ [68]. The concentration can be recast in terms of charge density, $\bar{\rho}$, and conductivity, $\bar{\sigma}$:

$$\bar{\rho} = c_+ - c_- \; ; \quad \bar{\sigma} = c_+ + c_-, \tag{2.7}$$

to allow for faster numerical convergence and accuracy. The diffusivity is assumed to be

$$\overline{D} = 0.5\ (D_+ + D_-). \tag{2.8}$$

By adding and subtracting the cationic and anionic forms for Eq. 2.1 and using $\overline{D}$, the three coupled equations that determine the species evolution and potential then become

$$\epsilon\nabla^2\psi = -e_0\bar{\rho} \tag{2.9}$$

$$\frac{\partial\bar{\rho}}{\partial t} + \nabla\cdot\left(-\overline{D}\nabla\bar{\rho} - \overline{D}e_0\beta\bar{\sigma}\nabla\psi\right) + \mathbf{u}\cdot\nabla\bar{\rho} = 0$$

$$\frac{\partial\bar{\sigma}}{\partial t} + \nabla\cdot\left(-\overline{D}\nabla\bar{\sigma} - \overline{D}e_0\beta\bar{\rho}\nabla\psi\right) + \mathbf{u}\cdot\nabla\bar{\sigma} = 0\ .$$

Relevant dimensionless numbers based on these equations include the dimensionless Debye length, λ_D/h, and the Peclet number, $Pe = \frac{U_0 h}{D}$, where $\lambda_D = \sqrt{\frac{\epsilon k_B T}{2e_0^2 c_\infty}}$, h is the channel height, U_0 is the characteristic fluid velocity, D is the species diffusivity, and c_∞ is the reservoir

solute concentration. The velocity, U_0, refers to the characteristic velocity that representative of combined pressure-driven and electroosmotic flow in the channel.

2.1.2 Boundary Conditions

The rectangular, two-dimensional domain consists of an inlet and outlet and two charged, impermeable walls. The boundary conditions are as follows:

$$\mathbf{n} \cdot \left(\overline{D}\nabla\bar{\rho}\right)|_{\text{wall,outlet}} = \mathbf{n} \cdot \left(\overline{D}\nabla\bar{\sigma}\right)|_{\text{wall,outlet}} = 0, \tag{2.10}$$

$$\bar{\rho}|_{inlet} = 0\ ; \quad \bar{\sigma}|_{\text{inlet}} = 2c_\infty, \tag{2.11}$$

$$\mathbf{u}|_{\text{wall}} = 0, p|_{\text{inlet,outlet}} = \left(\mu\nabla^2\mathbf{u}\right)\mathbf{n}|_{\text{inlet,outlet}} = 0, \tag{2.12}$$

$$-\mathbf{n} \cdot \left(\epsilon\nabla\psi\right)|_{\text{wall}} = \sigma_w, \quad \psi|_{\text{inlet,outlet}} = 0 \tag{2.13}$$

$$\mathbf{n} \cdot \mathbf{J}|_{\text{wall}} = 0, \quad V|_{\text{inlet}} = V_0, \quad V|_{\text{outlet}} = 0, \tag{2.14}$$

where σ_w is the channel wall surface charge.

2.1.3 Current Through the Channel

The conductivity in the channel can be expressed in terms of the species concentration and velocity and has advective (σ_{adv}) and electromigrative (σ_{mig}) components,

$$\sigma_{\text{EC}} = \sigma_{\text{adv}} + \sigma_{\text{mig}}, \tag{2.15}$$

where σ_{EC} is the conductivity as defined in Equation 2.5, which, after recasting concentration and diffusivity as in Equations 2.7 and 2.8, can be written as

$$\sigma_{\text{adv}} = -\frac{1}{\nabla V} F \mathbf{u} \bar{\rho} \tag{2.16}$$

$$\sigma_{\text{mig}} = \beta e_0 F \overline{D} \bar{\sigma}, \tag{2.17}$$

where F is Faraday's constant. The current through the channel can then expressed as the current density times the area,

$$I = \langle -\sigma_{\text{EC}}(x,z) \nabla V(x,z) \rangle \, hw, \tag{2.18}$$

where h is the channel height (in the $z-direction$, w is the out-of-plane width of the channel, x denotes the axial variation, and the angle brackets, $\langle\rangle$, denote the area-averaged value of the contained variables. Note that $\bar{\rho}$ is generally much smaller than $\bar{\sigma}$, meaning the electromigrative component of conductivity generally dominates. The only case in which the advective conductivity contribution is substantial is when the EDLs overlap considerably (for very low concentrations or small channels).

2.1.4 Solution Methodology

The equations and associated boundary conditions are solved in a 2D finite element domain using COMSOL v4.4 (COMSOL, Inc., Stockholm, Se). Quadratic elements are used in solving for the electric potential and ionic potential, and linear elements are used for velocity and pressure fields. The mesh is refined adaptively in the Debye length near the charged wall such [69]. In the EDL, there were at least 20 elements per Debye length to ensure proper resolution of large potential and concentration gradients near the wall. Elements increase in size further from the wall to allow fewer elements to be used. Note that all equations were

solved dimensionally as in Equation 2.9. An electric potential of 200 V is applied through the channel, yielding a nominal electric field of 40 kV/m. KCl is used as the background electrolyte, with the diffusion coefficients of K^+ and Cl^- equal to $0.5 \cdot (1.96 \cdot 10^{-9} + 2.03 \cdot 10^{-9})$ m^2/s.

2.2 Materials and Methods

Materials All nanochannel devices were designed and custom fabricated in fused-silica wafers using conventional MEMS processing techniques. Briefly, straight designs were patterned with photolithography techniques, etched using wet chemical processes, and bonded to top wafers with drilled inlet and outlet ports via fusion bonding [46]. The final channel dimensions were 5 mm long, 5 μm wide, and 100 nm deep.

Chemicals and Reagents For all experiments, I diluted sodium tetraborate (Sigma Aldrich, Inc.) using de-ionized filtered water at 18 MΩ cm^{-1}, provided by a Millipore Milli-Q Gradient filtration system to 100 mM at pH 9.2. Next, stock solution was diluted to concentration of 1, 9, 10, and 50 mM. KCl was not used in experiments because it does not have buffering capacity to mitigate potential pH gradients due to wall deprotonation or electrochemical reactions at the electrodes. Since this is highly undesirable, I used a buffered solution for experiments. Borate buffer has been found, through other experiments [70], to match closely with KCl in terms of observed EOF velocity, if ionic strength is matched. Therefore, the time of arrival of the experiments will match that of the simulations when using a reasonable guess for the surface charge in the model. The current was matched using a multiplicative factor to convert sodium tetraborate to KCl using mobility values from literature [71] such that borate buffer and KCl have the same conductivity at the same ionic strength.

Current Monitoring We performed current monitoring (CM) experiments as described in detail elsewhere [42], in which, we filled one reservoir (the positive voltage reservoir) with a background electrolyte (BGE). Then, we applied 50 V via platinum electrodes placed within each fluid reservoir of the device using a high voltage sourcemeter (Model 2410, Keithley) to generate constant electroosmotic flow. After applying voltages, the system equilibrated within about 15 minutes, after which we removed liquid from the positive voltage reservoir and replaced it with BGE at the target concentration. We monitored the rise in current over time using an electrometer (Keithley 6517a, Keithley) controlled with Labview.

As the BGE of higher concentration enters the channel and migrates from the positive well towards the intersection, the current increases at a constant rate. The length of the channel divided by the duration of this initial transient is a direct measurement of area-averaged velocity.

2.3 Results and Discussion

2.3.1 Current Monitoring with finite EDLs and $\gamma \sim 1$

When $\gamma \sim 1$, there are negligible conductivity changes through the channel, so the axial electric field within the channel can be approximated as being constant. This also implies that there are no induced pressure gradients, so that the resulting CM curves are linear and one can simply use the Helmholtz-Smoluchowski equation, Equation 2.4, to solve for the mean zeta potential [61] [40] [42]. This is demonstrated in Figure 2.1, which shows a numerical simulations of normalized current versus normalized time of a 10 mM KCl solution displacing a 9 mM KCl solution in microfluidic channels of three different channel heights superimposed with this simple, linear equation. Note that for thin EDL systems, normalized current as a

function of time is simply

$$I/I_0 = \frac{1}{\gamma} + \frac{t}{t_{\text{HS}}}\left(1 - \frac{1}{\gamma}\right), \quad 0 < t < t_{\text{HS}} \tag{2.19}$$
$$I/I_0 = 1, \qquad\qquad t > t_{\text{HS}}$$

with

$$\begin{aligned} I_0 &= \sigma_\infty E_0\, h\, w \\ &= \left(\beta e_0 F \overline{D}(2c_\infty)\right) E_0\, h\, w, \end{aligned} \tag{2.20}$$

and

$$t_{\text{HS}} = \frac{L}{u_{\text{HS}}} = \frac{L\mu}{-\epsilon E_0 \langle\zeta\rangle}, \tag{2.21}$$

where t_{HS}, the normalized time, is the channel length, L over the HS velocity, σ_∞ is the bulk conductivity of the displacing solute, and $\langle\zeta\rangle$ is the height-wise averaged zeta potential for the displacing and displaced solutes. Note that there are extremely small differences between the numerical simulation and theory for the for 100 μm and 10 μm cases most likely because the numerical simulation solves the exact time dependent solution displacement problem accounting for the small differences in the electrolyte conductivity, which will induce very small pressure gradients.

Also note that the above theory does not match simulation or experiment for the case of finite electric double layers within the channels, which occurs in the case with 100 nm channels. Here, EDL thickness is approximately 10% of the channel height, and therefore, there will be a larger overall current due to the extra conductivity within the EDL [44]. Furthermore, the HS velocity is not constant; instead, it is non-uniform throughout the channel,

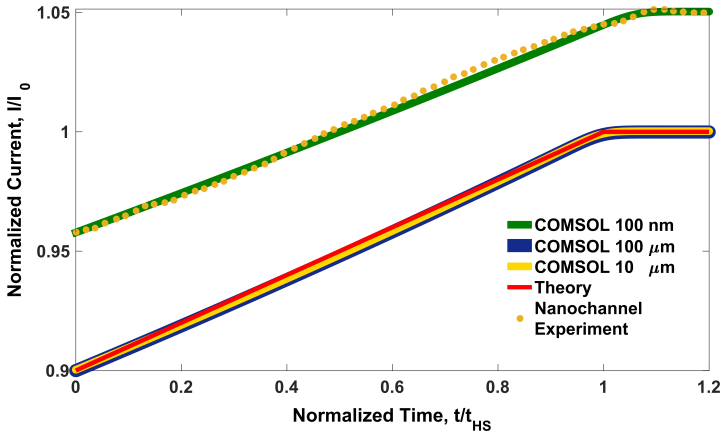

Figure 2.1: Current versus time for 100 nm, 10 μm, and 100 μm channels in which 10 mM KCl displaces the 9 mM KCl present in the channel with a surface charge of -10 mC/m^2. The nanochannel current is greater than microchannel current, but simulations match nanochannels experiments well.

resulting in a lower area averaged velocity and thus longer time-to-arrival [44]. However, since $\gamma \sim 1$, the current versus time curve is still linear, and the following normalization accounts for the effects of both the added current and longer time scale in a nanochannel (NC), enabling direct comparison between micro- and nanochannels:

$$\begin{aligned} I_{0,\mathrm{NC}} &= \sigma_\infty E_0\, h\, w + 2\langle\sigma\rangle_{\mathrm{EDL}}\rangle E_0\, (3\lambda_D) w \\ &\approx \left(2\beta e_0 F \overline{D} c_\infty\right) E_0\, w\cdot \qquad (2.22) \\ &\left(h + 3\left\langle (exp(-\beta e_0 \psi) + 1)\right\rangle \lambda_D\right), \qquad (2.23) \end{aligned}$$

and the HS time is

$$t_{\mathrm{HS,NC}} = \frac{L}{u_{\mathrm{HS}}} = \frac{L\mu}{-\epsilon E_0 \langle \zeta - \psi \rangle}, \qquad (2.24)$$

where $I_{0,\mathrm{NC}}$ and $t_{\mathrm{HS,NC}}$ account for the conductivity contribution in the EDL, as well as for the nonuniform transverse potential distribution and resulting slower area-averaged velocity profile. Although the time normalization ultimately yields the appropriate ζ-potential, $I_{0,\mathrm{NC}}$ may still not scale perfectly unless the extra conductivity in the definition of γ is considered.

In reality, numerical methods must be used to solve for ψ accurately, and therefore, the

above relations are difficult to use in practical scenarios. However, one can estimate the size of the EDL as $3\lambda_D$, where λ_D is simply a function of concentration [45]. In Figure 2.2a, the ratio of normalized current in a nanochannel to that in a microchannel as a function λ_D/h is plotted using a numerical solution to the following equation:

$$I_{0,NC}/I_0 = 1 + \frac{3\lambda_D}{h}\left(\langle exp(-\beta e_0 \psi)\rangle + 1\right). \tag{2.25}$$

For the sake of practicality, a fit to the above solution can be written as

$$I_{0,NC}/I_0 = 1 - \left(\frac{\lambda_D}{h}\right)^2 \left(1.567 \cdot 10^4 \sigma_w + 50\right), \tag{2.26}$$

with an R^2 value of 0.9997. This relation exhibits quadratic dependence with respect to λ_D/h as well as a fitting function with linear dependence on surface charge, for typical surface charge values of -5 to -50 mC/m^2. Note that at small ratios of λ_D/h this equation is simply 1. This new normalization can be used for all current monitoring curves when $\gamma \sim 1$; as long as the surface charge of channels is known. Although typical values for microchannels in literature are between -5 and -50 mC/m^2 [72], it is hard to know the exact value without repeated experimentation. Therefore, I show in Figure 2.2b the percentage error if I compare results with an arbitrarily chosen, typical value of -10 mC/m^2. For $\lambda_D/h < 0.015$, the change is negligible, and this assumption can work over all systems. However, as the EDL thickness increases, for example greater than 1.5 nm for a 100 nm channel, this assumption breaks apart due to the quadratic dependence of λ_D/h on current. The absolute value of current is not as important as the time to arrival to determine the ζ potential of a system. Therefore, it behooves us to not only look at the correct normalized time, but also the percent error if arbitrarily choosing a surface charge.

Figure 2.2c shows the normalized time versus λ_D/h. This normalized time can be written

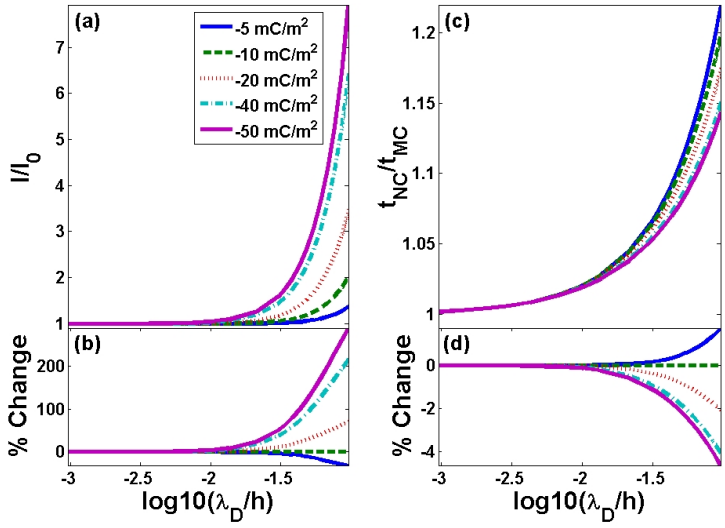

Figure 2.2: (a) Normalized current, (b) percent change in current compared with -10 mC/m^2, (c) normalize time, and (d) percent change in time compared with -10 mC/m^2 versus the ratio of Debye length to channel height. Current and time approach unity as $\lambda_D/h \to 0$. However, as λ_D/h increases, the EDLs are a larger part of the channel, and thus these values increase. We plot five different values of surface charge, and although the current value can change significantly, the percent change is minimal over all surface charges for time, which is the only important parameter in evaluating ζ-potential within the channel.

as

$$t_{\mathrm{HS,NC}}/t_{\mathrm{HS}} = \frac{\langle \zeta - \psi \rangle}{\zeta}. \tag{2.27}$$

The area-averaged potential difference, $\langle \zeta - \psi \rangle$ is calculated numerically. Similarly to normalized current, a fit for this function is written as:

$$t_{\mathrm{HS,NC}}/t_{\mathrm{HS}} = 1 + \left(\frac{\lambda_D}{h}\right)\left(292.2\sigma_w^2 + 30.49\sigma_w + 2.352\right), \tag{2.28}$$

giving linear dependence on normalized time as a function of λ_D/h and a fitted quadratic dependence as a function of surface charge with $R^2 = 0.9973$.

We note that as the EDL grows, the displacing solute arrival time increases because thicker

EDLs correspond to a more nonuniform velocity profile and thus lower area-average velocity. However, similarly to current, as shown in Figure 2.2d, the percent change in arrival time for a surface charge different than -10 mC/m^2 shows a difference of $< 5\%$ even at large λ_D/h. Therefore, even though the current may be much higher than expected, the time to arrival can still be used with the new scaling and fit to determine the zeta potential of the channel. This time to arrival is key since one can solve for ζ-potential using the CM method.

To prove that these relations are in fact valid, I performed CM experiments in nanochannels as described in Section 2.2. Superimposed on the nanochannel simulation curve in Figure 2.1 are experimental data from 100 nm custom fabricated nanochannels. Not only do experimental data and simulations match well, but this relation can be used to solve directly for ζ-potential, without using the simulation data and instead using the function above. To do so, I simply take the actual time-to-arrival (note that in Figure 2.1 I divided by the HS velocity) and divide by the relation in Equation 2.28, to get the HS time as if in a microchannel. Then, I use the relation $\zeta = -\frac{L\mu}{\epsilon E_0 t_{\text{HS,NC}}}$ to obtain the ζ-potential. In this case, doing so, and assuming a surface charge of -10 mC/m^2, I get a ζ potential of -41.8 mV. Note that this is what I usually measure in custom fabricated microchannels of the same salt concentrations [62], although the zeta potential will vary with surface charge and λ_D/h as shown in Figure 2.3.

2.3.2 Monitoring with High γ

When $\gamma \gg 1$, non-uniform electric fields due to the conductivity differences give rise to internal pressure gradients [65]. These internal pressure gradients arise to satisfy continuity and increase dispersion in the channel, highly affecting the shape of the resulting solution displacement curves. One representative set of curves for $\gamma = 50$ is shown in in Figure 2.4. Note that the shape of the curve is dependent on the height of the channel, not just the concentration ratio.

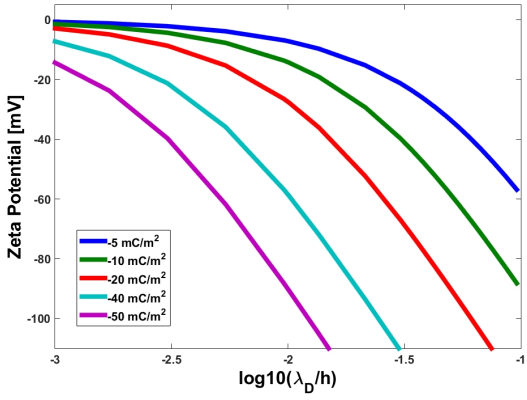

Figure 2.3: Expected zeta-potential vs λ_D/h for different surface charge values. For thicker EDLs, the expected zeta potential will vary significantly depending on the predicted surface charge; however, this is still captured in the model.

Dispersion occurs under the combined effect of molecular diffusion and the nonuniform velocity profile that can exist within a system [73]. Dispersion coefficients have been accurately solved for over a wide range of profiles analytically using the Aris method of moments equations, as well as numerically [74], [75]. Although some have looked at dispersion due only to EOF, pressure-driven flow is the primary component contributing to Taylor dispersion for high γ, and is fairly well characterized [76] [77] [78] [79] [80]. Furthermore, in microfluidics, many have looked specifically at Taylor-Aris dispersion in systems with non-uniform pressure gradients with and without finite double layers [47] [81] [48]. Some have also studied dispersion in the pure convection regime within microchannels [82]. Dispersion was deduced from a result of the numerical simulation, which simultaneously solved Poisson-Nernst-Planck and Stokes equations. Since these underlying equations have no closed-form solution in the case of a nanochannel, an equation for dispersion (as in the method of moments by Taylor) cannot be easily derived.

All studies mentioned have focused only on one particular regime of dispersion (Taylor, Taylor-Aris or pure convection). However, typical operation of CM in microfluidic channels can allow for several different regimes of dispersion within the same experiment, based on

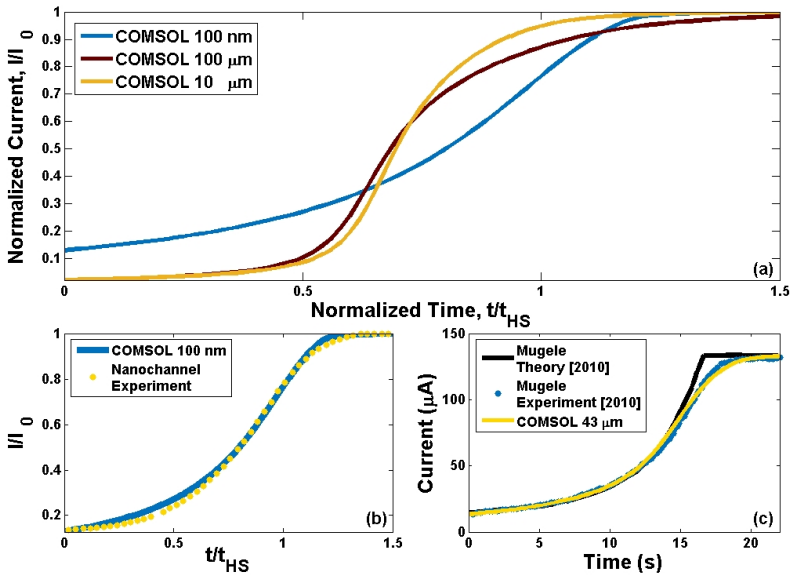

Figure 2.4: Experiment, COMSOL simulation, and theoretical current monitoring for high γ ratio configurations. A comparison of COMSOL simulations performed using different channel heights for which 50 mM KCl displaces 1 mM with a surface charge of -10 mC/m^2 is shown in (a). These are normalized by I_0 and t_{HS}. The 100 nm channel has higher relative current because of the finite EDLs and also takes longer to reach a steady state current. Next, in (b), I compare experiments conducted in a 100 nm channel under the same conditions as in (a) and the 100 nm COMSOL simulation. These curves show excellent agreement. Finally, existing literature theory and experiments are directly compared with COMSOL simulation. As expected, the simulation captures all the dispersion effects and matches the experiment more accurately than the previous theory.

the extent of the non-uniform gradients. Figure 2.5 shows regimes investigated both theoretically and experimentally, typical of experimental microfluidic systems, superimposed with the classic Probstein dispersion map [2]. The circles in the figure represent the highest possible Pe number for a given channel height, where Pe is defined using Hagen-Poiseuille flow in between parallel plates,

$$u_{\text{PDF}} = \frac{1}{2\mu}\left(-\frac{dp}{dx}y(h-y)\right), \tag{2.29}$$

except for the case of the nanochannel, where I add dispersion due to the nonuniform electroosmotic flow profile [78]. The internal pressure gradients that develop at high γ are the

driving mechanism behind the nonuniform velocity profile, and the dotted lines correspond to decreasing γ, down to one, when the induced pressure becomes negligible, and the associated pressure-driven flow component of velocity is zero, as seen in Section 2.3.1. As the interface moves through the channel, the pressure gradients and therefore Pe vary spatiotemporally, thereby causing the solute to experience difference dispersion regimes depending on the time and channel position.

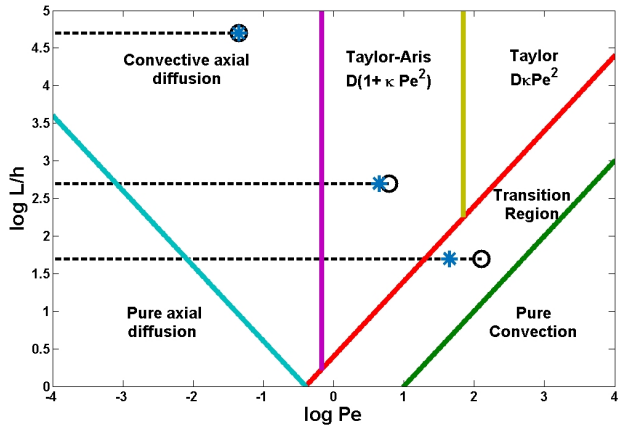

Figure 2.5: This figure, adapted from Probstein [2], shows the different regions in which the role of diffusion, dispersion, and convection vary in importance. The black circles show the Peclet number under the case of maximum total flow, maximum pressure-driven flow combined with underlying EOF, found in the channels obtained when simulating the largest γ. The blue stars show the case of uniform EOF when $\gamma \sim 1$. The dotted lines demonstrate that, for purely uniform EOF, there will be no dispersion, leading to neglible Pe.

Figure 2.4a shows CM curves for three different channel heights, spanning the range of dispersion regimes. To validate the simulation, I performed CM in a nanochannel (Figure 2.4b), as well as replotted data from [63] in a microchannel (Figure 2.4c). The nanochannel experiment matches the simulation well, and the simulation matches the microchannel experiment well. In fact, the simulation is a much closer match than the previous theory used because dispersion was neglected. Note that even though the two different experiments are in widely varied dispersion regimes, the simulation can capture the data well.

To explain why the CM curves look the way they do, Figure 2.6 shows representative con-

tour plots all at the same normalized time (the actual simulation time divided by the average HS time for both concentrations) of 0.54 for the 100 nm channel (a), 10 μm channel (b), and 100 μm channel (c). The 100 nm channel is in the convective diffusion regime, 10 μm is in the Taylor-Aris regime, and 100 μm is between Taylor-Aris and pure convection (Figure 2.5. Also, in the 100 nm channel, the largest observable transverse concentration gradient occurs in the double layers, which is why in this case EOF contributes to convective dispersion. As the concentration ratio increases, the double layers become thinner, but because the channel height is so small, transverse diffusion will dominate over advection, and diffusion generally dominates over any sort of dispersion. In the 10 μm case, transverse diffusion is still much faster than advection, however, there is more dispersion due to PDF at high concentration ratios than in the nanochannel case because the channel height is larger. This dispersion is in the Taylor-dispersion regime, and therefore is well-mixed in the transverse direction of the channel, and has the smallest transverse concentration gradients.

Figure 2.6 shows that the 100 μm channel has the most convective dispersion, meaning that there exist large transverse concentration gradients due to the PDF within the channel. In this scenario, since the Pe is in general larger, there is not enough time for transverse diffusion to occur, allowing the parabolic PDF profile to remain visible in Figure 2.6. This in itself explains the CM profile in Figure 2.4a. The curve shows that at small time, the current is actually larger than the 10 μm case, presumably due to the forward pressure gradient causing higher concentrations to come forward. However, midway through the channel, this behavior changes because axial dispersion is so great that the time to actually reach the nominal current is greater.

I can further explain the CM plots through Figure 2.7, which plots normalized time of arrival versus γ for the higher concentration ratios of $\gamma = 10, 20$ and 50. Here, I normalize the time by t_{HS}, where t_{HS} takes into account the average ζ-potential for each concentration ratio. This figure shows the important components of Figures 2.4 and 2.6 across the range

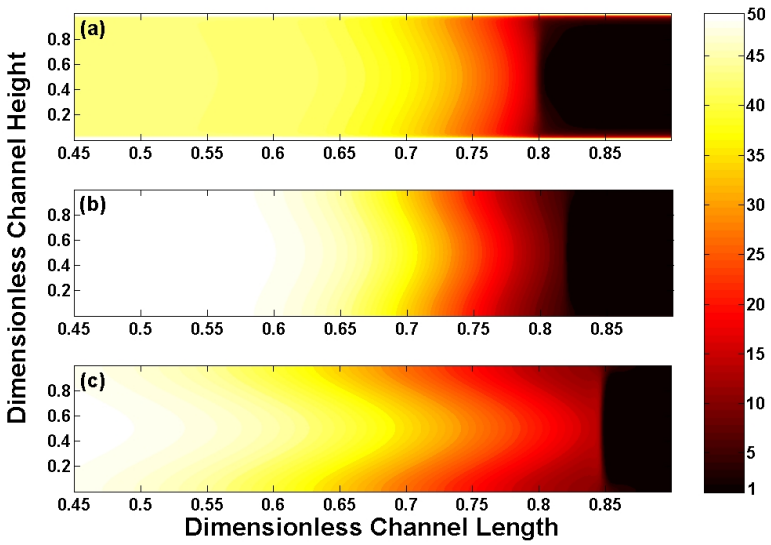

Figure 2.6: This figure presents a color map of KCl ionic strength in the channel for the normalized time step of 0.54 for the 100 nm channel (a), 10 μm channel (b), and 100 μm channel (c), where 50 mM KCl displaces 1 mM. Ionic strength is used to represent the front even though the front is composed of both cations and anions. Because electroneutrality is maintained in the bulk of the channel, both species exist in the same configuration; however, in the EDL there are excess cations and a depletion of anions. The most dispersion occurs in (c), where PDF is greatest.

of concentration ratios. The 100 μm channel has the largest time to arrival, which can be attributed to the highly convective behavior dominating transverse mixing. Both the 10 μm channel and 100 nm channel time to arrival is shorter than for the 100 μm channel. For these two cases, the time to arrival actually decreases with concentration ratio because Taylor dispersion allows the channel to be well-mixed in the transverse dimension, meaning that axial dispersion can allow for the plug to reach 99% before it would had there not been dispersion. The time to arrival is still always greater for the nanochannel case relative to the 10 μm channel because of the retardation of flow due to EOF in the low concentration regime. As γ increases, the time to arrival for the nanochannel approaches that of the microchannel because the effect of EDL thickness decreases (higher concentrations mean smaller double layers).

Lastly, an important consideration is knowing when the theory fails. I assumed small, monovalent electrolytes, and a continuum relation between surface charge and zeta potential. This will break down when using high wall surface charges (over 200 mV), large polyvalent ions that may cause charge inversion, and systems that may exhibit concentration polarization. However, for the bulk of microfluidic system where small ion buffers in concentrations between $1 - 100$ mM are being used, my results are accurate for CM curves with both finite EDLs and high concentration ratios. The effective dispersion may be also be underestimated because of the presence of channel side walls in actual, physical systems [67]. For the microchannel case with thin double layers, the side walls do not affect the dispersion in the time regime investigated. However, for the 100 nm channel, the finite double layers and width to height ratio produce an expected dispersion coefficient at most six times larger than for parallel plates. Therefore, three-dimensional simulations would be required to fully capture the side-wall dispersion, but a two-dimensional approximation remains within an order of magnitude.

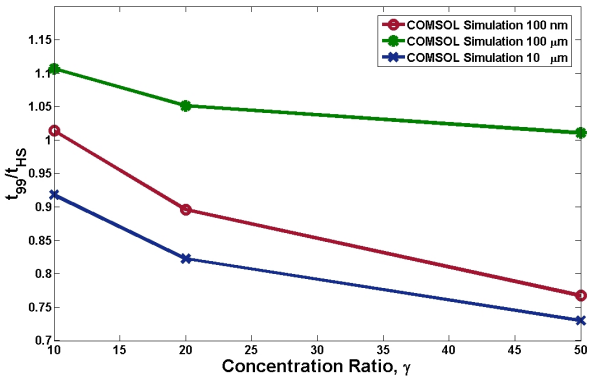

Figure 2.7: This shows the normalized time at which the current reaches 99.9% of the final value for high concentration ratios. The induced dispersion severely skews the arrival time, especially for the Taylor dispersion-dominated 10 μm channel.

2.3.3 Conclusion

The solution displacement technique is a quick and easy experimental method to solve for the ζ-potential in a micro- or nanofluidic channel. However, finite double layers and large concentration gradients can lead to inaccuracies of measurement. In this chapter, I explore these discrepancies both theoretically and experimentally, and accurately show different dispersion regimes of practical microfluidic systems due to spatial conductivity gradients. These dispersion regimes lead to different shapes of current monitoring curves. In addition to explaining the different regimes of CM, I also present guidelines with which to predict accurate zeta potential even with finite double layers.

Reprinted from Ref. [66] with permission from Springer.

Chapter 3

Using Theory to Enhance Experimental Understanding

3.1 Introduction

Deep theoretical understanding of experimental micro- and nanofluidic systems has guided the design and optimization of breakthrough innovations in our field. For example, Torrie and Valleau [83] observed charge inversion in the electric double layer (EDL) using Monte Carlo simulations in the 1980's, which has furthered the experimental understanding of the electric double layer [58] [84]. More recently, experimentalists [85] have taken advantage of similar Monte Carlo simulations to better understand ion-selective nanochannels. This optimization of experimental systems through theoretical analysis contributes significantly to the field, but it is the ability to further use that theory for the predictive design of systems that can truly motivate scientific endeavors. For example, recent Molecular Dynamics simulations shed light on confined heterogeneous surface charge systems [86], showing potential for active electroosmotic flow control. This novel, active control can be predictively tailored for real-time fine manipulation of single charged species for biological diagnostic applications [87].

Such predictive modeling can spark genuinely innovative breakthroughs and fill in as-yet misunderstood nano-scale electrochemical processes.

This section describes my role in utilizing theory to better understand initial experimental results. Over the last five years, I have collaborated with experimentalists in the lab to further their innovations and understanding of their systems through my background in modeling of electrokinetic micro- and nanofluidics. The first project exploited the high surface area to volume ratio of nanofluidics to prove the validity of all-electronic DNA sensing based on DNA-induced nanochannel conductivity due to changes in apparent surface charge [88]. Dr. Pete Crisalli synthesized all compounds and performed all experiments. I produced a model to predict the change in nanochannel conductivity with changes in surface charge due to DNA adsorbed to the modified surface. Second, DNA hybridization and reaction thermodynamics were investigated experimentally in microchannels under varying electrolyte and DNA species conditions by Dr. Tom Wynne [4], as well as under the effect of nanoconfinement by rotation student Yanxian Lin and graduate students Joe de Rutte and Alex Downs [89]. Again, I modeled the system using the convective-diffusion-reaction equation and extract parameters by matching simulation results with experimental data. Lastly, Josh Loessberg-Zahl, an undergraduate student, observed a standing isotachophoretic-like front between $Ru(bpy)_3Cl_2$ (which causes flow reversal) and $MgCl_2$ in 100 nm silica nanochannels, which we were able to successfully model [90]. This exciting project showed that it is possible to produce a non-dispersive standing front by tuning the ion mobilities and surface charges appropriately. Here, I performed nanochannel current monitoring experiments to obtain zeta potential values for different electrolytes as well as aided in the modeling and elucidation of observed phenomena. Overall, I have had the privilege to work with fantastic scientists toward a mutual goal of understanding nanofluidic electrokinetics. The remainder of this chapter describes these bodies of work, DNA detection in nanochannels, DNA hybridization under non-equilibrium conditions in micro- and nanochannels, and the effect of complex ionic species on fluid flow

in nanochannels.

3.2 Label free detection of nucleic acids by modulating nanochannel surfaces

In this work, we developed surface-modified 100 nm silica nanofluidic channels whose solution conductivity changes upon exposure to single- or double-stranded DNA. Through careful monitoring of both electromigrative and advective current in the channel, we can detect nanomolar concentrations of DNA. These results can be exploited for inexpensive, all-electronic DNA sensors. [88]

Facile detection of nucleic acids is important for rapid screening for pathogen detection [91]. While various methods exist, most require the addition of a labeling reagent for detection, often via a spectroscopy [92] [93]. Such methods, however, are not ideally optimized for point of care detection, as use of laboratory instrumentation is required for a sample assay. Alternative methods for specific sequence detection become even more laborious, as introduction of radiolabels or the need for gel electrophoresis increases the time, skill, and materials needed for detection [94]. Electric methods represent unique alternatives for simple detection of biological components [95], particularly with the expansion of nanopore technology for complete label-free nucleic acid sequencing [96]. Ideally, simple devices should be capable of utilizing DNA interactions with surfaces to initiate changes in electronic properties measured through change in current, potentially eliminating the need for laboratory instrumentation and improving point-of-care detection [97]. However, these approaches often require addition of a reporter tag to at least one nucleic acid or the need for highly specific surfaces and transition-metal containing buffers for optimal changes in current upon sample exposure [98].

Nanofluidic devices offer an alternative means of analyte detection based upon the unique properties inherent to nanochannels. In general, because of the large surface area to volume ratio, the surfaces of nanofluidic channels or pores can be exploited for all-electronic biomolecular sensing [97]. There are a couple of mechanisms that allow for such sensing, the first being the fact that large biomolecules can actually clog the channel or pore, changing the resulting measured current, as is the case for nanopore sequencing [96]. Alternatively, the addition of biomolecules to the surface in a nanoconfined system can change the potential on the wall or surface, thus the resulting ionic conductance of a buffer interacting with it [97] [99].

While nanopore and nanomembrane detection approaches show great promise, they also display difficulties in precise, repeatable, and inexpensive preparation. Planar nanofluidic channels, however, have already shown excellent repeatability via commonly used glass fabrication methodology and properties of the nanofluidic wall have been well examined [72] [100] [53]. Moreover, nanofluidic devices present great advantages in portability and decrease in sample consumption as channel volumes are in the low picoliter range.

3.2.1 Experimental Setup

Combining these properties, we aimed to develop a simple glass-fabricated planar nanofluidic assay to detect nucleic acids without added reagents, only monitoring changes in measured current through a modified nanochannel upon sample DNA exposure (Figure 3.1). To do so, we use our recently developed model to solve for electromigration and advective current within the nanochannel with varying surface charge [72]. As shown in Figure 3.2, for a 16 mS/cm buffer (the measured value for phosphate buffered saline employed in experiments), surface potential affects measured conductivity drastically for smaller channels because of the relative contributions of advective and electromigration current [44] [45]. Note that for

larger channels with thin electric double layers (EDLs), the value of zeta potential does not affect the measured conductivity within the channel, making it impossible to measure difference in such channels. We exploit this feature of nanofluidic channels to detect biomolecular surface attachment.

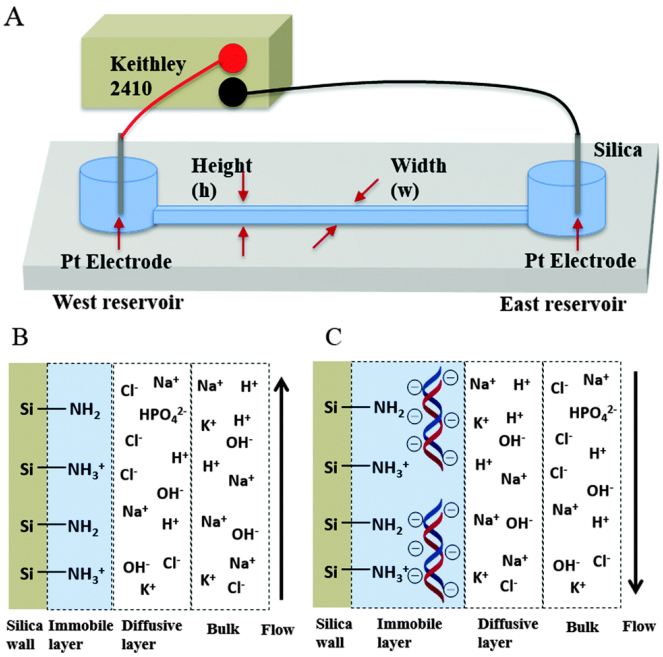

Figure 3.1: (A) Experimental setup for 100 nm height fused silica nanofluidic channel connected to a sourcemeter (Keithley 2410). (B) Interactions of aminosilanized nanofluidic wall with buffer components. (C) Interactions of aminosilane/dsDNA adsorbed nanofluidic wall with buffer components.

We therefore designed a simple nucleic acid sensor by measuring specific changes in the surface potential upon interactions with nucleic acids, using 25 base ssDNA and dsDNA oligomers as examples. We measured phosphate buffered saline in either 100 nm or 89 nm nanofluidic channels with a sourcemeter (Keithley, 2410) at a constant voltage (+600 V) before and after sample exposure, and detected the presence of surface attached nucleic acids through changes in the current. Moreover, surface potential at the wall determines direction of flow [72], allowing detection through simply observing direction of flow (i.e. positive current) before and after sample incubation. The initial design selectively formed dsDNA at the wall of a 100 nm height nanochannel by performing surface modification to incorporate ssDNA and allowing for subsequent hybridization of the complimentary sequence. The formation of dsDNA at the wall decreases the zeta potential of the channel wall, providing readily

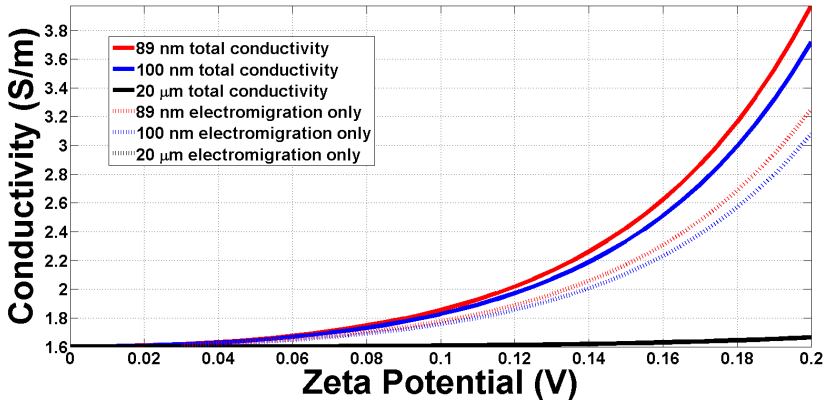

Figure 3.2: Channel conductivity as a function of zeta potential for 89 nm, 100 nm, and 20 μm channels. In all cases, as the zeta potential increases, the conductivity increases. For the microchannel, the EDL contribution to conductivity remains minimal, while for the nanochannels, the EDL contribution increases substantially. Note that the conductivities are higher in a shallower channel because a higher percentage of the channel is taken up by the EDL. Using this model, we can estimate the change in surface potential due to surface modification.

observed changes in measured current as long as the channel is small enough (Figure 3.2).

Amine modification was performed by filling a dry channel with a 4% (v/v) solution of 3-(aminopropyl)trimethoxysilane in 18 MΩ MilliQ water followed by overnight incubation and washing with water. Successful modification was confirmed by an increase in the measured current from a typical average of 92 ± 3 nA (-75 mV surface potential) for unmodified nanochannels to 101 ± 2 nA ($+100$ mV) for the amino modified nanochannels [72]. As noted by the surface potentials calculated, amino modification induced charge inversion of the surface to a positive charge (at pH 7.4 used), changing the direction of flow, consistent with previous work.[99] The amino modified surface allowed for channel wall attachment of 5'-amino modified DNA 25mer (5'-NH2-TTTTTTTTAGCACGTATAGTTTT-3') via bis(sulfosuccinimidyl)suberate, (BS3) crosslinking, confirmed by a decrease in the measured current to 85 ± 4 nA ($+60$ mV) as the negatively charged DNA partially screens positively charged amino groups. Subsequent incubation with 5 μM of complimentary DNA 25mer (5'-AAAACTATACGTGCTAAAAAAAA-3') for three hours in hybridization buffer (70 mM

Tris borate, 10 mM $MgCl_2$, pH 7.55) followed by washing increased the measured current of PBS an average of 64% (to 139 ± 12 nA), while unmodified channels displayed no significant change in current upon incubation with ssDNA or dsDNA. The large increase in current for ssDNA modified surfaces was accompanied with a change in surface potential from positive to negative (Figure 3.3). Modification of the nanochannel wall with a DNA sequence noncomplimentary to incubated ssDNA increased the current by 40% as well as created a negatively charged surface, indicating some background interactions derived from the BS3 surface. We confirmed DNA hybridization in channels by using a 5'-fluorescein labeled complimentary strand.

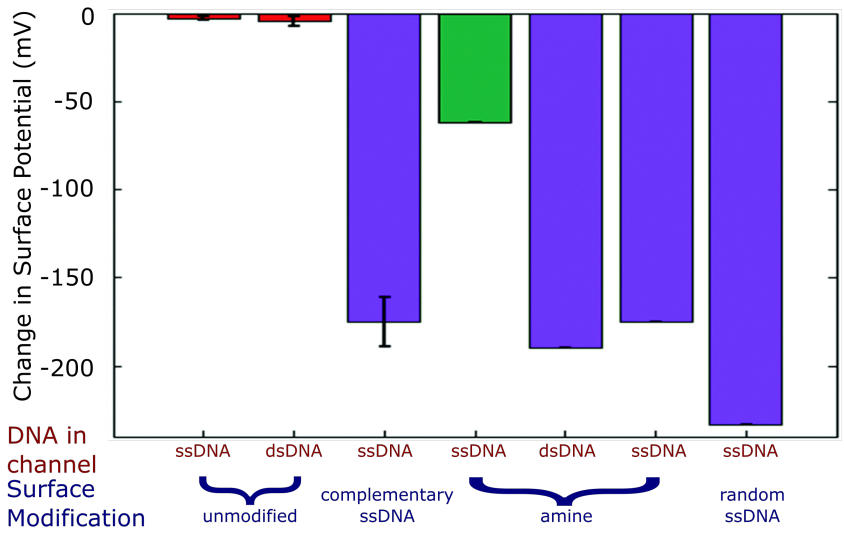

Figure 3.3: Change in calculated surface potential of 100 nm tall nanochannels after incubation with 5 μM ssDNA or dsDNA. Red bars indicate negative surface potential throughout, green bars indicate positive surface potential throughout, and purple bars indicate change in surface potential from positive to negative after DNA exposure.

Importantly, similar experiments in an ssDNA modified 20 μm microchannel displayed negligible change in current (-0.4%), indicating importance of the nanochannel to induce large alterations in current properties. As seen in Figure 3.2, the larger microchannel dimensions make calculations of surface potentials more difficult as bulk flow is the leading

determinant of current.

We next examined the interaction of ssDNA with an amino modified surface only, as we anticipated nonspecific interaction of the negatively charged phosphate backbone with a positively charged surface [99] [101]. Incubation of ssDNA with an amino modified channel displayed a decrease in measured current (101 nA prior to incubation, 89 nA after, -12%) due to nonspecific adsorption of the ssDNA to the channel wall, but not sufficiently enough to negatively charge the surface (surface potential decreased from $+100$ mV to $+38$ mV, see Figure 3.3). Washing the channel with Tris-EDTA buffer (TE buffer, pH 7) removed some adsorbed ssDNA from the channel wall, as the current increased to 97 nA (surface potential of $+88$ mV). Re-incubation of 5 μM ssDNA in the same channel now provided the same current and surface potential, indicating that the surface had become saturated with ssDNA. Upon incubation of a solution of annealed dsDNA, however, the channel displayed not only a moderate increase in measured current of PBS but also re-inversion to a negatively charged surface ($+71$ mV to -119 mV), indicative of considerable adsorption of dsDNA to the amine surface.

We performed considerable experiments using just aminosilane/BS3 modified channels (without adding ssDNA to the channel wall) and found considerable binding of both ssDNA and dsDNA at low concentrations. However understanding and modelling this surface is inherently difficult when considering the variety of possible reactions between BS3 and a simple amine surface. Thus, further experiments with simple amino modified surfaces were performed to better model and understand its capability as a general sensor platform for single- or double stranded DNA. Previous studies of ssDNA interaction with amino modified 30 nm nanochannels had shown changed wall properties at high concentration of ssDNA incubation and our initial results indicated differences between ssDNA and dsDNA interactions at the channel surface. For these experiments, 89 nm height nanochannels were prepared using standard fabrication procedures and amino-silanization, then exposed to increasing con-

centrations of ssDNA or dsDNA. When measuring the current and calculating the resulting surface potential, differences between ssDNA and dsDNA behaviour were notable at 500 nM and 5 µM samples (Figure 3.4). Low concentrations (5 nM and 50 nM) of ssDNA or dsDNA changed measured current only slightly, keeping a similar or slightly lower positive surface potential. Incubation of 500 nM ssDNA created detectable changes in measured current (11% increase), and, more interestingly, generated channels with bidirectional flow (Figure 3.4). These channels were subsequently exposed to 5 µM ssDNA but surface saturation was evident from 500 nM exposure. 500 nM was also the threshold for altering surface properties with dsDNA, with surface changing from $+88$ mV to -113 mV, but this is a significantly higher than the threshold for BS3 (where changes in channel properties were observed at 5 nM dsDNA incubation).

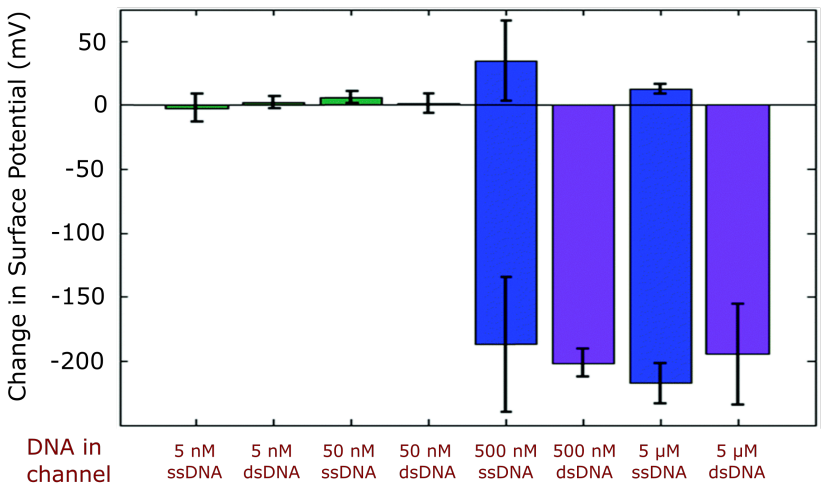

Figure 3.4: Change in calculated surface potential of various amine modified nanochannel surfaces after incubation with variable concentration of ssDNA or dsDNA. Green bars indicate positive surface throughout, purple bars indicate change in surface potential from positive to negative, and blue bars indicate bidirectional flow (positive and negative surface potential) after DNA exposure.

To further confirm that interactions of the amino modified surfaces were specifically because of ssDNA or dsDNA, we degraded a dsDNA sample with DNase and then incubated the resulting reaction mixture in unmodified or amino modified channels. These experiments

showed negligible change in measured current for both an unmodified channel (-0.55%) and an amino modified channel (1.2%). Importantly, inverted charge and direction of flow was maintained in the amino modified channel, indicating little to no non-specific adsorption of nucleotides. Consequently, re-inversion in charge and changes in measured current of amino modified nanochannels are specifically the result of oligomers of ssDNA and dsDNA as opposed to interaction with nucleotides or small ions in general, providing promising early results for nanofluidic channels as label-free nucleic acid sensors. Performing the same experiment with a BS3 modified nanochannel displayed unstable current values, indicating this surface may be sensitive to nucleoside mono-phosphates with a different wall interaction than oligonucleotides.

3.2.2 Discussion

In total, there are 5 regimes possible for interactions of nucleic acids at the channel wall that will subsequently change the nanochannel wall surface potential. First is simply no interaction with the channel wall, as observed with unmodified channels (via charge repulsion) or dilute concentrations of ssDNA or dsDNA, where minimal change in current was observed and surface potential maintained. Next, minimal interactions between the nucleic acid and the surface can occur, most likely where the nucleic acid is not bound tightly, observed by a decrease in the measured current whilst maintaining direction of flow (for example, in cases of ssDNA in 100 nm amino modified channels). Alternatively, a greater degree of interaction with adsorbed DNA provides change in the direction of flow but results in reduced measured current. When sufficient DNA is present with the appropriate wall, high binding will occur, increasing the current and inverting charge, as seen in ssDNA modified channels interacting with the complimentary sequence to form dsDNA at the wall or high concentrations of dsDNA non-specifically adsorbing to amino modified nanochannels. Finally, bidirectional flow

can be attained, although understanding this surface (as seen in ssDNA with aminosilanized channels) is difficult and may be the result of zwitterionic or net neutrally charged surfaces.

While our initial experiments confirmed the ability of the system to serve as a non-specific sensor for nucleic acids via negatively charged phosphate backbone interactions with a positively charged (aminosilanized) nanochannel surface, we still sought to have specificity. To this end, we adopted a different surface functionalization, namely azidosilanization. Coupling this surface to copper-free click chemistry for better DNA attachment, we theorized that improved specificity could be attained. Indeed, successful azidosilane modification afforded reduced surface potential as confirmed by the low measured currents. Subsequent reaction with 5'-DBCO modified DNA increased the negative surface potential (as DNA was selectively attached to the surface by this reaction) using a known sequence for PCR based detection of Ebola (5'-DBCO-CAAGAAATTAGTCCTCATCAATC-3') [102]. Exposure of the resulting ssDNA surface modified nanochannels to 5 μM of a complimentary DNA sequence (5'-FAM-GATTGATGAGGACTAATTTCTTA-3') increased the measured current modestly ($3.5 \pm 0.8\%$) while the calculated surface potential decreased by 11 ± 3 mV, indicating a further negative potential at the surface based upon dsDNA formation. Importantly, negative controls resulted in reduced changes in both the measured current and calculated surface potential. When ssDNA modified surfaces were incubated with a mismatch sequence (5'-FAM-AAAACTATACGTGCTAAAAAAAA-3'), the current increased by $1.6 \pm 0.5\%$ as indicated by a change in the calculated surface potential of only -6 ± 2 mV. This indicates that although there is likely some nonspecific adsorption of the mismatch to the negatively charged channel surface, it is considerably less than when using an aminosilane modified surface and indicates considerably greater repulsion of nucleic acids by the azidosilanized surface. This was experimentally confirmed by incubating the complimentary DNA oligonucleotide inside a nanochannel modified to contain only an azidosilane surface (no ssDNA surface modification). Similar to incubation with a mismatch sequence, the measured current changed by only

$2 \pm 1\%$ indicating a change in the surface potential of -5 mV. These results cumulatively indicate the ability for azidosilanization of a nanochannel wall and subsequent strain promoted click chemistry to allow for a moderately negatively charged surface that can become more negatively charged upon recognition of a complimentary sequence, reducing our concerns for an aminosilanization approach.

3.2.3 Conclusions

Our experiments confirm the capability of nanofluidic channels to be used for detection of nucleic acids. While microchannels show virtually no change in properties upon nucleic acid interactions at the channel wall, considerable changes in properties can be attained in 100 nm or smaller nanochannels based upon the modifications made to the nanochannel wall. Importantly, ssDNA and dsDNA generate different properties upon adsorbing to aminosilanized channels, while employing azidosilanization and click chemistry can greatly reduce nonspecific adsorption while still providing measurable changes for a perfect compliment. These results provide the basis for future nanochannel wall modifications to optimize changes in surface properties upon binding of nucleic acids, and future efforts will be made to allow for single nucleotide resolution of binding biologically important sequences to DNA wall modified nanochannels and simple label free detection using an all-electronic approach. Future designs incorporating neutral (or near-neutral) surface modifications and uncharged nucleic acid derivatives (e.g., PNA, morpholino DNA) are likely to provide increased sensitivity to change in surface potential while reducing nonspecific adsorption based upon charge pairing [97] [98] [103].

Reproduced from Ref. [88] with permission from The Royal Society of Chemistry.

3.3 Hybridization Thermodynamics of DNA Oligonucleotides during Microchip Capillary Electrophoresis

As described in Section 1.2, Capillary electrophoresis (CE) is a powerful analytical tool for performing separations and characterizing properties of charged species. For reacting species during a CE separation, local concentrations change leading to non-equilibrium conditions. Interpreting experimental data with such non-equilibrium reactive species is non-trivial due to the large number of variables involved in the system. In this section we develop a COMSOL multiphysics-based numerical model to simulate the electrokinetic mass transport of short interacting ssDNAs in microchip capillary electrophoresis. We probe the importance of the dissociation constant, K_D, and the concentration of DNA, on the resulting observed mobility of the dsDNA peak, μ_w by using a full sweep of parametric simulations. We find that the observed mobility is strongly dependent on DNA concentration and K_D, as well as ssDNA concentration, and develop a relation with which to understand this dependence. Furthermore, we present experimental microchip capillary electrophoresis measurements of interacting 10 base ssDNA and its complement with changes in buffer ionic strength, DNA concentration and DNA sequence to vary the system equilibria. We then compare our results to thermodynamically calculated K_D values.

3.3.1 Introduction

Capillary electrophoresis (CE) has been a workhorse tool to analyze the size, charge, and mobility of chemical and biological species. CE has also been used to determine kinetic and thermodynamic parameters, recently coined kinetic capillary electrophoresis (KCE), and defined as a CE separation of interacting species.[104],[105] Drug-protein binding, for example, has been studied experimentally and computationally using five equilibrium methods of KCE;

affinity capillary electrophoresis (ACE), Hummer-Dreyer (HD), frontal analysis (FA), vacancy peak (VP), and vacancy affinity capillary electrophoresis (VACE) [106] [107] [108] [109]. Although these methods give useful information about the equilibrium parameter K_D, dynamic parameters such as the rate constants (k_{off} and k_{on}) cannot be determined.

Non-equilibrium methods for KCE were introduced in 2002, most notably non-equilibrium capillary electrophoresis of equilibrium mixtures (NECEEM).[104] Here, a plug of two reacting species in equilibrium enters the capillary, and electrophoretic forces drive the protein and target in different directions away from the complex, thereby enabling the study of non-equilibrium dynamics of the kinetic system. Okhonin et al. developed analytical solutions for the determination of rate constants based on the ratio of electropherogram peak areas in NECEEM,[105],[110] however these analytical solutions assumed forward reactions are negligible and are therefore neglected. Krylova et al. derived two parameters, slow-dissociation parameter (SDP) and slow-recombination parameters (SRP), to test if assumptions used in NECEEM analysis are valid.[111] Okhinin et al. developed numerical simulations and performed experiments to determine rate constants k_{off} and k_{on} of protein-DNA interactions using plug-plug KCE where reactive analytes are injected sequentially separated by a small amount of run buffer so that the analytes electrophoretically move in opposite directions and migrate through each other.[112] To date, only KCE systems where the unbound analytes migrate in opposite directions relative to the bound complex have been investigated theoretically. However, other migration orders exist in nature, such as in the case of hybridized DNA, where two complementary, negatively charged single strand (ss) DNA migrate in the same direction relative to the double strand (ds) DNA. Recent micro- and nanofluidic NECEEM experiments with reacting DNA species ranging from 10nt to 100nt have shown the importance of channel size and ionic strength on separation as well as the importance of reaction constants,[113] [114] [3] however these experiments lack a reliable model for the effects of hybridization thermodynamics on transport. In the context of cycling temperature capillary

electrophoresis of DNA, Laachi et al. derived a robust theoretical framework to describe the denaturing and reannealing kinetics of DNA strands during a separation. [115] Their model calculates mean velocities and effective diffusivities to determine band broadening during separations, taking into account binding kinetics and transport. However, it does not address species that are fully resolved or allow for the determination of kinetic parameters from experimental data.

In this section, we simulate non-equilibrium KCE of DNA systems where analytes are of the same charge. We first validate our model using theory for typical protein systems, where the reacting analytes migrate in opposite directions relative to the complex. Next, we perform KCE of DNA, where both strands migrate in the same direction, causing changes in the observed electrophoretic mobility of the dsDNA. We investigate the important parameters that affect the observed mobility as well as the electropherogram shape, namely the dissociation constant of the system, K_D, and initial concentration of the analyte, c_0. To further validate our model, we perform microchip capillary electrophoresis experiments with ssDNA hybridizing with its perfect complement and with complements containing single nucleotide polymorphisms (SNPs) at different salt concentrations to vary K_D. Finally, we compare our results to calculated values from common thermodynamic prediction software for static systems.

DNA Under Confinement

Furthermore, Understanding DNA hybridization at the nanoscale and the effects of confinement on molecular processes has important implications for understanding cellular function and evolution. Confined or compartmentalized spaces are essential to the evolution of increased complexity in protocells and synthetic cells, since they prevent takeover of functional systems by parasitic or low-information sequences [116]. Understanding nucleic acid hybridization kinetics are particularly useful for understanding and manipulating cellular function. However, typical methods for measuring equilibrium constants are not conducive

to measurements in confined (ie. < 100 nm) systems [117] [118]. Therefore, we also exploit the miniaturization of non-equilibrium capillary electrophoresis of equilibrium mixtures (NECEEM) [3] in nanofluidic channels to determine the K_D of 20 base-pair single-strand DNA (ssDNA) in confinement and under an applied electric field. We show the dissociation constant (K_D) of nucleic acids (e.g., DNA) in confinement in non-equilibrium conditions. These results are the first time that non-equilibrium constants are determined in confinement and under an applied electric field.

3.3.2 Theory and Simulation

KCE separations are governed by the basic mass transport equation with electromigration and reaction kinetics:

$$\frac{\partial c_i}{\partial t} + \nabla \cdot (-D_i \nabla c_i - z_i \nu_i F c_i \nabla V) + u \cdot \nabla c_i = R_i, \tag{3.1}$$

where c_i is the concentration of species i, D_i is the diffusion constant, z_i is the valence, ν_i is the mobility, V is the applied voltage through the channel, u is the EOF velocity, and R_i is the reaction term. The reactions are determined according to the following equations:

$$[A] + [B] \leftrightharpoons [C] \tag{3.2}$$

$$R_A = -k_{\text{on}}[A][B] + k_{\text{off}}[C] \tag{3.3}$$

$$R_B = -k_{\text{on}}[A][B] + k_{\text{off}}[C] \tag{3.4}$$

$$R_C = +k_{\text{on}}[A][B] - k_{\text{off}}[C], \tag{3.5}$$

Furthermore, the electrophoretic velocity, $\mathbf{u}_{\text{EP},i}$ of an analyte is characterized by the electrophoretic mobility which is dependent on the equilibrium balance between the Lorentz and

drag forces:

$$\mathbf{u}_{\mathrm{EP},i} = \mu_{\mathrm{EP},i}\mathbf{E} \tag{3.6}$$

$$\mu_{\mathrm{EP},i} = z_i F \nu_i \tag{3.7}$$

Association and dissociation of complex, C, between substrate A and ligand B are characterized by a bimolecular rate constant k_{on} for association and a unimolecular rate constant k_{off} for dissociation.

And in equilibrium, the dissociation constant K_D is defined as:

$$K_{\mathrm{D}} = k_{\mathrm{off}}/k_{\mathrm{on}} = \frac{[A][B]}{[C]} \tag{3.8}$$

We performed numerical simulations of the above equations using a commercial finite element program (COMSOL multiphysics versions 4.3a and 4.4 Stockholm, Sweden). Specifically, we solved for the electrophoretic transport of three reacting species, assuming the advective velocity **u** is zero, because electroosmotic flow is simply a constant in channels with a height of 1 μm or larger and can simply be superposed to the computed electrophoretic velocity.[119] The model solves for both the electric field distribution as well as the mass transport of a finite size plug of charged analyte migrating within a straight channel. The initial concentration distribution is a top hat with plug width, w_0, with the species at given concentrations, $c_{0,\mathrm{A}}$ and $c_{0,\mathrm{B}}$. The analytes equilibrate for 20 seconds before the electric field is turned on at $t = 0$, to ensure an equilibrium concentration distribution in the initial plug similar to that performed in experiments. To test for a suitable equilibrium time, numerous simulations were performed at a range of K_D values and were allowed to equilibrate for 60 seconds. In all cases, after only 20 seconds, the three species had reached within 1% of their equilibrium values, giving the equilibrium time to be used in all simulations.

To validate our model, we compared our results with an exact analytical model [110] for the migration order $\mu_A > \mu_C > \mu_B$, where the complex electrophoretic mobility is less than the substrate and greater than the ligand (Figure 3.5). Note that the analytical solution does not account for any association reactions, effectively assuming $k_{on} = 0$. However, since the concentrations of analytes are dependent on $K_D = k_{off}/k_{on}$, assigning $k_{on} = 0$ results in an infinite K_D which is not physically realizable. As a result, there are slight differences between analytical and simulation results. Figure 3.5 shows the comparison between the models, for three K_D values (solid lines = analytical model, dashed lines = numerical model). As specified in our initial conditions, at time $t = 0$ there is an equilibrium plug with a top hat distribution $w_0 = 50$ μm wide centered at $x = 0$. We plot the analyte distributions after 16 seconds (rightmost peak is the substrate, the middle centered around zero is the complex, and the leftmost peak is the ligand). The substrate concentration distribution (right, blue peak) consists of a Gaussian peak from the initial excess substrate as well as a disassociation tail that is due to dissociation of the complex. The complex peak is affected only by dissociation and diffusion. Since the substrate and ligand migrate in opposite directions, the complex will completely dissociate after long times (when $t \gg 1/k_{off}$) and this peak will disappear. The ligand peak (left, red) has a smaller Gaussian peak from the equilibrium dependent initial concentration of unbound ligand as well as a tail that is due to dissociation of the complex peak. Our model captures true equilibrium dynamics of this migration order, as k_{on} decreases ($k_{on} = 10^4$ $M^{-1}s^{-1}$ is the lowest value in Figure 3.5), our results approach the analytical solutions (Note that values of k_{on} for DNA hybridization are larger, typically around 10^6 or 10^7 $M^{-1}s^{-1}$). [120],[121] Furthermore, our numerical model shows the limitation of this particular analytical model which assumes the forward reaction is negligible.[110] In cases where k_{on} is large the complex dissociates slower because the dissociative flux is dependent on how far the system is from equilibrium which is in turn dependent on K_D as well as the electromigration flux of the substrate and ligand away from the complex.

We theoretically probed other migration orders where the charges of the substrate and ligand are the same polarity. Since this is typical of DNA based systems where all species are negatively charged, we herein adopt a naming convention specifically for DNA. In both simulations and experiments we will always use double the concentration of one labeled ss-DNA (A) as compared to its unlabeled complement (B). In other words, there is an excess of unbound A in the initial plug which is used to evaluate separation resolution and quantify the observed electrophoretic mobility of the dsDNA (AB) peak. In the model, we assign the same diffusivity to A and B, and vary their charge to modulate the relative electrophoretic mobilities. This is to simplify the model so that we can focus directly on the effects of kinetic parameters (k_{on}, k_{off}, and K_D), and initial concentration, c_0, on the observed electrophoretic mobility and plug shape. We use a Lagrangian reference frame that moves with the velocity of A. Figure 3.6 shows an electropherogram typical of reacting DNA systems, where A and B migrate faster in a channel (or column) than AB. The figure shows three different values of K_D at $t = 30$ seconds. Here, the peak on the right is always A, and the peak on the left is AB. Note that peak A is always in excess by a factor of 2, which is why it is about the same intensity as peak AB. The most important feature to notice from this figure is that peak AB shifts in space depending on the K_D. This is because as the K_D increases, the dissociation rate increases, so there is more ssDNA in the system. This causes the dsDNA peak to move with a mobility that is closer to that of ssDNA, pushing its elution peak (AB) to the right. In other words, for an infinite K_D, peak A and peak B would simply diffuse with no separation, and with a K_D of zero, peak AB and the ssDNA peaks (A and B) would be the exact same magnitude, separating in time with no DNA present between. Also in this figure, we plot excess A and B that is not hybridized (AB) at this particular moment in time, which is in the Lagrangian reference frame, is a peak with a center at zero. This peak is larger for higher values of K_D because the dissociation rate is higher.

Using this model, we probed the effects of parameters involved in the system, including

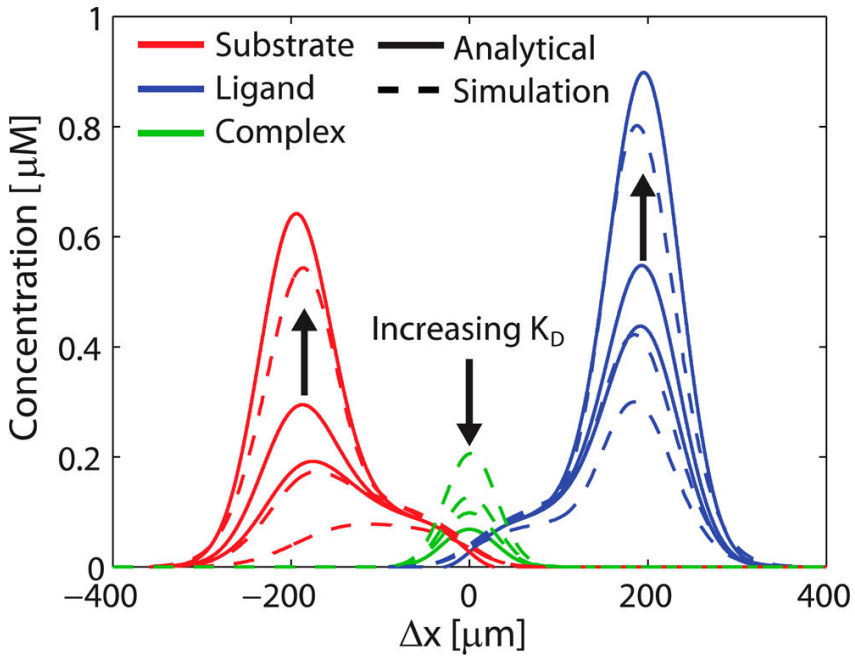

Figure 3.5: Comparison of analytical model (solid lines) to numerical simu-lation (dashed lines) for first migration order ($\mu_A > \mu_B > \mu_C$, where A = Substrate, B = Ligand, and AB = Complex) evaluated at $t = 16$ s for K_D values of 10^{-6}, 10^{-7} and 10^{-8} M with $k_{off} = 0.1$ s^{-1}. The analytical model neglects forward reactions which overestimates the rate of complex dissociation. In all cases, the analytical model predicts a lower concentration of complex and higher concentrations of substrate and ligand. Increasing K_D (by decreasing k_{on}) increases the complex dissociation rate and simulations results approach the analytical model, as shown by the similar shape in analyte distributions. Note that numerical model captures the effect of forward reactions on equilibrium dynamics as shown by slower rate of dissociation where the substrate and ligand overlap within the complex plug.

reaction constants, initial concentration, initial plug width, and differences in the DNA mobilities to determine influence of different parameters on observed effective analyte mobilities. In the analytically-verified case, electrophoresis of unbound analytes relative to the complex drives the complex plug into a non-equilibrium state. This causes the complex to dissociate to maintain equilibrium within the plug. In this case the observed electrophoretic mobility of both the unbound analytes and the complex is the true electrophoretic mobility. However, when both unbound species migrate in the same direction relative to the bound species, they can rebind downstream and form complex away from the mobility of the dsDNA in equilibrium, which causes the apparent shift in dsDNA mobility observed in Figure 3.6. Further-

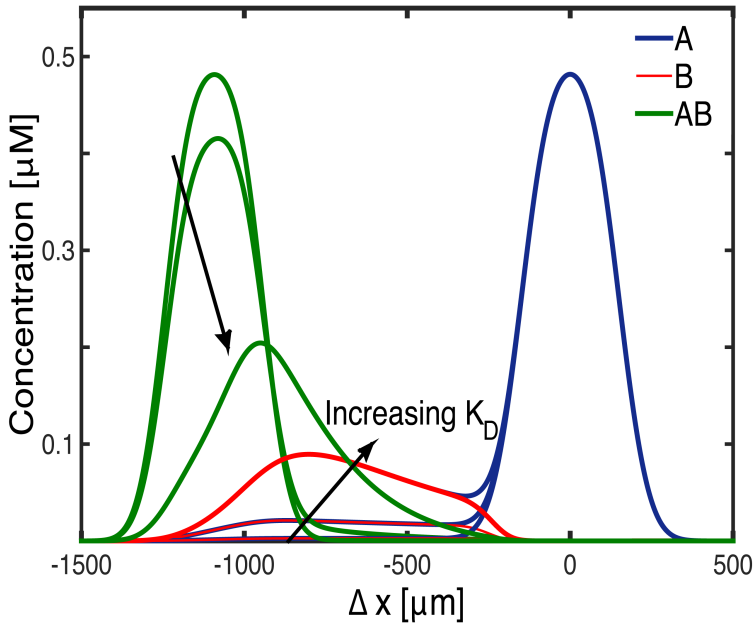

Figure 3.6: Example concentration distributions at $t = 40$ seconds for the migration order where A and B have the same charge and initial concentration of 2 μM and 1 μM, respectively. Different lines correspond to increasing K_D values of 10^{-8}, 10^{-7} and 10^{-6} M with k_{on} equal to $5 \cdot 10^4$ $M^{-1}s^{-1}$. The peak on the right (blue) is peak A which is always twice the concentration of B, and the peak on the left is peak AB (green). At the largest value of K_D, the dissociation rate is highest, so there is more ssDNA (A and B) in the system and the peak can shift more towards the true ssDNA mobility. We plot the excess ssDNA (A and B) that is not hybridized into AB at this particular moment in time (blue, A, red, B). This peak is larger for higher values of K_D because the dissociation rate is higher. Note that peak B is always closer to peak AB because its mobility is dominated by the time it spends hybridized, while peak A on the right does not spend any time hybridized because it is in such excess.

more, it is interesting to note that when K_D increases, there is more peak dispersion because it contains species with different mobilities that only exist transiently and never truly separate, resulting in a broader peak. To quantify this effect, we non-dimensionalize the observed complex peak velocity by the velocity of strand A to derive a weighted mobility we term μ_w. It can be evaluated using ratios of electrophoretic mobility, electrophoretic velocity or

electrophoretic displacement as follows:

$$\mu_w = 1 - \frac{\mu_{\text{obs,AB}}}{\mu_{\text{A}}} = \frac{u_{\text{obs,AB}}}{u_{\text{A}}} = \frac{\Delta x_{\text{AB}}}{\Delta x_{\text{A}}} \tag{3.9}$$

When $\mu_w = 1$, the mobility of peak AB is representative of the true electrophoretic mobility of AB (as in Figure 3.5). However for other migration orders, μ_w ranges between 0 and 1. The minimum value of μ_w is 0 and occurs when the observed mobility of peak AB is the same as peak A (this would appear as a single unresolved peak in a real experiment assuming A and B have the same mobilities), and describes a system with a very high equilibrium ratio of unbound (ssDNA) to bound (dsDNA). In general, the equilibrium ratio of A and B to AB (R = [A]/[AB]) is the most important factor on the weighted mobility of the complex. R is dependent on K_D and c_0: as K_D increases, R increases by the square root of K_D and as c_0 increases, R decreases as the square root of c_0. This ratio is not constant over time or space during the separation since the analyte concentrations decreases over time due to diffusion and dispersion. Therefore, numerical simulations are vital to accurately study these varying effects over space and time. Figure 3.7 shows the dependence of a weighted mobility, μ_w on K_D and c_0 of the complex. As K_D decreases or c_0 increases, μ_w decreases, and follows a sigmoidal type curve. In general, low μ_w results from a low equilibrium ratio R of A to AB, and so the electrophoretic flux of the A and B is low. In other words, the analytes are primarily in a bound state where the electrophoretic mobility is closer to the equilibrium mobility, therefore the observed change in velocity is more heavily weighted toward zero. When μ_w is high, the equilibrium ratio R is high and the analytes are primarily unbound. This results in an observed velocity that is heavily weighted toward the velocity of the A and larger observed mobilities.

In addition to probing the effects of concentration and K_D on μ_w, we performed sweeps on the initial plug width, w_0, the charge ratio between ssDNA and dsDNA, and the diffusivity D of the DNA.

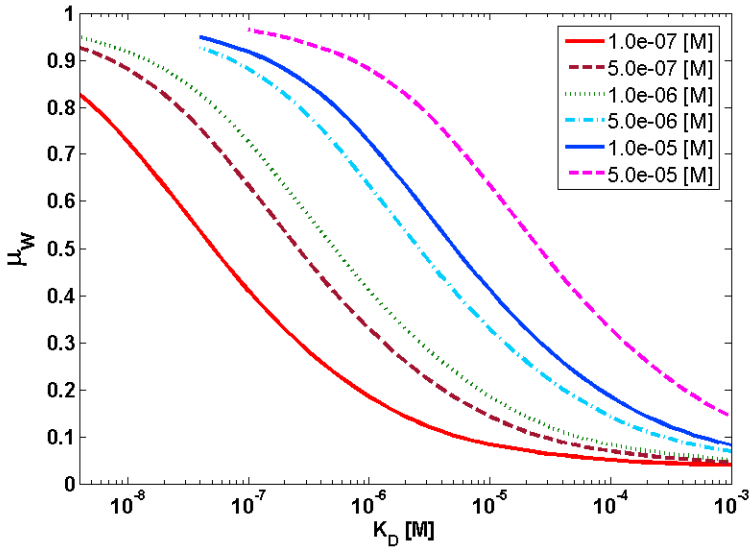

Figure 3.7: Plot of weighted mobility w for varying dissociation constant K_D for specific values of initial concentration c_0. Increasing initial concentration or decreasing K_D increases weighted mobility because of the equilibrium ratio of A to AB. Note that the gap in the data for $c_0 > 2 \cdot 10^{-6}$M and $K_D < 2 \cdot 10^{-7}$M is due to singularity errors. The surface plot is composed of 2 parametric sweeps, the first shows w across a wide K_D range K_D ranges from $5 \cdot 10^{-9}$M to 10^{-3}M and c_0 ranges from 10^{-7}M to $2 \cdot 10^{-6}$ M) and the second shows a wide range of c_0 (c_0 ranges from 10^{-7}M to 10^{-4}M and K_D ranges from $2 \cdot 10^{-7}$M to 10^{-3}M).

3.3.3 Materials and Methods

Sodium phosphate buffered solutions were prepared using a ratio 3:17 ratio of monobasic to dibasic sodium phosphate salt (Fisher Scientific) in 10, 20, and 50mM concentrations at pH 7.6 (affording concentrations of 18.5 mM, 37 mM and 92.5 mM of Na^+, respectively). All solutions were filtered with 200 nm pore size syringe filters (Nalgene, Rochester, NY) prior to use. DNA oligomers were purchased with standard desalting from Integrat-ed DNA Technologies, Inc. We use a single 10 base long primary sequence and 3 different sequences for the complementary strands. We introduce a single nucleotide polymorphism (SNP) at the end of some the complementary strands to vary the K_D. The DNA sequences and naming conventions are described in Table 3.1.

Note that in all experiments we perform, strand A is in excess, and is used to measure

Strand A	AF488-5'-AATCGTTGCC-3' ssDNA with fluorescent tag (AlexaFluor 488)
Strand B	5'-GGCAACGATT-3' Perfect complement to Strand A
Strand B' nm	5'-TGCAACGATT-3' Complement to Strand A with a single base mismatch at one end. G-C pair is substituted with a T-C pair.
Strand B'*	AF488-5'-TGCAACGATT-3' Same as Strand B' but with fluorescent label

Table 3.1: Sequences and descriptions of DNA

the arrival of both A and AB. We also examine hybridization thermodynamics with an end-mismatched sequence (B'). Finally, we investigate the effect of adding a fluorescent tag by adding a fluorescent label to give strand B'* and compare the resultant mCE behavior to the same mismatch sequence without a tag (B').

For all experiments, we performed microchip capillary electrophoresis injections in a 1 μm deep and 9 μm wide glass channel (Dolomite Ltd). The devices consist of a simple cross geometry with north, west and south channels 5 mm long and the east channel 30 mm long as shown in Figure 3.8. Electric potentials were applied to these wells using platinum electrodes (Omega Eng. Inc., Stamford, CT), connected to a high voltage sequencer (Labsmith HVS-6000D). Experiments are performed similar to that described in reference.[3]

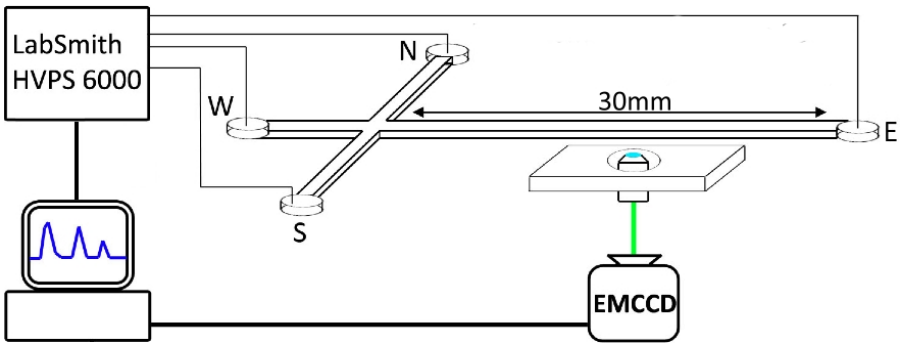

Figure 3.8: Schematic of micro- and nanofluidic cross channel and experimental setup.

Each set of experiments were performed 3 times, at 3 different buffer concentrations of 10,

20 and 50 mM of sodium phosphates (providing final concentrations of 18.5 mM, 37 mM and 92.5 mM Na^+ in solution for DNA hybridization), and 2 different initial DNA concentrations of 2 and 20 μm with fluorescein dye acting as an *in situ* mobility reference. For each case, we plot the separations as electropherograms vs the observed mobility and then horizontally align each trace to the fluorescence reference peak. By plotting the traces in this manner, horizontal shifts preserve the distance between peaks providing a convenient visual comparison that accounts for variations of absolute elution time resulting from differences in bulk electroosmotic flow and viscosity.[122] Variations in electroosmotic flow velocity did not exceed 10%.

Materials: DNA Under Confinement

We also perform new NECEEM in 100 nm, 250 nm, and 1 μm deep channels with fluorophore-tagged 22 base-pair ss- and dsDNA using a typical microfluidic electrophoretic injection protocol (Figure 3.8) [4]. The ssDNA species are individually tagged with either Fluorescein (FL) or 5-Carboxytetramethylrhodamine (TR) dyes, whose emission spectra peaks differ by 60 nm, allowing each strand as well as the dsDNA complex (which fluoresces in the TR spectrum) to be tracked individually via microscopy (Figure 3.10). At 20 mm downstream, we capture images of the DNA through the microscope over time to produce a spatiotemporal elution set, which we use to generate electropherograms shown in Figures 3.10.

3.3.4 Results

Figure 3.9 shows analyzed experimental electropherograms from our experiments. Although we varied the initial DNA concentration, buffer concentration, and DNA sequence, these variables do not have one to one relationships with K_D and c_0. For example, changing buffer concentration changes K_D, because changing salt concentration affects the ion behav-

ior near the surface of the DNA, which in turn changes the electrostatic behavior of the DNA and thus both the DNA affinity and mobility.[123] Furthermore, changing the sequence by introducing SNPs changes both K_D as well as the differences in DNA mobility resulting from the sequence dependent mobility of DNA.[124] Therefore, in order to make accurate comparisons between theory and experiments, we show data dimensionally.

Each electropherogram in Figure 3.9 shows three different cases superimposed, each with 3 experimental trials. These cases correspond to runs containing strand A with (i) B (red, solid line), (ii) B' (green, dashed), and (iii) B'* (blue, x). The peak that has the highest mobility is always strand B'*, then strand A and then hybridized AB (or AB' or AB'*), where the two ssDNA strands possess different mobilities presumably due to sequence differences.[124] In the case of 50 mM sodium phosphates buffer, (92.5 mM Na^+), the K_D is sufficiently low that most likely all the complementary ssDNA is hybridized to form dsDNA. This is why, for all three cases, there are two peaks of roughly equal intensity because the initial ratio of A to B is 2:1, leading to an A:AB ratio of 1:1. This is further verified by the fact that B'* is barely present, since it is all bound by strand A. Furthermore, in all cases, note that A has the same mobility, because they are the same exact strand, but the hybridized dsDNA (AB, AB' and AB'*) all have different mobilities. The fact that AB and AB' have different mobilities is understandable, and it is of note, too that our microfluidic system can resolve such small differences in mobility. However, we also note a small difference in mobility of AB' and AB'*. We attribute this to the fluorophore label, which likely changes the electrophoretic mobility of the duplex by changing its charge and hydrodynamic drag and could also affect DNA binding resulting in thermodynamic differences. We are able to resolve these differences via electrophoretic separations. Also, we note that the intensity of the area in between A and AB is slightly higher than the baseline in all cases, and that B is closest to baseline, then B', then B'*. This may indicate that single base mismatches do have some DNA that is not fully hybridizing, or may represent impurities in the sample, if we assume that everything should be bound at this

high salt concentration.

In the 20 mM sodium phosphates case (37 mM Na^+), where the K_D is theoretically much higher, we see that there exists much more B'* (rightmost blue peak) than in the 50 mM case, confirming that the binding affinity is lower. This is also evident in the fact that the space in between the peak A and peak AB has significant intensity, suggesting that binding and unbinding of DNA is occurring there. As expected, peak B is closest to baseline in between the two peaks, most likely because the K_D of AB is lowest. We also note that AB' and AB'* show slightly different behavior. Also note that, compared to the 50 mM sodium phosphates case (92.5 mM Na^+), the shape of the peaks are significantly non-Gaussian.

Finally, in the 10 mM sodium phosphates buffer case (18.5 mM Na^+), the peaks are the most non-Gaussian, with the least amount of space between A and AB, and a lower concentration of AB shown in the leftmost peak. Here, K_D is presumably very high, and there is considerable dissociation and re-association making the peaks very broad and poor baseline separation resolution.

Figure 3.9 shows the same experimental electropherogram for 10, 20 and 50 mM sodium phosphates (with all three trials averaged) overlaid with the best-fit theoretical simulations. Note that we chose experimentally relevant times with which to compare our simulations, such as the typical time to arrival for our experimental DNA separations. Furthermore, simulation results at these particular times produce profiles that highlight notable features for our discussion. To compare our COMSOL model with experiments, the initial plug width was calculated by multiplying the electroosmotic flow velocity (calculated with the mobility marker) with the sample loading time for each experiment. The initial concentration of each species was the same as the experimental values. Assuming rod-like structure, the diffusivity of the ssDNA and dsDNA was found to be $6.4 \cdot 10^{-11}$ and $5.1 \cdot 10^{-11}$ m^2/s respectively.[124] The apparent mobility of the ssDNA and its complement were determined by varying the k_{on} and k_{off} values, while keeping the assumed K_D value constant. Specifically, k_{on} values were

swept over the range of 10^4 to 10^7 [L mol^{-1}s^{-1}], which were in the range obtained from similar kinetic capillary electrophoresis experiments.[105],[110] Finally, the mobility values for A and B were simultaneously varied yielding a large, comprehensive parameter space from which the best match to the experimental data was chosen.

While varying the parameters in COMSOL, we noticed that peak location is affected most by the mobility values. Specifically, larger mobilities result in a greater separation between the dsDNA and the two other species. Peak shape and location are also greatly affected by the values of k_{on} and k_{off}, even for the same K_D. Therefore, both k_{on} and k_{off} as well as the dsDNA and complement mobilities (B, B' and B'*) were varied and chosen to best qualitatively match the peak shape and location of the dsDNA and complement. During the simulations, due to Lagrangian reference frames, the mobility of strand A was held at zero. Peak AB (leftmost peak) and peak A (middle peak) are used to match mobilities exactly, and for B'*, all three mobilities were varied to match experimental data. After matching all peak locations and shapes, the total intensity was normalized to match the intensity of the simulated ssDNA to that of the experimental data. A large difference in intensity for the dsDNA peaks exists between the simulation and experiment because the fluorescence emission of AF 488 varies because its quantum efficiency is sensitive to its local environment.[125],[126] This leads to a difference in emission intensity between ssDNA and dsDNA.

Table 3.2 shows the K_D values extracted from our simulations compared with those from online simulation calculators DINAMelt (http://mfold.rna.albany.edu /?q=DINAMelt/Two-state-melting) and IDTDNA Biophysics Tool (http://biophysics.idtdna.com/) at all conditions. We performed all simulations at 25 degrees Celsius. Since the online simulators cannot capture difference between adding a fluorescent label, the mismatch with a label and the mismatch without a label are the same between cases. In general, our study produced K_D values that are higher than those predicted by online programs, although in many cases within the same order of magnitude. Indeed, changing temperature in the simulator values by just a degree or

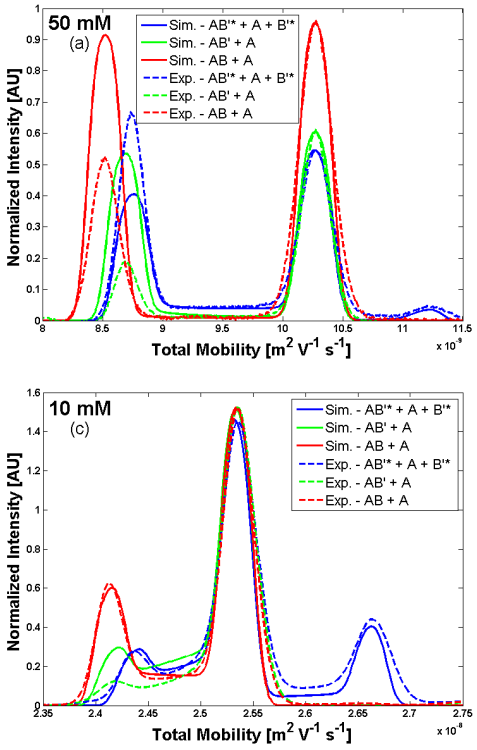

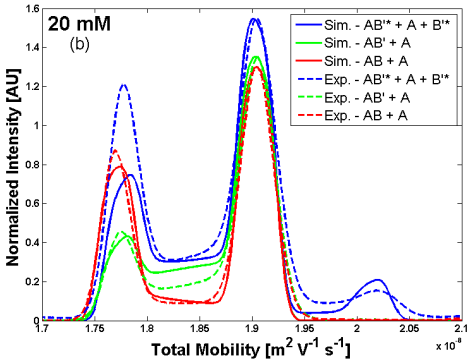

Figure 3.9: Experimental electropherogram overlaid with COMSOL fit lines at best fit K_D's. Experiments were performed with (a) 50 mM buffer, (b) 20 mM, and (c) 10 mM. Red corresponds to AB+A, blue AB'*+A+B'*, and green AB'+A.

two can allow us to exactly match values. In some cases, the differences between the two online simulator values are greater than that between our values, which indicates that our values are within error. The differences in K_D between a perfect complement and an end mismatch is about a factor of 3 (using DINAMelt), which is about the same as with our study. Finally, the effect of a second added tag in a mismatch hybridization is shown to slightly alter the K_D, which is consistent with literature pointing to the fact that dyes can modulate hybridization thermodynamics and therefore impact K_D values.

We find our K_D values to be larger in all cases than software prediction values. Greater differences are observed in lower salt concentrations while an increase in salt concentration leads to better agreement between our study and both predictor programs. Disagreement of all approaches under low salt (10 mM) confirms the difficulty with modeling such conditions where few ions are available to stabilize the phosphate backbone charge repulsions between hybridizing strands (indeed, DINAMelt and IDTDNA Biophysics disagree by an or-

10 mM	DINAMelt	IDTDNA	Our Study
Perfect Match	59.6	288	4200
SNP no label	281	2950	12000
SNP with label	281	2950	9000
20 mM	DINAMelt	IDTDNA	Our Study
Perfect Match	19.7	307	1200
SNP no label	882	371	6200
SNP with label	882	371	2400
50 mM	DINAMelt	IDTDNA	Our Study
Perfect Match	4.14	2.67	51.0
SNP no label	19.5	38.2	210
SNP with label	19.5	38.2	590

Table 3.2: Table showing K_D values (in nM) extracted from our COMSOL model (our study) as well as those calculated using online the online calculator DINAmelt (http://mfold.rna.albany.edu/?q=DINAMelt/Two-state-melting) and IDTDNA Biophysics tool (http://biophysics.idtdna.com/). All online calculations were performed at 25 degrees Celsius and 20 μm concentration of initial DNA strand with salt concentrations of 10 mM, 20 mM and 50 mM respectively (see text for resulting Na^+ concentrations).

der of magnitude in predictions at 10 mM buffer). Increased salt concentrations that approach biologically relevant amounts of monovalent ions result in good agreement between all model programs. The differences in calculations of K_D between our approach and melting temperature approaches can be partially explained first by the difference in calculations made by melting software, which assumes full DNA melting and annealing to generate estimations of entropy and enthalpy through Van't Hoff treatment of data. In our system, however, DNA is simply hybridized at a constant temperature (25 C) without any thermal denaturation, thus making it more applicable to determining K_D values in similar systems, particularly at biologically relevant temperatures for assays (e.g., molecular beacon hybridization) where thermal denaturing does not occur. Furthermore, our system is inherently more dynamic than use of melting temperature data calculations, as sequences are constantly being separated by an applied electric field, as represented by shifts in the location of the dsDNA peak in our electropherograms. Thus, when dehybridization occurs, the resulting ssDNA strands will begin to separate under the applied field, resulting in localized depletion of the sequences needed

for hybridization, effectively assisting the dehybridization process and providing a slightly higher K_D. By contrast, in a representative melting experiment, the DNA strands remain within the same solution and unable to be separated by any applied forces, providing for lower K_D values. Furthermore, our model had a greater difference than predictor values at lower salt concentration, where sulfonate groups of the AF488 dye are likely destabilizing via repulsion from the phosphate backbone, explaining the increased experi-mental K_D values, while the higher salt concentration (92.5 mM Na^+) reduced destabilizing charge repulsion and provided better agreement between our model and computational predictions.

Results: DNA Under Confinement

Figure 3.10 shows the averaged electropherograms for ss- and dsDNA in (left) 100 nm and (right) 250 nm channels. We normalize the data so that free fluorescein dye (FL - circles) elutes at zero seconds. Specifically, we show, the case for which the T-DNA (Tamra-tagged ssDNA) is in excess relative to the F-DNA (Fluorescein-tagged ssDNA).

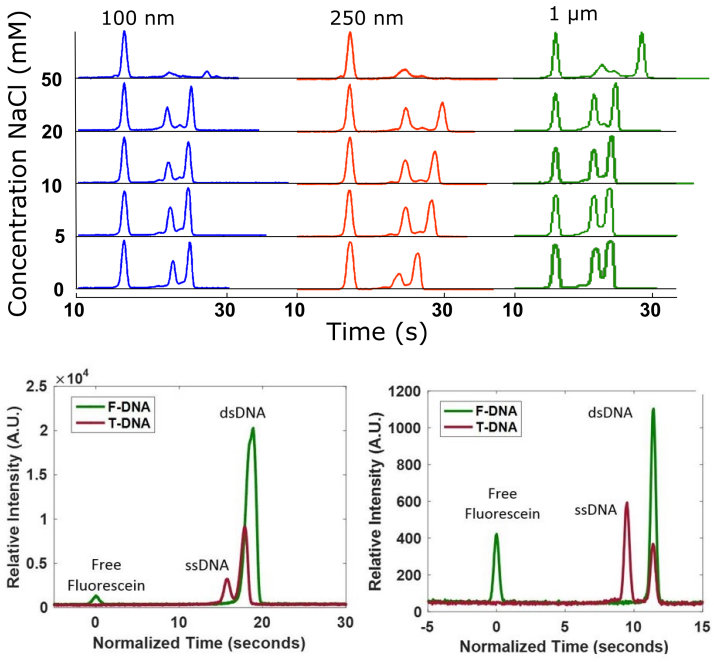

Figure 3.10: (top) Sample data from Russell et al [3] showing separation of 20 bp DNA for 3 different height channels, and (bottom) electropherograms showing fluorescein–tagged DNA (F-DNA) and Tamra-tagged DNA (T-DNA) in (left) a 100 nm channel and (right) a 250 nm channel. For both cases the Tamra-tagged ssDNA is in excess, at 30 μM relative to the 20 μM F-DNA.

Following the same approach as the microchannel cases, we show (in Figure 3.11) that increasing the level of confinement, as well as increasing background NaCl concentration, decrease the dissociation constant. K_D is determined in the same way, by matching the experiments using a least-squares fit by varying K_D and k_{on} until the peaks heights and shapes match. The other parameters necessary to perform the simulations (i.e., species mobility μ_i, initial peak width w_0, and initial concentration c_0) are obtained from the experimental results.

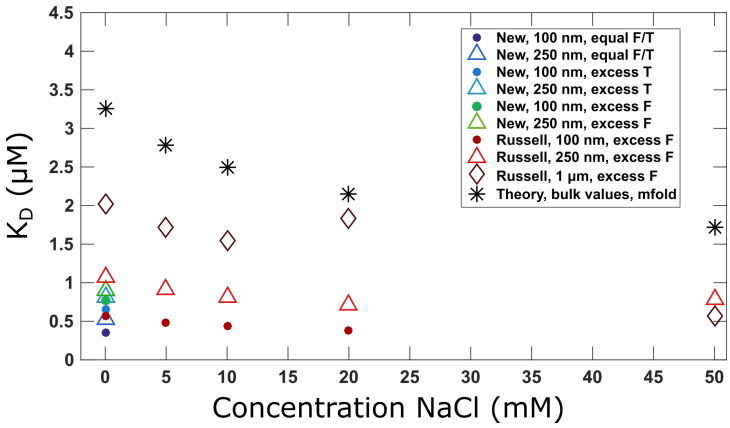

Figure 3.11: Final K_D values obtained by fitting data from the current section as well as that of Russell et al [3]. K_D decreases with increasing salt concentration as expected [4], as well as decreases under increasing confinement (for smaller channels).

These results confirm predicted behavior, that while the bulk K_D values may be large for these short DNA strands, under confinement, K_D decreases substantially. Practically, this decrease in dissociation under confinement could help cells enhance replication rates and protein synthesis. Moving forward, we are exploring actual biological experiments, collaborating with another group to confirm the observed phenomena in real cells.

3.3.5 Discussion

Our approach offers multiple advantages versus traditional melting temperature analysis to determine K_D and other KCE studies. Importantly, our method employs a single temperature to determine the dissociation constant via simulations fitting experimental results rather

than the need for complicated cycling of temperature as in traditional melting temperature experiments. This approach is inherently more biologically relevant, as using temperature control during an experiment could be performed at 37 degrees C and results fit at this temperature to rapidly determine K_D under biological conditions. Furthermore, employment of a capillary electrophoresis or microfluidic approach will greatly reduce the volume of samples needed to perform experiments needed for subsequent fitting by simulations. Finally, in all cases, we performed experiments at different initial concentrations, and although these were shown not to have a large effect on the resulting data, we do show in Figure 3.12, the ratio of peak heights (AB /A and AB'/A) at each of the different buffer concentrations and initial concentrations. The reason that we did not notice large shifts in resulting mobility is because we used high concentrations of DNA, namely 2 and 20 μM, and major differences in K_D do not occur until concentrations are down at nM. Figure 3.12 does show some interesting and expected trends, though. First, in all cases, AB/A (square) has a bigger intensity ratio than AB'/A, indicating better binding affinity. Furthermore, the 20 μM (red) always has higher intensity ratio (and thus binding affinity) than the 2 μM case (black). Finally, as salt concentration increases, the ratio increases, again showing that the trends that we capture using matching data to the electropherograms is further confirmed through experimental intensity values, something that we did not fit to in our simulations. Note that in this figure that we only show AB and AB', because AB'* gives twice as much signal, making it impossible to com-pare.

For electrophoresis in capillaries and microchannels, the goal is to achieve the best separation resolution in the shortest time with highest sensitivity. Sample is resolved when the separation due to electrophoresis between the samples is larger than both the initial plug width and the spreading of the peaks due to diffusion. From our simulation results shown here, it is obvious that increasing initial concentration, electric field, and plug width will help in achieving the highest separation resolution as well as sensitivity. Although they are all

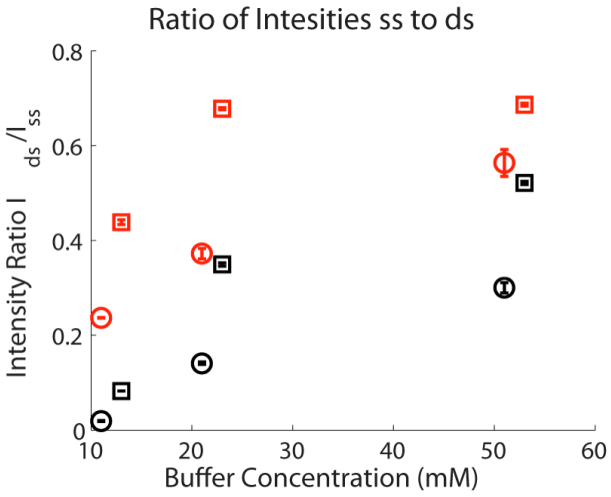

Figure 3.12: Intensity Ratios AB/A (square) and AB'/A (circle) for 20 μM concentration of DNA (red) and 2 μM concentration of DNA (black). As expected, intensity ratio increases with DNA concentration as well as with a perfect complement, indicating better binding affinity in both cases.

interrelated, as the plug width increases, the minimum time to resolve separation increases, because the weighted mobility will be closer to one for higher initial concentration and plug width. How-ever, it is important to keep the plug width on the same order of diffusion time $t_D = W^2/2D$ at the time of arrival ($t_D = t_{arrival}$) to maximize the concentration detected (and therefore sensitivity of your detection).

Furthermore, with our model, one can determine system parameters using an experimental electropherograms. For example, knowing the concentrations and mobilities of the substrate and ligand, you can find K_D using the model. These data are useful in practical situations, where we can use experimental values of electrophoretic mobility, arrival time, initial concentration, initial plug width, and electric field of each species, to calculate the K_D (either assuming a weighted mobility of zero for an experiments performed at an extreme case, or from literature values of the innate mobilities of each sample). Using these experimental mobilities, and the details of the system, one can construct a curve like Figure 3.6 and compare the experimental weighted mobility with the Figure to find the K_D. One example of using this technique is shown in Ref. [3], where we determine the K_D of complementary strands of 10 bp DNA at different ionic strengths.

3.3.6 Conclusions

In this section, we present a 1D numerical model to simulate capillary electrophoresis of charged species with reaction thermodynamics. First, we validate our model with an existing analytical model for a typical protein reacting systems. Next, we discuss results for DNA systems, where the substrate and ligand are typically of the same charge. We define an observed electrophoretic mobility, μ_w, that is dependent upon both K_D and initial concentration. We experimentally validate our model by performing microchip capillary electrophoresis measurements with 10bp ss- and dsDNA of varying K_D, and show that our model can match the profile of the resulting electropherogram. Such a model can be useful in determining thermodynamics or providing insight to reacting species with unknown reaction constants. Moreso, for the first time we show that K_D can be determined using NECEEM in nanoconfined fluidic channels. Such data and resulting analyses may have huge resulting implications for the design, evolution, and understanding of cellular systems.

Adapted with permission from [4]. Copyright 2015 American Chemical Society.

3.4 (Almost) Stationary Isotachophoretic Concentration Boundary in a Nanofluidic Channel Using Charge Inversion

To probe the electric double layer and its effect on electroosmotic flow, we conducted an experimental study to explore complex ionic species with potential applications to induce a quasi-stationary boundary for species concentration or separation in a nanochannel induced by charge inversion. Instead of using pressure-driven counter-flow to keep the front stationary, we exploit charge inversion by a highly charged electrolyte, $Ru(bpy)_3Cl_2$, that changes the sign of the zeta potential in part of the channel from negative to positive, thus changing

the flow direction. Having a non-charge-inverting electrolyte ($MgCl_2$) in the other part of the channel and applying an electric field can create a standing front at the interface between them without added dispersion due to an externally applied pressure-driven counterflow. The resulting slow moving front position can be easily imaged optically since $Ru(bpy)_3Cl_2$ is fluorescent. A simple analytical model for the velocity field and front axial position that reproduces the experimental location of the front shows that the location can be tuned by changing the concentration of the electrolytes (and thus local zeta potential). Both of these give the charge inversion-mediated boundary significant advantages over current methods of concentration and separation and the method is, therefore, of particular importance to chemical and biochemical analysis systems such as chromatography and separations and for enhancing the stacking performance of field amplified sample injection and isotachophoresis. By choosing a non-charge inverting electrolyte other than $MgCl_2$, either this electrolyte or the $Ru(bpy)_3Cl_2$ solution can be made to be the leading or trailing electrolyte. [90]

3.4.1 Motivation

Advances in microfabrication technology, and the consequent ability to precisely control geometrical features down to the sub-micron scale, have enabled the development of novel micro- and nanofluidic platforms. This new generation of miniaturized devices allows for faster analysis on smaller sample volumes, integration of multiple functionalities on the same platform, and better sensitivity at a lower cost. Preconcentration has long been used in such systems to enhance the detection of analytes. Methods for online preconcentration include sweeping with ionic detergent micelles [127], field-amplified stacking (FASS) [128], and isotachophoresis (ITP) [129]. Both FASS and ITP are nonlinear electrophoretic techniques used to preconcentrate a variety of ionic compounds. FASS uses electrolytes with different conductivities, and the resulting nonuniform electromigration fluxes create concentration in-

creases of analyte ions. In ITP, charged analytes are separated and focused based on their mobility, between a leading electrolyte (LE) and trailing electrolyte (TE) which have co-ions with respectively higher and lower effective electrophoretic mobilities than the sample ions, all with the same counterion.3 Sample ions are concentrated between the LE/TE interface when a constant voltage or current is applied across the channel, arranged in the order of their mobilities [130].

Ideally, the accumulation zone would be stationary inside the channel. This has a number of practical advantages including simplifying control of the timing and method of injection of analyte solutions and maximizing the time of preconcentration. In addition, if chemical reactions are designed to occur in the accu-mulation zone, a stationary zone simplifies the monitoring of concentrations, reactants, and products. In general, however, both FASS and ITP involve the ITP peak constantly moving through the channel. Achieving a stationary ITP peak is relatively difficult and cumbersome, mainly because to do so requires introducing a counterflow. This is generally done by adding hydrostatic pressure to oppose the LE, which requires additional equipment. The process also degrades the peak width by increasing sample dispersion [131] [132] [41]. Another method is to add counter flow with electroomosis (EOF) [133], which has its own inherent issues due to the instability of EOF over time.

In general, to achieve a stationary concentration peak while minimizing dispersion requires 1) a nanochannel with a small cross-section to reduce Peclet number and thus reduced sample dispersion [53], and/or 2) exploiting changes in surface charge to invert the electroosmotic flow [134]-[135]. Currently this is achieved by selecting the electrolyte pH [134], coating the capillary to reduce or even reverse the surface charge [136]-[137] and using sheathing electrodes [138]. While these techniques afford good control of the flow rate in EOF driven systems, they do not allow for the precise localization of the front, because it is the electrolyte type and concentration that determine the local zeta potential, and thus local EOF and concentration peak location.

Here, we exploit the phenomenon of charge inversion and isotachophoresis in nanofluidic systems to create a (nearly) stationary sample focusing zone. In charge inversion, multivalent counterions in the electrolyte accumulate at the charged walls of the device in excess needed to neutralize their surface charge. This changes the sign of the electrostatic potential in the Stern layer (e.g., from negative to positive if the surface charge is negative) and reverses the direction of EOF. Recent experiments have provided a detailed investigation of charge inversion by multivalent counterions from an analysis of streaming currents, the electric currents resulting from applying a pressure gradient along a charged nanofluidic channel containing electrolyte solutions [84]. Charge inversion has also been observed experimentally in voltage-driven ion flow [85]. In both cases, theories of charge inversion generally corroborate the experimental results [85]-[139].

In this initial proof-of-principle work, we use two adjacent aqueous electrolytes: $MgCl_2$, which does not exhibit charge inversion, and Tris(2,2' -bipyridine) dichlororuthenium(II) Chloride ($Ru(bpy)_3Cl_2$) which does. The advantage of using $Ru(bpy)_3^{2+}$ ions is that it naturally fluoresces, which allows us to easily observe and characterize the nearly stationary front. In the system, the zeta potential throughout the channel is determined solely by the ion concentrations and the natural surface charge of the fused silica. Before the application of a potential, the two electrolytes are mixed within the channel, and there is a gradient of zeta potential ranging from positive near the $Ru(bpy)_3Cl_2$ well to negative near the $MgCl_2$ well. Upon the application of a well-to-well potential, the continuously distributed electrolytes quickly form zones, one containing only $Ru(bpy)_3Cl_2$ and the other $MgCl_2$, with a sharp isotachophoretic interface. A simple theoretical analysis shows that because the $MgCl_2$ and $Ru(bpy)_3Cl_2$ solutions electroosmotically move in opposite directions, natural internal pressure gradients are created that oppose the electromigration of both Mg^{2+} and $Ru(bpy)_3^{2+}$, resulting in a stable front where the velocity of both cations is zero. In the experiments, the front velocity is not exactly zero, something we attribute to slow changes in pH within the channel. However,

this $\sim 2\mu$m/s drift is orders of magnitude slower than typically found in FASS or ITP.

The charge inversion-mediated quasi-steady concentration boundary we describe here has a number of significant advantages over current methods. Specifically, the zeta potential interface is not the result of fabrication or chemical modifications of the nanochannel, but instead depends only on the concentrations and electrophoretic mobilities of the cations. Because of this, our method does not require any special fabrication or surface chemistry modification techniques, nor does it require extra components to add counterflow, as is currently needed. Also, of practical consideration for injection control and concentration analysis, our system allows the user to prescribe the equilibrium location of the front by adjusting the electrolyte concentrations. Moreover, by using the naturally fluorescent $Ru(bpy)_3Cl_2$, it is very easy to visualize the interface so that its exact location is always known. Lastly, by working in a nanochannel with low Peclet number, any dispersion that would arise due to non-uniformities in the pressure-driven flow (i.e., Taylor-Aris based dispersion) is minimized because we are in a pure axial diffusion regime [140]-[135],[2]. A nanochannel can also potentially induce focusing of analyte in the center of the channel when electrical double layers overlap, but this future work is beyond the scope of this initial report on the method.

3.4.2 Theory

Here we present a simplified derivation for electroosmotic flow in a channel with a discrete step in zeta potential. [41] This zeta potential difference in our case is due to charge inversion caused by $Ru(bpy)_3Cl_2$. Furthermore, exploiting the isotachophoretic condition that the cations in each regime move at the same velocity [141], we can derive the position of the stationary isotachophoretic front based solely on zeta potentials of the channel in different regions and mobilities of the ions.

Location of Stable Isotachophoretic Front

Consider the electroosmotic flow in a nanochannel with a step change in zeta potential, as shown in Figure 3.10. Assuming 1) the fluid velocity is steady and only a function of the transverse position of both regions of the channel, 2) thin electric double layers, and 3) regions far from the discontinuity, using Burgreen and Nackache's analytical derivation [44] within parallel plates we can simply write the equation of average velocity in region n as:

$$v_n = \frac{\epsilon E_n \zeta_n}{\mu} + \frac{h^2}{12\mu}\left(\frac{\partial P}{\partial x}\right)_n \tag{3.10}$$

where ϵ is the permittivity of the fluid, h is the height of the channel, η is the dynamic viscosity, and $\frac{\partial p}{\partial x}$ is the pressure gradient. In region n, E_n is the (constant) electric field within each region and ζ_n is the zeta potential. An incompressible fluid requires that volumetric flow rate in all regions are equal. The assumption of steady, fully developed flow results in a pressure distribution that is continuous and piece-wise linear. Let P be the pressure at the stationary front located at $x = a$. This pressure is found by equating the fluid velocities of Equation 3.10:

$$-P = \frac{12\epsilon}{h^2}\left(E_1\zeta_1 - E_2\zeta_2\right) a\frac{L-a}{L}, \tag{3.11}$$

where L is the length of the channel.

The two adjacent electrolytes used in the experiments here have cations dissimilar in mobility but share the same counter ion (Cl^-). The interface between two such electrolytes is described by ITP [129]. The ITP relation that cations in both zones migrate at the same velocity gives

$$\mu_1 E_1 = \mu_2 E_2, \tag{3.12}$$

where μ_n is the (signed) mobility of the cation in region n. At the stationary front, the migration of $Ru(bpy)_3^{2+}$ (in region 1) is opposed by the fluid velocity in the opposite direction: $v_1 = -\mu_1 E_1$. Using this relation, we can find the location of the stable front a by combining Equations 3.11 and 3.12:

$$\frac{a}{L} = \frac{\frac{\eta}{\epsilon}\mu_{\text{RuBpy}} - \frac{\mu_{\text{RuBpy}}}{\mu_{\text{Mg}}}\zeta_{\text{MgCl}_2}}{\zeta_{\text{RuBpy}} - \frac{\mu_{\text{RuBpy}}}{\mu_{\text{Mg}}}\zeta_{\text{MgCl}_2}} \tag{3.13}$$

Equation 3.13 gives a relation that describes the location of the stable front based on fundamental system properties. Assuming that the fluid properties of the system remain constant, a is sensitive only to changes in the local zeta potential, which is determined by the composition of the local electrolyte.

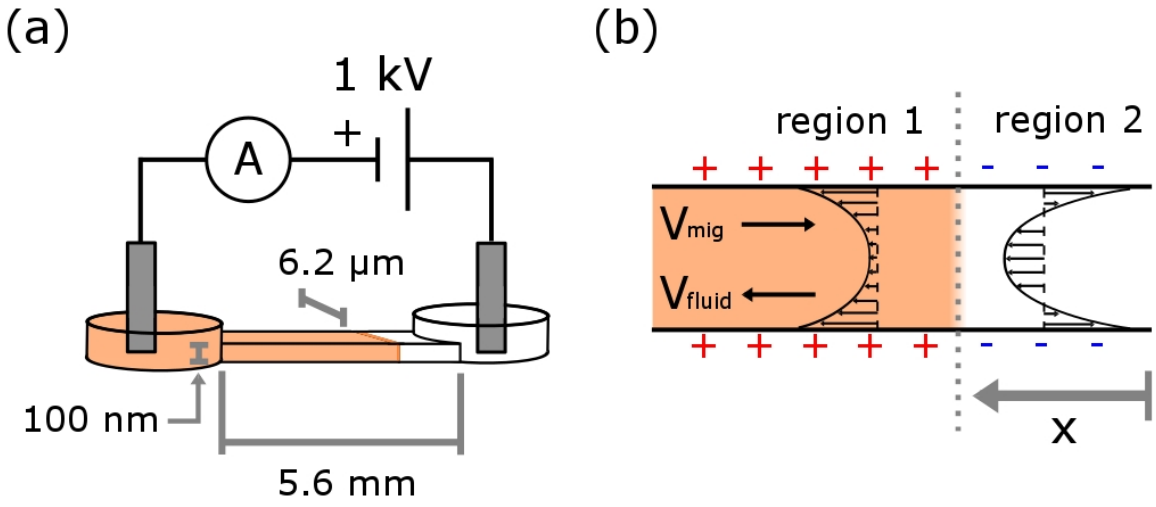

Figure 3.13: (a) Experimental setup for standing front observation. We used 6.2 µm wide, 100 nm deep, and 5.6 mm long nanochannels. (b) Schematic of the channel itself where x is the distance between the front and the well containing $MgCl_2$ The diagram illustrates that the $Ru(bpy)_3Cl_2$ zone's electrophoretic migration velocity (v_{mig}) in the proposed system is opposite in magnitude to the fluid velocity (v_{fluid}). The predicted parabolic flow in the system is depicted in the schematic. The EOF in the $Ru(bpy)_3Cl_2$ region (region 1) opposes the EOF in the $MgCl_2$ region (region 2).

3.4.3 Materials and Methods

Materials

Experiments were performed in, 5.6 mm by 6.2 μm by 100 nm straight nanofluidic channels, custom-fabricated in fused silica (Figure 3.13). These channel geometries were patterned onto fused silica wafers using conventional optical photolithography and then reactive-ion etched to a depth of 100 nm. Tolerances were 10 nm for the depth and 0.1 μm for the width. The channels were sealed by fusion bonding to a second fused silica wafer with 2 mm diameter pre-drilled wells. A schematic of channel geometry and experimental setup is shown in Figure 3.13. The fused silica chip was housed in a custom fabricated Delrin chip holder with 50 μL wells and sealed with a fluorosilicone gasket to prevent leakage and evaporation of samples. Platinum Iridium electrodes were used to apply the external potential.

Chemicals

Dry $Ru(bpy)_3Cl_2$ and $MgCl_2$ salts were purchased from Sigma Aldrich. Solutions were prepared with de-ionized filtered water at 18 MΩ/cm from Millipore Milli-Q water (EMD Millipore, Billierica, MA) and all stock solutions were measured to have a pH of 7.5. Stock solutions were prepared at 50 mM and were first filtered with 0.2 μm syringe filters (THERMO Scientific) before being diluted down to the concentrations reported in the results section.

Experimental Setup

Figure 3.13 shows a schematic of the experimental setup used for our experiments. We applied a voltage using a Keithley 2410 sourcemeter (Keithley, Inc.) and Platinum Iridium electrodes. Current was measured with a Keithley 6517a (Keithley, Inc.) electrometer for better precision. Fluorescence intensity measurements were performed on an IX71 Olympus microscope with an iXon Ultra 897 EMCCD with a 512 X 512 pixel array and 16-bit digitization. A

frame rate of 20 fps was used for all experiments. We used a filter cube (MDFM-MF2, Thorlabs) with excitation filter (D405/90x, Chroma Technology Corp), emission filter (595AF60, Omega Optical), and dichroic mirror (470dcxr, Chroma Technology Corp) to excite the $Ru(bpy)_3^{2+}$ and measure the fluorescence. We collected data with LabVIEW and analyzed all resulting data in MATLAB. Relative intensity versus the measured intensity of a DI-filled channel was calculated.

Channel Preparation

Before use, we baked all channels at 400° C for ~ 2 hours then allowed to capillary fill. After use, all channel geometries were rinsed for 10 min with 100 mM HCl to fully protonate silanol groups on the glass surface, reducing the surface charge and freeing any ions that remained from the previous experiments [1] and stored in a 1:1 DI to EtOH mixture. To minimize carry-over upon changing solutions in the reservoirs during experiments, we completely rinsed the wells three times with the new solution before voltage was applied.

Analyte and Channel Zeta Potential Characterization

We measured the bulk conductivity of both $MgCl_2$ and $Ru(bpy)_3Cl_2$ with an OAKTON PC2700 conductivity meter for all concentrations used, and we checked the $MgCl_2$ conductivities against values listed in the CRC Handbook of Chemistry and Physics [142] to ensure reliability of the values measured. Conductivity measurements of $Ru(bpy)_3Cl_2$ solutions were used to determine the mobility of the ion at a concentration of 50 mM, so that we could accurately determine zeta potential at the channel with such an ion mobility. Values are reported in Table 3.3.

We experimentally determined the zeta potential of the system for all the electrolyte concentrations used in an identical fused silica channel via current monitoring experiments25 over a range of concentrations ($30 - 70$ mM) for $MgCl_2$. Zeta potentials determined for both

Ion	Mobility $(\cdot 10^{-8}[m^2/Vs])$	Source
$Ru(bpy)_3^{2+}$	1.70	Experiment
Mg^{2+}	1.8	CRC [142]
Cl^-	-7.91	CRC [142]

Table 3.3: Ion mobilities (including valence)

electrolytes are shown in Table 3.4.

Ion	Concentration (mM)	Zeta Potential (mV)
$Ru(bpy)_3^{2+}$	30	26.94 ± 0.95
	40	27.55 ± 0.48
	50	27.89 ± 0.75
	60	27.71 ± 0.61
	70	27.53 ± 0.47
Mg^{2+}	30	-11.21 ± 0.36
	40	-9.45 ± 0.14
	50	-8.90 ± 0.29
	60	-7.86 ± 0.08
	70	-7.73 ± 0.17

Table 3.4: Measured zeta potentials

Experiments

Single nanochannels were first allowed to fill via capillary action with $MgCl_2$ for 1 min before introduction of $Ru(bpy)_3Cl_2$. It is important to note that $MgCl_2$ was the first analyte introduced, otherwise a stable front never formed, presumably because of surface adsorption dynamics of the $Ru(bpy)_3Cl_2$.[26] Therefore, for our experiments the channel was first filled with 50 mM $MgCl_2$, then 50 mM $Ru(bpy)_3Cl_2$ was introduced into the opposite (North) well (in all experiments). 500 V was applied for 100 seconds in one direction (N-S) with the South well grounded. The polarity was switched for 100 seconds (S-N) and then switched back for 100 seconds (N-S). Finally, a coincident fluorescence intensity and conductivity measurement was performed using the opposite polarity as the original (S-N) for 100 seconds. The reason for this preparation was to prevent the buildup of pH gradients and mitigate the effects of

ion depletion [143]. This process was repeated for each new concentration. Solutions were introduced in a randomized order to ensure that the measurements were not an artifact of potential hysteresis in the system. Flushing out the solutions of $MgCl_2$ took about 5 minutes; the well was flushed with the new solution three times before reapplication of voltage. During this time, the $Ru(bpy)_3Cl_2$ diffused, but the application of an electric field immediately sharpened the interface between $Ru(bpy)_3Cl_2$ and $MgCl_2$.

3.4.4 Results and Disccusion

Figure 3.14 shows a raw data time series from a typical front formation experiment. Within half a second after voltage application (Figure 3.14a), the front sharpens. The front then moves rapidly (~ 300 μm/s) for the first ~ 2 seconds, the onset period, before slowing to a relatively small drift velocity of ~ 2 μm/s towards the $MgCl_2$ (South) well. This is summarized in Figure 3.14b. This behavior is observed for all the concentrations of $MgCl_2$ used. If the voltage is turned off, the front decreases in definition only to re-sharpen at the most recent location upon reapplication of the voltage.

A stable front position is expected when the system reaches its steady-state, as described by Equation 3.13. We believe that the drift we observe is similar to the drift seen in other ITP studies [144] where changes in the zeta potential (and thus the front position) occurred because of minute changes in solution pH from the transport of ions through the channel and electrolysis at the electrodes [143]. It is important to note, however, that this drift velocity is significantly smaller than band velocities in either FASS or ITP [145].

The stable front positions found in the experiments are shown in Figure 3.15, plotted versus the concentration of $MgCl_2$ used. Using Equation 3.13, and zeta potentials and ion mobilities determined via experimental characterization in our system, we plot the theoretical value of front position, also shown in Figure 3.15. In the case of ζ_{Mg}, the zeta potential as a

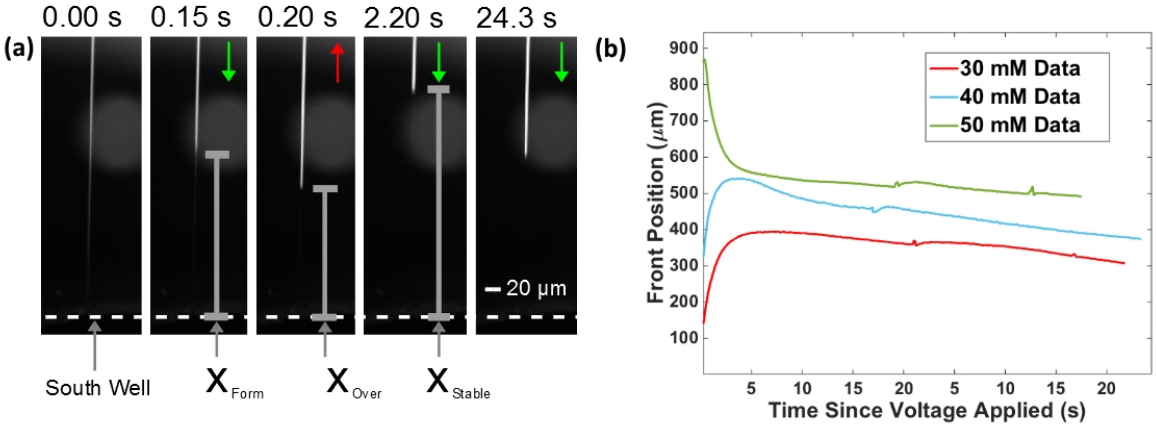

Figure 3.14: (a) Time-stamped images of front formation between $Ru(bpy)_3Cl_2$ (50 mM) and $MgCl_2$ (50 mM) in a 100 nm nanochannel. The bright vertical line originating in the North well is the fluorescence of the $Ru(bpy)_3Cl_2$. Time from application of voltage is shown above each individual frame. Colored arrows at the top show the direction the front is moving. The front is diffuse at the instant the voltage is applied ($t = 0$) but sharpens quickly ($t = 0.15$ s) before overshooting its stable position ($t = 0.20$ s). The front finally withdraws to its stable position in after a few seconds ($t = 2.20$ s) and begins to creep forward at roughly 2 μm/s until the experiment is ended at $t = 24.3$ s. (b) The time course of the front location for several experiments.

function of the $MgCl_2$ concentration was simply measured via independent current monitoring experiments (Table 3.3 and 3.4). To find ζ_{RuBpy} in terms of the $MgCl_2$ concentration, we first measured the zeta potential as a function of the $Ru(bpy)_3Cl_2$ concentration (Table 3.3) then used the Kohlrausch regulating function [141] to find the $Ru(bpy)_3Cl_2$ concentration for each $MgCl_2$ concentration.

The location of the front is not monotonic as the $MgCl_2$ concentration increases (Figure 3.15). This is a reflection of the non-monotonic behavior of the $Ru(bpy)_3Cl_2$ zeta potential (Table 3.4). That these small changes in the $Ru(bpy)_3Cl_2$ zeta potential predict the stable front position so well gives us confidence that the front position is held constant by EOF counterflow, as opposed to some other process.

Being able to tune the experimental conditions to achieve the stationary front at a desired location is one of the great advantages of our method. Moreover, it is possible to change the

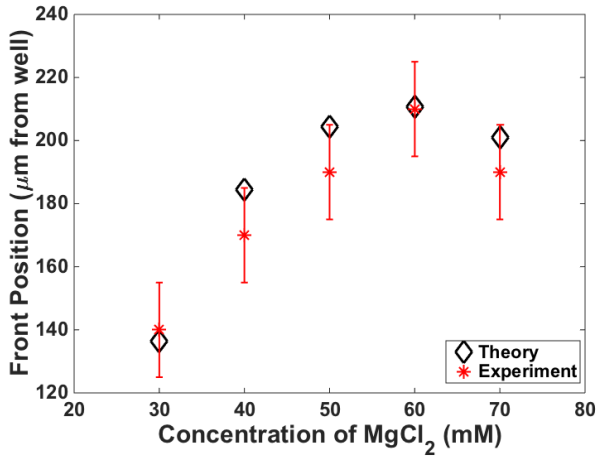

Figure 3.15: Stable front location as a function of $MgCl_2$ concentration. Theoretical values are derived from Equation 3.13 using directly measured zeta potentials and mobilities from conductivity data, as shown in Tables 3.3 and 3.4. Error bars account for drift by taking a weighted average of location over time.

front location within an experiment by changing, in our case, the $MgCl_2$ concentration. It is worth noting, however, that in practice this re-quires some care. Specifically, changes in $MgCl_2$ concentration can result in an initial overshoot of the transient front (during the onset period) past its stable location (Figure 3.14b). Moreover, this overshoot correlates strongly with the size of the change in $MgCl_2$ concentration, as shown in Figure 3.16 where the overshoot (and undershoot) is plotted as a function of the difference in concentration of $MgCl_2$ between sequential experiments. The overshoot/undershoot distance correlates strongly with the change in concentration. This suggests that this is the result of the system adjusting to a new well concentration of $MgCl_2$. Importantly however, the overshoot/undershoot does not affect the final equilibrium position reached; after stabilization, the front equilibrium position location depends only on the $MgCl_2$ concentration in that experiment. In this first proof-of-principle introduction of the charge induced-mediated stationary front method, we discuss the over-shoot/undershoot mostly for practical implementation reasons, but it is also an interesting phenomenon whose underlying cause deserves further study.

3.4.5 Conclusions

We introduce an experimental method and a general analytical model to locate the front position of a charge inversion-mediated isotachophoretic concentration boundary. The good fit between model and experimental results implies that local charge inversion by the metal-ion complex $Ru(bpy)_3^{2+}$ produces sufficient pressure gradients and counter flow to hold the position of a cationic isotachophoretic focusing front nearly constant in time. The model predicts - and experiments verify - that changing the concentration of the non-charge inverting electrolyte (in our case $MgCl_2$) changes the equilibrium position of the boundary in a predictable way. It is important to note, however, that using $MgCl_2$ as the non-charge inverting electrolyte is not required; only $Ru(bpy)_3Cl_2$ is truly necessary to induce charge inversion and visualize the front. A different electrolyte (as long as it does not induce charge inversion) will have a different mobility compared to $Ru(bpy)_3Cl_2$. This allows the user to define the leading and trailing electrolyte best suited for their specific purposes.

The method we introduce here has several advantages such as keeping dispersion to a minimum and by eliminating extra experimental components or surface coatings. The use of the fluorescent $Ru(bpy)_3Cl_2$ also allows continuous, real-time monitoring of the front location.

Here, we focused on the basics of the method in a proof-of-principle description in terms of preconcentration of analytes. However, because the method is easy to implement and highly flexible, a range of possible applications exist beyond the basic preconcentration of samples. In particular, combination of optical visualization of the front, and control of the front location merely by changing the concentration of the non-charge inverting electrolyte, can be uniquely exploited. For example, one can place analyte and/or catalyst injection sites in different prescribed locations and move the front back and forth between them. By periodically changing the concentration, one can potentially achieve localized chemical reactions in various locations with different catalysts. Moreover, this sort of charge-inversion based sta-

tionary front allows for enhanced performance of both field amplified sample injection and ITP.

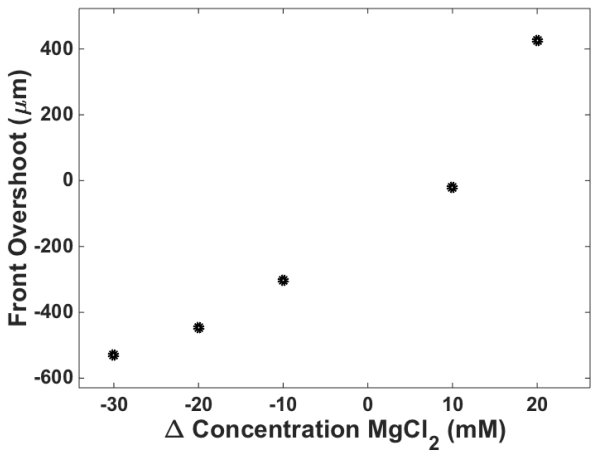

Figure 3.16: The overshoot distance versus the concentration difference of $MgCl_2$ concentration. When the concentration was decreased between experiments (negative Δ Concentration), the front formed closer to the well (negative overshoot). When the concentration was increased between experiments (positive Δ Concentration), the front formed farther away (positive overshoot).

In addition, this method provides a new way to study both ITP and nanofluidics. For example, it is generally well understood what occurs during the ITP process in microchannels [145]. Having a (relatively) stable front that can be directly visualized, gives us a new way to study the process in nanochannels. This is important because it has been shown that, in addition to ion stacking, nanochannels also exhibit ion focusing at the center of a nanochannel. Similarly, this same slow-moving, easily-tracked front will give us deeper insights into nanofluidics such as, for example, the overshoot/undershoot phenomenon in Figure 3.16, which to our knowledge has not been studied before in depth.

3.5 Moving Forward

This chapter showed that for four different projects theory can greatly improve our understanding of experiments. I employed a theoretical approach to further understand nanochannel conductivity changes based on DNA-induced surface charge changes, DNA hybridization

kinetics under non-equilibrium conditions in micro- and nanochannels, and standing front isotachophoretic-like conditions in nanochannels with complex, charge inversion-inducing species.

Furthermore, although we adequately describe the standing front induced from the complex EDL of $Ru(bpy)_3Cl_2$ using a simple mass/current conservation analysis, a more complete model that could actually predict zeta potential and current, as well as the sharp electric field gradient that arises at the interface between the two solutions would potentially lead to predictive design of novel systems. Therefore, I began to collaborate with Dr. Dirk Gillespie, an expert in Density Functional Theory (DFT), to begin a modeling endeavor of complex EDLs and fluid velocity profiles. DFT shows excellent accuracy relative to Monte Carlo (MC) and Molecular Dynamics (MD) simulations [6] [23] [7], and the fluid velocity profile under electroosmotic flow (EOF) is well-predicted using DFT [35]. Because ion concentration and EOF has been extensively studied and documented for uniformly planar surfaces, we chose to model a heterogeneity in surface charge on a planar surface. This geometry is highly relevant for numerous applications, yet a systematic study over varying counterion species and surface charges has yet to be conducted.

The following chapter presents a theoretical investigation into EDL nano-structure at the planar interface between regions of different surface charge. I show Density Functional Theory calculations that systematically probe the structure of the EDL, illustrating the lateral (parallel to the wall) and normal (perpendicular to the wall) ion oscillations that can arise at this interface. We further propose applications that take advantage of this structure such as fine electrochemical ion manipulation. For example, charged species could be manipulated near the interface via spatiotemporal tuning of surface charges.

Chapter 4

Two-Dimensional Electric Double Layer Structure with Heterogeneous Surface Charge

To adequately probe the structure of the electric double layer, we modeled a heterogeneous planar geometry consisting of two different surface charges, covering a systematic parameter set of varying counterion diameter, valence, and bath concentration, as well as the surface charges. This chapter explores the resulting lateral (parallel to the wall) and normal (perpendicular to the wall) nano-structure of the electric double layer at a heterogeneous interface between two regions of different surface charge, often found in nanoscale electrochemical devices. Specifically, classical Density Functional Theory (DFT) is used to probe a cation concentration range of 10 mM to 1 M, for valences of +1, +2, and +3, and a diameter range of 0.15 to 0.9 nm over widely varying surface charges (between ± 0.15 C/m^2). The DFT results predict significant lateral and normal-to-the-wall nano-structure in the form of ion concentration oscillations. These results are directly compared with Poisson-Boltzmann, showing significant deviation between the two theories, not only in the concentration profiles, but

also in the sign of the electrostatic potential.

4.1 Introduction

The electric double layer (EDL) at the interface between electrolytes and charged surfaces significantly affects performance of fuel cells, batteries, ion-selective channels, and other electrokinetic and electrochemical devices. While planar, impermeable, and uniformly charged walls have been predominantly studied for a variety of applications, heterogeneous surfaces are of notable interest because they can be tuned and exploited for manipulation of molecules or uncovering unique physics. For example, researchers have built heterogeneous wall charge systems to finely manipulate electrokinetic devices to enhance micromixing [8] and mimic biological nanopores for single molecule detection [9] [10] [11]. To date, most studies of heterogeneous wall charge systems use forms Poisson-Boltzmann (PB) theory and modified forms [146] [147] [148] [149], are experimental [41], or use computationally-intensive Molecular Dynamics (MD) simulations [86]. Furthermore, the details of the parallel to the wall (lateral) and perpendicular to the wall (normal) nano-structure (referred to hereafter simply as structure) of the double layer in heterogeneous systems and modalities to exploit this structure are still unknown. A comprehensive study of the structure of the EDL at a surface charge discontinuity and the effect of ion valence, concentration, size, and surface charge is crucial to understanding local and peripheral ion transport and fluid flow, especially at the nanoscale, which can potentially be exploited for novel bioanalytical and energy applications.

Figure 4.1 shows the simplest embodiment of a system with heterogeneous surface charge: a single discontinuity on a planar surface. Although many techniques (Monte Carlo (MC) [19] [20], Molecular Dynamics (MD) [21] [22] [23] [24], or Density Functional Theory (DFT) [25] [26] [27] [28]) can effectively model the discontinuity and ion correlations that lead to complex EDL structure, DFT is particularly well-suited because it accounts for the finite size of

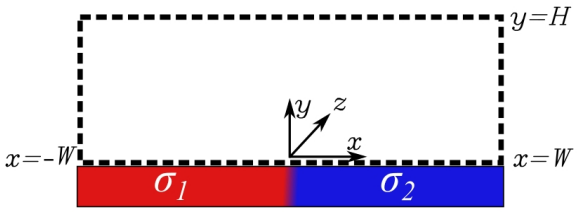

Figure 4.1: Schematic of a heterogeneous planar surface with two surface charges, focusing on the region of interest. H is the height, and W is the half width for which we computed concentrations. In this chapter, x and y refer to the lateral (parallel to the wall) and normal (perpendicular to the wall) dimensions, respectively. The system is homogeneous in the z dimension because of the symmetry of the system.

ions as well as more complex ion-ion electrostatic effects in a computationally efficient manner [150] [7]. DFT accurately models EDL structure for uniformly-charged planar surfaces as compared to MC, including in regimes such as high surface charge and high ionic strength for which PB is not sufficient [6] [7] [151]. Moreover, because DFT captures complex phenomena such as charge inversion [139] [152] and layering [35] [153], DFT should also serve well to model the transition between two surface charges and the lateral structure arising from the interaction between the two EDLs.

In this chapter, we report and discuss both normal and lateral EDL structure at the solid-liquid interface of a wall with a single discontinuity in surface charge, showing that the interface near the discontinuity can be substantially more structured than indicated by PB. For example, in cases with high surface charge differences, the resulting structure perpendicular to the wall can create structure parallel to the wall. After defining the system and theory, we explore structure in both dimensions, as well as the width of the transition, characterizing all three by comparing with PB to show the extent to which the complex physics at the transition affect the peripheral ion and potential distributions. Finally, we comment on the potential applications and methods to exploit electrochemical heterogeneous systems.

4.2 Experimental

4.2.1 Model of the System

We modeled the system as a binary electrolyte near a hard, planar, charged surface with an implicit solvent of uniform dielectric constant, ϵ_r. For this system, the temperature $T = 298.15$ K, and the dielectric constant $\epsilon_r = 78.4$.

To adequately probe a large parameter space, we used cations of different size, valence, and concentration for different surface charge σ_1 and σ_2 values (Table 4.1). Each calculation had one positive and one negative ion species. The cation species varied, while the anion remained the same with 0.3 nm diameter with -1 charge, yielding a final data set of 832 EDL structures (a subset of the possible combinations shown in Table 4.1).

Value	Min	Max	Number of Values
Diameter [nm]	0.15	0.9	4
Valence	+1	+3	3
Concentration [M]	0.01	1	3
Surface Charge [C/m^2]	-0.15	0.15	13

Table 4.1: Table of parameter values for calculations

4.2.2 Density Functional Theory

DFT accurately calculates the ensemble average ion density and electrostatic potential profiles for a system in chemical equilibrium with a bath by taking into account hard-sphere (HS) and screening (SC) excess free energy components. Given their finite size, ion cannot overlap, and the HS contribution accounts for the pressure work necessary to insert a hard sphere. The SC component accounts for electrostatic correlations beyond the mean-field potential of inserting an ion within a screening length of other ions. Therefore, both components check for other ions within a radius or a screening length, thereby leading to convolutions

as in Equation 4.2. Specifically, we use the White Bear functional [26] for the HS component and the functionalized Mean Spherical Approximation (fMSA) [7] for the SC component.

The functionals used are currently the most accurate forms of DFT, relative to one-dimensional Monte Carlo simulations. The White Bear functional has been the most accurate HS functional used for over a decade, and the fMSA has proven at least as accurate as the Bulk Fluid [27] or RFD [28] functionals, as shown by Roth and Gillespie when they compared the fMSA functional to over 20 different one-dimensional MC simulations [7]. Additionally, the fMSA has significant speed improvements relative to the RFD functional, meaning the systematic study performed was a reasonable undertaking.

For each ion species i, is the concentration profile is given by:

$$\begin{aligned}\rho_i(x,y) = \rho_i^{\text{bath}} \exp\left(-\frac{\Delta\mu_i^{\text{ex}}\left[\{\rho_k(x,y)\};x,y\right]}{kT}\right)\cdot \\ \exp\left(-\frac{z_i e_0 \phi\left[\{\rho_k(x,y)\};x,y\right]}{kT}\right)\cdot \\ \exp\left(-\frac{\mu_i^{\text{ext}}(x,y)}{kT}\right),\end{aligned} \tag{4.1}$$

where ρ_i^{bath} is the bath concentration, $\Delta\mu_i^{\text{ex}} = \Delta\mu_i^{\text{HS}} + \Delta\mu_i^{\text{SC}}$ is the difference in excess chemical potential between the system and the bath, z_i is the species' valence, e_0 is the elementary charge, ϕ is the solution to the Poisson equation ($\phi = 0$ in the bath far from the wall) , μ_i^{ext} is the external potential due to the charged wall (i.e., ions were given an infinite penalty for approaching the wall nearer than one ion radius), and kT is the product of the Boltzmann constant and temperature.

Since the excess chemical potentials are functionals of the densities, we must compute the densities numerically. The fixed-point Equation 4.1 was iterated until convergence was achieved, using an optimized Picard iteration [37]. The excess chemical potentials were cal-

culated via convolutions, which are, in general,

$$\int f(\mathbf{r}')\omega(\mathbf{r}-\mathbf{r}')\mathbf{dr}', \tag{4.2}$$

where $f(\mathbf{r}')$ is either the true or weighted ion density. The DFT weight functions [26] [7] are

$$\omega_i^{(2)}(\mathbf{r}) = \delta\left(|\mathbf{r}| - R\right) \tag{4.3}$$

$$\omega_i^{(3)}(\mathbf{r}) = \theta\left(R - |\mathbf{r}|\right) \tag{4.4}$$

$$\omega_i^{(\mathrm{V2})}(\mathbf{r}) = \frac{\mathbf{r}}{|\mathbf{r}|}\delta\left(|\mathbf{r}| - R\right) \tag{4.5}$$

$$\omega_i^{(\mathrm{SC})}(\mathbf{r}) = \frac{1}{|\mathbf{r}|}\left(|\mathbf{r}| - \lambda_{ij}\right)^2 \cdot \theta\left(R_{ij} - |\mathbf{r}|\right), \tag{4.6}$$

where δ denotes the Dirac delta function, θ denotes the Heaviside function, and R is the radius of interest. This radius is either R_i (the radius of ion species i) or the screening length, $\lambda_i = R_i + \frac{1}{2\Gamma}$, where Γ is the screening parameter [27], which, in the limit of point charges, is equal to $\kappa/2$, where κ is the Debye-Huckel screening parameter, and where $\lambda_{ij} = \lambda_i + \lambda_j$ and $R_{ij} = R_i + R_j$. In our 2D geometry, the densities only depend on the x and y coordinates, so after integrating over z dimension (see Figure 4.1), the weight functions become [150]:

$$W_i^{(2)}(x,y) = \frac{2R}{\sqrt{\tau(x,y,R_i)}} \cdot \theta\big(\tau(x,y,R_i)\big) \tag{4.7}$$

$$W_i^{(3)}(x,y) = 2\sqrt{\tau(x,y,R_i)} \cdot \theta\big(\tau(x,y,R_i)\big) \tag{4.8}$$

$$W_i^{(\mathrm{V2})}(x,y) = \frac{2\sqrt{x^2+y^2}}{\sqrt{\tau(x,y,R_i)}} \cdot \theta\big(\tau(x,y,R_i)\big) \tag{4.9}$$

$$\begin{aligned} W_i^{(\mathrm{SC})}(x,y) = \Bigg[& -(4\lambda_{ij} - R_{ij})\sqrt{\tau(x,y,R_{ij)}} \\ & - \frac{1}{2}\left(2\lambda_{ij}^2 + (x^2+y^2)\right)\ln\left(\frac{R_{ij} - \sqrt{\tau(x,y,R_{ij)}}}{R_{ij} + \sqrt{\tau(x,y,R_{ij)}}}\right)\Bigg] \cdot \theta\left(\tau(x,y,R_{ij)}\right), \end{aligned} \tag{4.10}$$

where $\tau(x, y, R) = R^2 - (x^2 + y^2)$.

The domain of interest was defined in Figure 4.1 with dimensions of H by $2W$. The Fast Fourier Transforms (FFTs) used to compute the convolutions in Equation 4.2 were calculated in Matlab (R2016a, The MathWorks, Inc., 2016), although any software package that convolves lists can be used. The complete computational domain was padded to insulate the data from artifacts of periodicity [154] and achieve 2^N points (for FFT efficiency). Because the calculations involve list convolutions, the only requirement is that the padding is larger than the kernel length. Specifically, the padding and boundary conditions for $y < 0$, $y > H$, and $|x| > W$ are given by:

$$\rho_i(x, y > H) = \rho_i^{\text{bath}} \tag{4.11}$$

$$\rho_i(x, y < 0) = 0 \tag{4.12}$$

$$\rho_i(x < -W, y) = \rho_i(x = -W, y) \tag{4.13}$$

$$\rho_i(x > W, y) = \rho_i(x = +W, y). \tag{4.14}$$

The numerical grid was uniformly spaced at $\Delta x = \Delta y = 0.01$ nm for all calculations, and the H and W values were both 25 nm for the 10 mM cases, 12 nm for the 100 mM cases, and 7 nm for the 1 M cases. Profiles with smaller grid spacings were not visibly different (not shown).

4.2.3 Poisson-Boltzmann

We compared our results to PB calculations. Specifically, we used a modified form termed the distance of closest approach PB (DCA-PB) for which the ions are only allowed to approach the wall to within one radius [32] [33]. This formulation allows different sized ion to be accounted for and includes the gap between the wall and the charge of the ion [139] [36].

These are absent when point charges can approach the wall. Furthermore, DCA-PB enables an easier comparison with DFT because all of the ion concentration profiles begin at the same point away from the wall. The PB results were calculated by setting the HS and SC contributions to zero, but still including mean-field electrostatic potential and the external wall potential, which defines each species' distance of closest approach to the wall.

4.3 Results and Discussion

To characterize the EDL of the heterogeneous junction, we investigate the two-dimensional ion nano-structure at the interface and the width of the lateral (parallel to the wall) transition region. In general, lateral profiles differ qualitatively and quantitatively from PB, sometimes creating a wider transition region when lateral ion concentration oscillations are present, and other times creating a narrower transition width compared to PB.

4.3.1 Structure

EDL structure perpendicular to the wall appears in two primary forms: charge inversion and ion density oscillations. In this thesis, charge inversion is defined as a change in sign of the electrostatic potential in the normal direction near a charged surface. Charge inversion, studied extensively at least since the 1980's via MC simulations [19] [155] [83] and explored further both computationally and experimentally [156] [84] [85], occurs in particular for multivalent counterions. The second phenomenon, oscillations in the ion density profile, which in its extreme becomes ion layering (i.e., very low ionic concentration between peaks), generally occur at high packing fraction or for large counterion diameter [157] [35] [153].

We found that lateral structure, on the other hand, appears as oscillations in ion concentration and electrostatic potential profiles and forms solely when structure exists perpendicular to the wall, although this normal structure can exist on its own. For example, Figure 4.2 shows

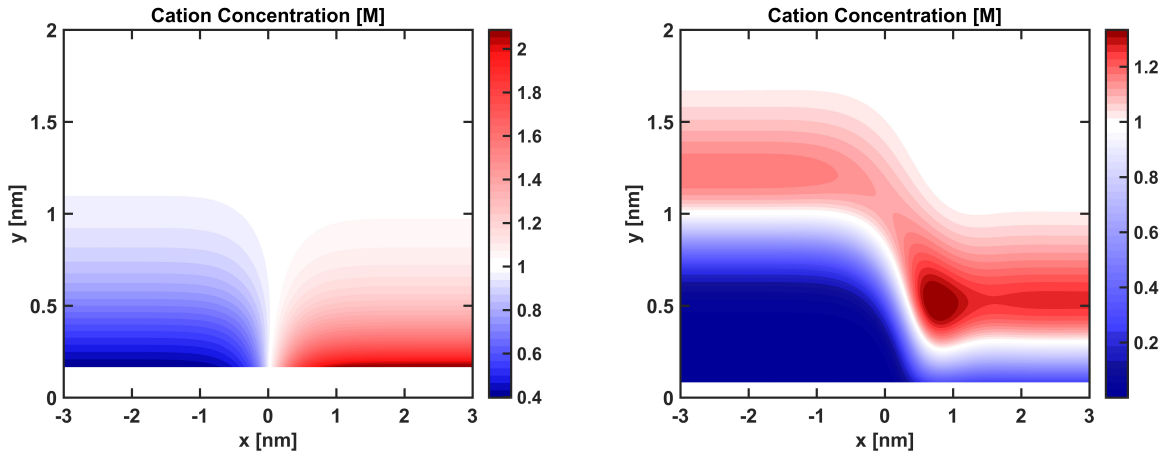

Figure 4.2: Normalized cation profiles for (left) the 0.3 nm diameter monovalent cation at 1 M concentration and (right) the 0.15 nm diameter trivalent cation at 1 M concentration. Surface charges are ± 0.05 C/m^2 for $\pm x$, respectively. (left) As expected, the cation is depleted near the positive surface charge and in excess near the negative with a monotonic lateral transition. (right) In contrast, the small trivalent exhibits depletion even for $x > 0$, as well as non-monotonic perpendicular- and parallel-to-the-wall structure. The small diameter of the cation causes this depletion for $x > 0$ because the smaller, trivalent cation approaches the wall closer than the anion, creating a region of high positive surface charge. Therefore, the system, minimizing the free energy, minimizing the amount of cations in this region to attempt to prevent large electrostatic potentials. Depletion of the smaller species near the surface has been previously documented via MC simulations for zero surface charge [5] [6] [7]. When the surface charge increases, the contact concentration increases and eventually becomes greater than bulk. We compared one-dimensional MC simulations to DFT for this case (data not shown), confirming the DFT accuracy as well as the depletion and concentration bump at 1 M.

two 2D profiles, one with a lack of structure (left) and another with considerable structure (right). For symmetric monovalent ions of the same diameter (left), normal and lateral profiles remain monotonic. The small, trivalent cation (right), however, induces significant EDL structure with both normal and lateral non-monotonicity, even containing of a localized spot of excess cations. These profiles represent two extreme cases of the entire range we studied, with a myriad of different intermediate profiles occurring as cation valence, diameter, and concentration were varied.

Highlighting six representative examples of this intermediate range, Figures 4.3—4.8 compare DFT and PB ion concentration, electrostatic potential, and excess chemical potential

profiles for different cases. We especially feature the influence of the excluded volume and screening excess chemical potentials on the ion concentration (in Equation 4.1) since PB does not account for these contributions. All these examples have the same surface charge configuration, with $\sigma_1 = +0.05$ and $\sigma_2 = -0.15$ C/m^2, but vary in cation diameter, valence, and concentration. In each figure, the panels show (A) cation concentration, (B) anion concentration, (C) cation hard-sphere and screening components, and (D) mean-field electrostatic potential.

To begin, Figure 4.3 shows the ion concentration and potential profiles for a 0.15 nm

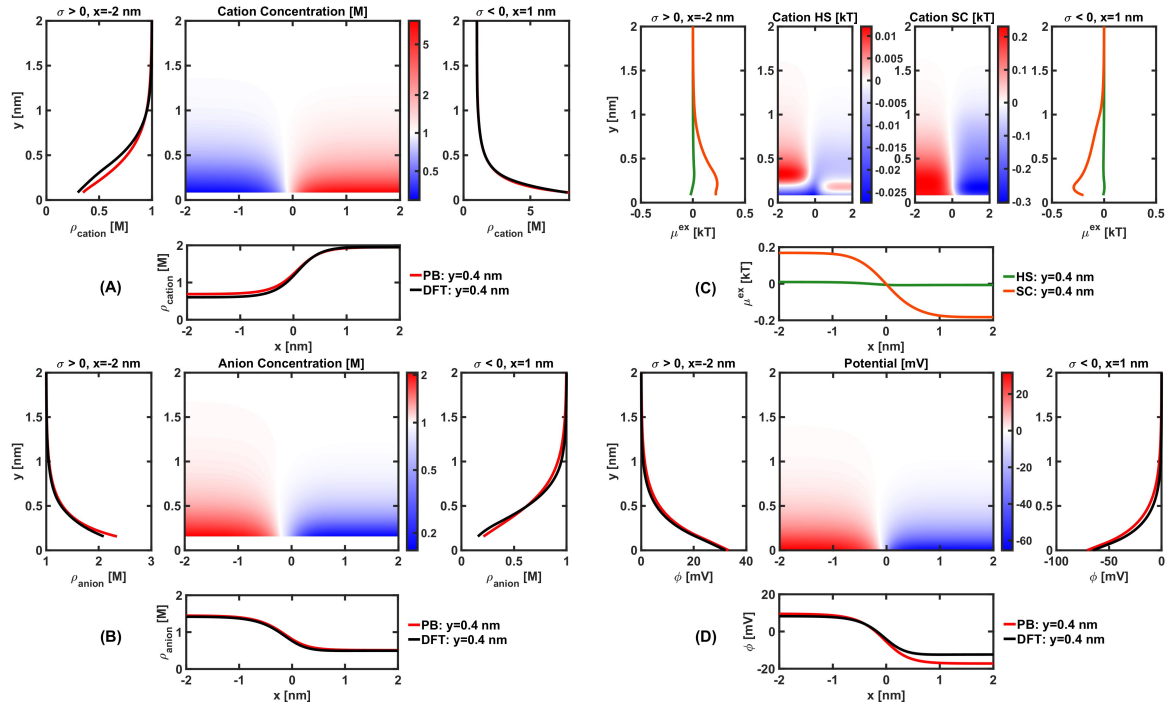

Figure 4.3: Various 2D profiles from the case of a 0.15 nm monovalent cation at 1 M concentration with plots from DFT of (A) cation concentration, (B) anion concentration, (C) cation HS and SC potential, and (D) mean-field electrostatic potential, as well as cross-sectional profiles comparing PB (red) and DFT (black) in the lateral-to-the-wall (bottom curves) and normal-to-the-wall (left and right plots) directions. The DFT curves are slices of the full 2D image, with the normal and lateral profiles taken at the specified x and y positions, respectively, which are then compared to PB (2D plots not shown). For this case, $\sigma_1 = +0.05$ and $\sigma_2 = -0.15$ C/m^2. In this color scheme, white in the 2D plots corresponds to zero potential or the bath concentration.

diameter monovalent cation at 1 M concentration. Both concentration profiles, and therefore also the electrostatic potential profile, are very similar to PB, exhibiting purely monotonic behavior with no normal or lateral structure. The ion concentration and potential profiles for DFT and PB are the same because the low packing fraction and small charge produce minimal HS and SC contributions, respectively. Specifically, even though the SC term is an order of magnitude larger than the HS, both are only a fraction of a kT and so have little impact on the ion profiles. Therefore, in general, with small, monovalent ions, even at relatively high concentration, PB suffices as a modeling tool for heterogeneous systems [157].

In contrast to the small monovalent cation, the large diameter, monovalent cation in Figure 4.4 induces oscillations in the cation and anion concentrations perpendicular to the wall, as well as non-monotonicity in the electrostatic potential. In general, large monovalent

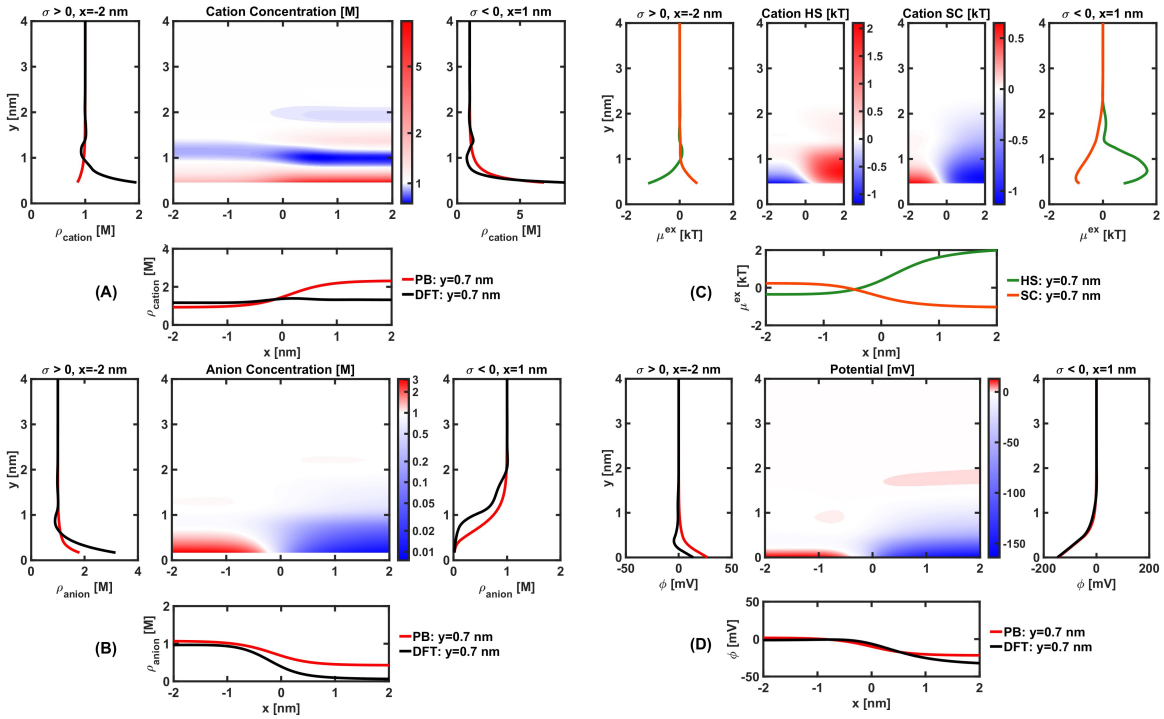

Figure 4.4: Case of the 0.9 nm monovalent at 1 M with plots from DFT of (A) cation concentration, (B) anion concentration, (C) cation HS and SC potential, and (D) mean-field electrostatic potential. See the caption of Figure 4.3 for more details.

cations can have strong layering perpendicular to the wall for large negative surface charges [153], which is confirmed in this case. Figure 4.4A also shows that the large monovalent cation concentration will oscillate mildly even for the positive surface charge when it is the co-ion. This structure is due to the considerable excluded volume contribution which is two orders of magnitude larger than the previously-shown small monovalent cation (compare the green lines in Figures 4.3B and 4.4B). Consequently, the perpendicular-to-the-wall ion structure induces a change in sign of the potential for $x < 0$, although, coincidentally, the DFT and PB potentials are the same for $x > 0$ on the scales shown.

In the lateral direction, there is only minor structure present in this case even though a large difference in surface charge is present. However, significant lateral structure is possible for large monovalent cations for much higher surface charges (not shown). In the end, PB poorly predicts the ion concentrations, and the similar normal potentials are a coincidence.

As compared to monovalent cations, divalent cations can induce different forms of structure perpendicular to the wall, and more significant structure parallel to the wall. This is shown in Figures 4.5 and 4.6. Because of the lower concentration (100 mM) and small cation diameter (0.3 nm) in Figure 4.5, the DFT and PB ion concentration and electrostatic potential profiles appear similar. However, a significant anion bump is present for both divalent DFT cases as well as charge inversion for the 0.6 nm cation, leading to considerably different lateral potential profiles relative to PB. Furthermore, while PB appears to model general trends for this system (with the exception of the normal anion concentration profiles), DFT reveals finer normal structure and some lateral structure, which becomes even more pronounced with a diameter of 0.9 nm (not shown). In Figures 4.5 and 4.6, the large screening contribution, due to the higher valence (the screening term scales roughly as valence squared)[7], produces slight lateral non-monotonicity. Both the 0.3 nm and 0.6 nm divalent cation cases exhibit a similar anion bump, although the larger divalent shows more significant deviation from PB, with considerable lateral structure and charge inversion.

The trivalent cation profiles shown in Figures 4.7 and 4.8 induce all forms of normal and lateral structure, with major contributions due to screening. For example, the 0.3 nm trivalent cation in Figure 4.7 exhibits significant charge inversion and lateral structure. The largest trivalent (0.9 nm) in Figure 4.8 induces even more substantial lateral structure, as well as notable charge inversion and a large excess anion concentration bump in the normal direction for $x > 0$. This charge inversion leads to qualitatively different lateral electrostatic potential profiles as compared to PB. For example, in Figure 4.7, the DFT potential always has the opposite sign relative to PB, and, in Figure 4.8, the lateral potential is non-monotonic and positive for all x, while the PB potential goes monotonically from positive to negative.

Additionally, the considerable screening contribution ($> 10\ kT$ for the largest cation) remains a remarkable feature of the trivalent cases and the largest deviation from PB. Many

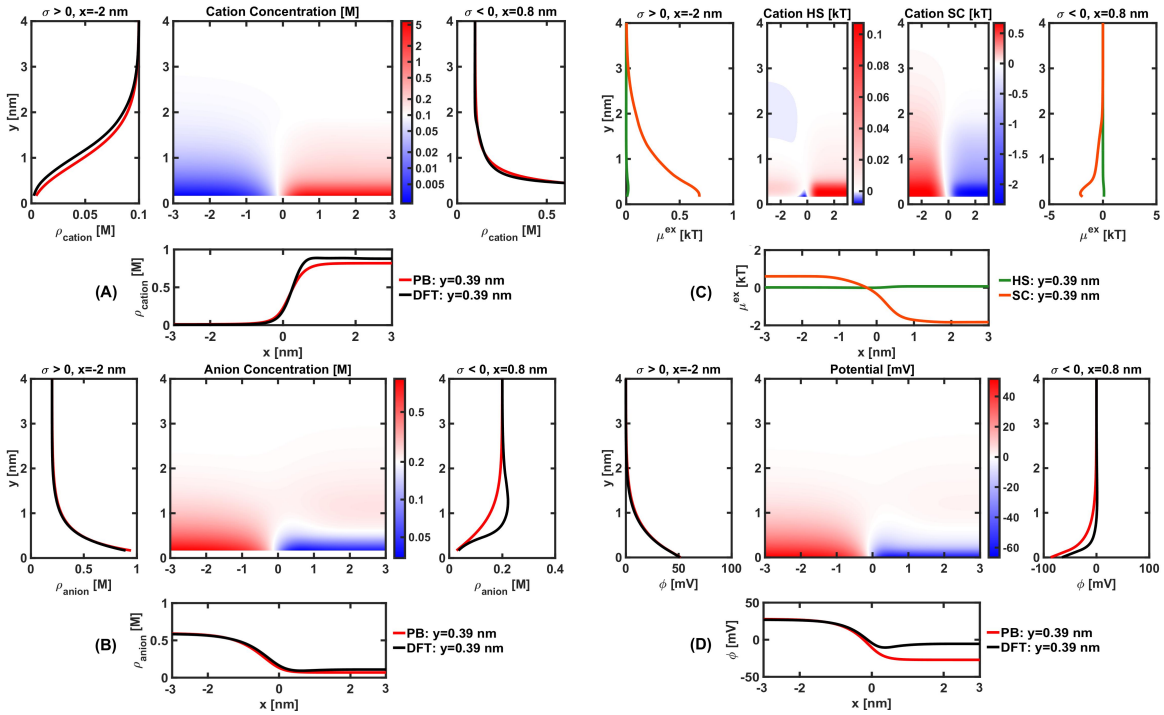

Figure 4.5: Case of the 0.3 nm divalent at 100 mM with plots from DFT of (A) cation concentration, (B) anion concentration, (C) cation HS and SC potential, and (D) mean-field electrostatic potential. The normal cation profile for $x > 0$ was truncated for easier viewing. See the caption of Figure 4.3 for more details.

theories [17] [29] attempt to improve on traditional PB by accounting for excluded volume effects, yet still neglect these screening effects [36]. This proves problematic since the screening component can be several kT and orders of magnitude larger than the excluded volume component that these theories include (see Ref. [36] for more discussion). On the whole, the trivalent cases exemplify the need for accurate theories beyond PB.

Here, we highlighted six cases showing that mulitvalent and large cations induce significant normal and lateral structure. We see ion concentration oscillations and electrostatic potential charge inversion, complex behavior for which the entire 2D profiles are needed. Even so, we will try to condense the 2D data into a single value to enable a more straightforward characterization of lateral structure present in the DFT calculations.

To do that, we will quantify lateral structure manifested in the DFT cases, with the trun-

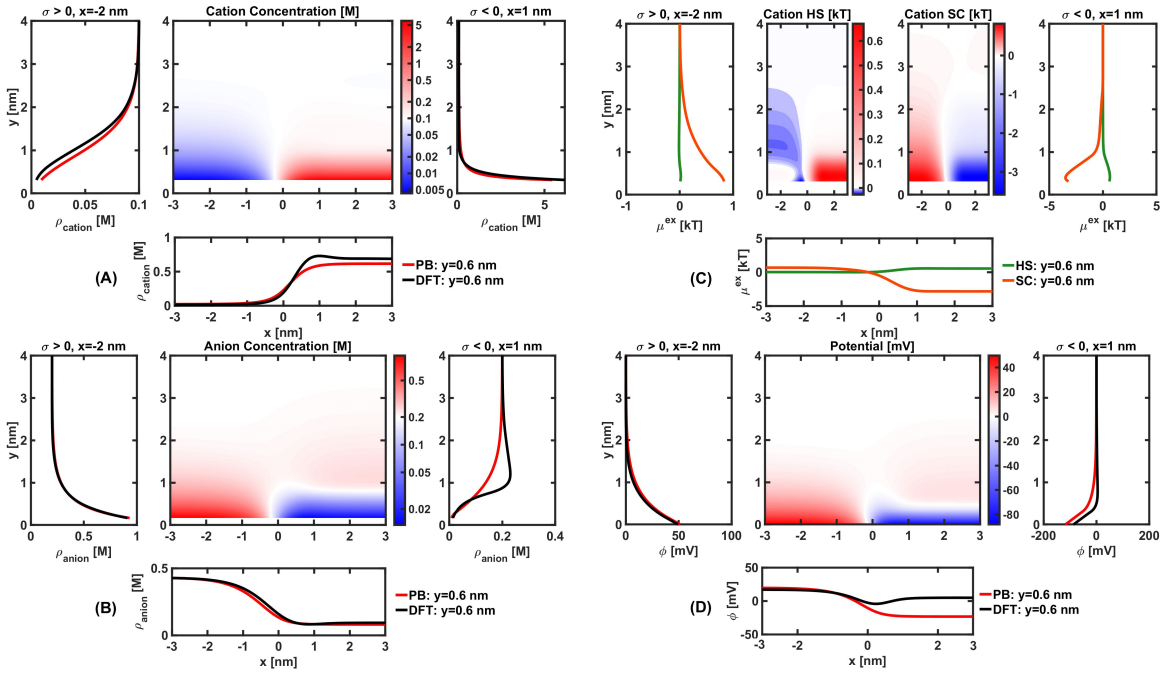

Figure 4.6: Case of the 0.6 nm divalent at 100 mM with plots from DFT of (A) cation concentration, (B) anion concentration, (C) cation HS and SC potential, and (D) mean-field electrostatic potential. See the caption of Figure 4.3 for more details.

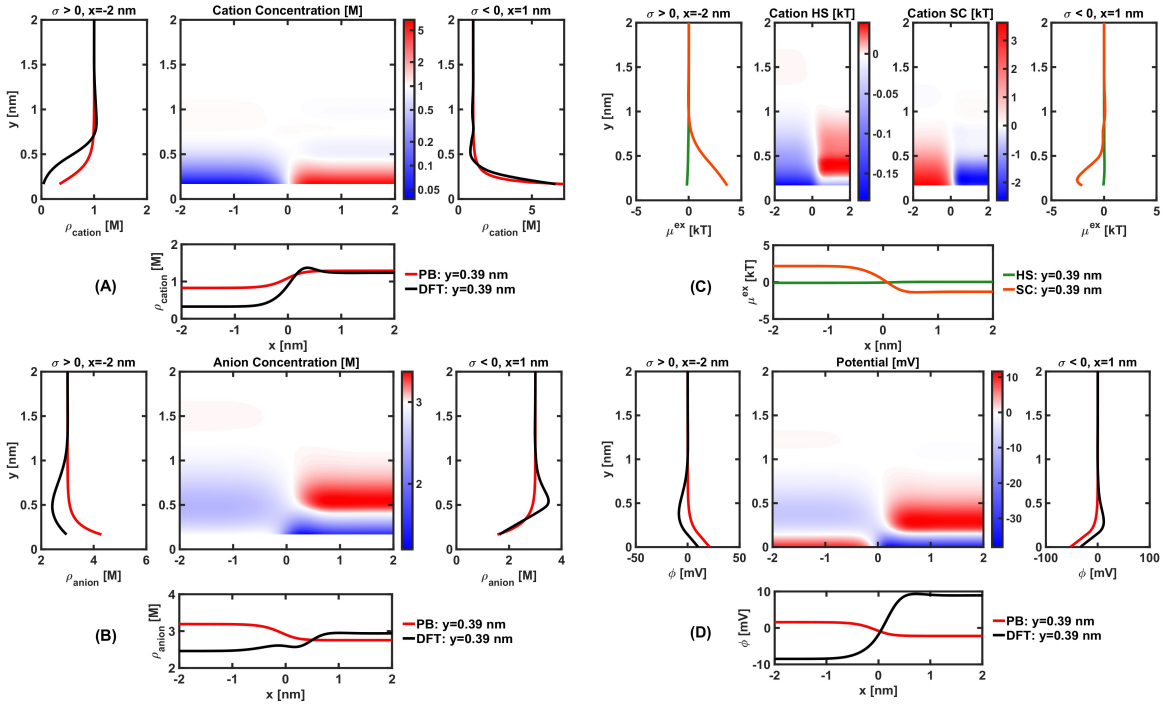

Figure 4.7: Case of the 0.3 nm trivalent at 1 M with plots from DFT of (A) cation concentration, (B) anion concentration, (C) cation HS and SC potential, and (D) mean-field electrostatic potential. See the caption of Figure 4.3 for more details.

cated absolute excess adsorption in the lateral direction:

$$\Theta_{\text{lat}} = \max_j \left(\int_{-W}^{\alpha_-} |\rho_+(x, y_j) - \rho_+(-W, y_j)|\, dx + \int_{\alpha_+}^{W} |\rho_+(x, y_j) - \rho_+(W, y_j)|\, dx \right), \quad (4.15)$$

where ρ_+ is the spatially-varying cation concentration and y_j are the y grid points. The integration limits, α_- and α_+, are used to truncate the data to remove the monotonic region near $x = 0$ (thus only accounting for troughs and crests in cation concentration):

$$\alpha_- = \max \left\{ x_k < 0 : \left[\text{sign}(\rho_+(0^-)) \left(\rho_+(x_k, y_j) - \rho_+(-W, y_j) \right) < 0 \right] \right\}, \quad (4.16)$$

$$\alpha_+ = \min \left\{ x_k > 0 : \left[\text{sign}(\rho_+(0^+)) \left(\rho_+(x_k, y_j) - \rho_+(+W, y_j) \right) < 0 \right] \right\}. \quad (4.17)$$

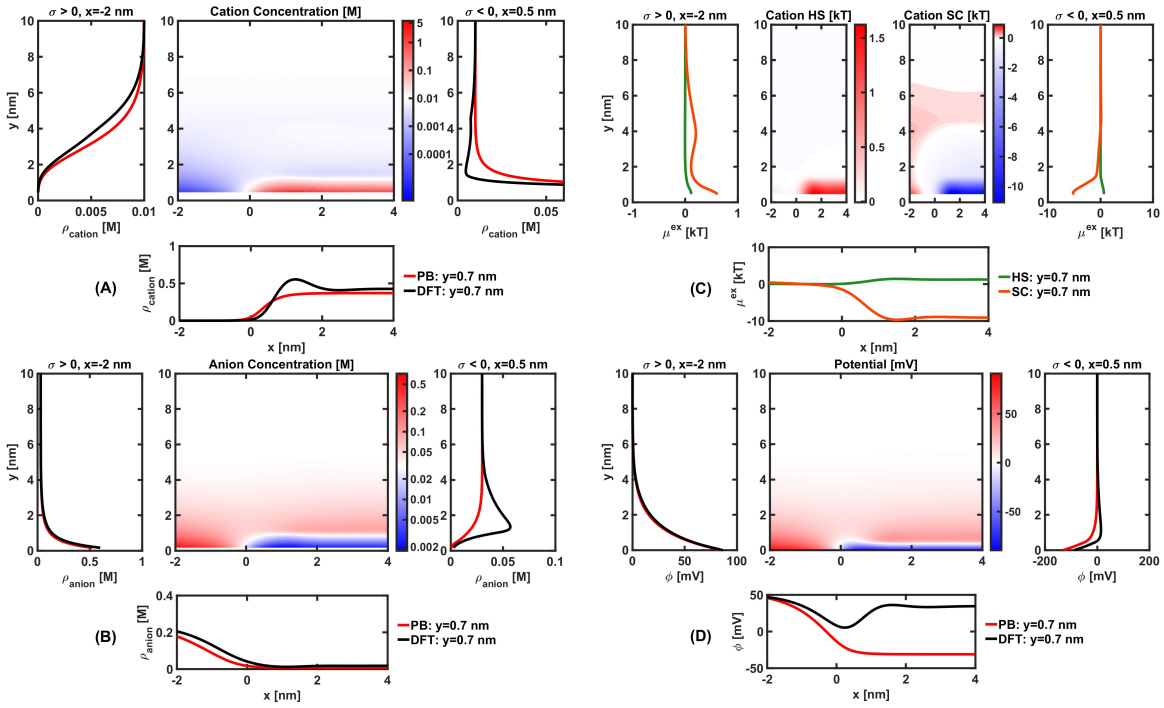

Figure 4.8: Case of the 0.9 nm trivalent at 10 mM with plots from DFT of (A) cation concentration, (B) anion concentration, (C) cation HS and SC potential, and (D) mean-field electrostatic potential. See the caption of Figure 4.3 for more details.

The Θ_{lat} integral is analogous to the excess ion adsorption in the normal direction,

$$\int_{R_i}^{H} \left(\rho(y) - \rho_i^{\text{bath}}\right) dy, \tag{4.18}$$

where ρ^{bath} is the ion concentration in the bath far from the wall. This excess adsorption is one way of quantifying the number of ions near a charged surface. However, by taking the absolute value of the integrands in Equation 4.15, the oscillation troughs below $\rho_+(\pm W, y_j)$ increase the adsorption metric, not decrease it. Furthermore, by eliminating the monotonic region, we only focus on the oscillations (non-monotonic nano-structure), and $\Theta_{\text{lat}} = 0$ for all PB profiles. Figure 9 plots Θ_{lat} for DFT for varying cation diameter, valence, concentration, and σ_2 (with $\sigma_1 = +0.05$ C/m^2).

Although Figures 3-8 show major qualitative differences between PB and DFT in the elec-

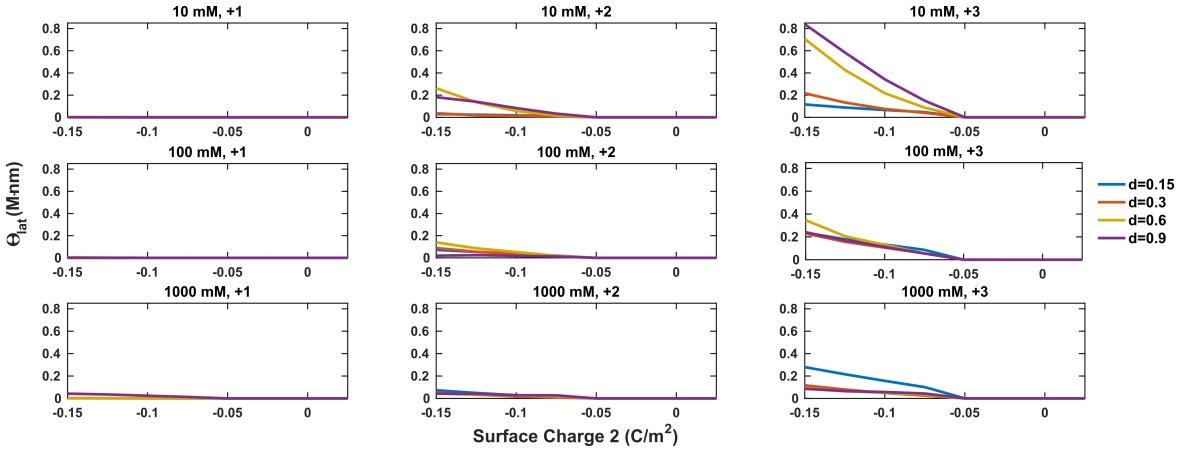

Figure 4.9: Effect of surface charge (along each x-axis), ion concentration (10 mM in the top row, 100 mM in the middle row, and 1 M in the bottom row), diameter (different colored lines), and valence (columns) on the truncated absolute excess adsorption (Θ_{lat}) defined in Equation 4.15. In all cases $\sigma_1 = +0.05$ C/m^2. Notably, a surface charge threshold near -0.05 C/m^2 exists, below which negligible lateral structure appears, although the spacing of 0.025 C/m^2 may obscure finer trends.

trostatic potential as well as the EDL normal and lateral structure, understanding the differences quantitatively over the entire range gives insight as to which cases merit further study and how PB profiles are different from DFT profiles. Here, we use Θ_{lat} as a metric to illustrate the configurations for which the lateral DFT profiles exhibit appreciable cation concentration oscillations. We focus in particular on the lateral structure, but we note that certain cases like the large monovalent cation at 1 M in Figure 4 can have considerable normal-to-the-wall structure with negligible lateral structure. Conditions under which normal-to-the-wall structure exists are described in detail in Reference 26 and so we do not discuss them further.

Figure 9 shows that, as one might expect, more negative σ_2 increases structure. (In fact, there appears to be a threshold near -0.05 C/m^2.) This is because a more negative σ_2 will increase the cation excess on the right (Figure 1), as compared to the cation depletion on the right caused by the positive σ_1. While this is similar to the normal-to-the-wall EDL structure, there are a number of notable differences between the normal and lateral EDLs. For example, charge inversion and concentration oscillations for large monovalent species are not seen in

our lateral EDLs. Also, lateral EDLs exhibit the most structure at low density (especially the trivalent species), the opposite of what is seen in EDLs perpendicular to the wall. This is due to a larger screening component in the chemical potential, μ_+^{SC}, at low concentrations that, in the absence of significant hard-sphere effects, recruits more cations to this region, creating a steeper transition and cation (as well as anion) oscillations.

Overall, the Θ_{lat} highlights conditions that may be of interest and is convenient for predicting configurations for which lateral structure might arise (normal-to-the-wall structure has already been reviewed [152]), as well as regimes in which PB no longer accurately models the system (such as large or multivalent counterions at higher magnitude surface charge).

4.3.2 Transition Width

Determining the lateral transition width is another way to quantify our results. Qualitatively, the width is the lateral distance on either side of the interface at which the normal ion profiles recover to the far away profiles at $x = \pm W$. Quantitatively, this width is calculated by first finding the largest magnitude x_k discrete lateral grid points (for both $x < 0$, x_-, and $x > 0$, x_+) at which the normalized ion density profile of species i reach 1%:

$$x_- = \max\left\{x_k < 0 : \forall_{i,j} \left|\frac{\rho_i(x_k, y_j)}{\rho_i(-W, y_j)} - 1\right| < 0.01\right\}, \tag{4.19}$$

$$x_+ = \min\left\{x_k > 0 : \forall_{i,j} \left|\frac{\rho_i(x_k, y_j)}{\rho_i(+W, y_j)} - 1\right| < 0.01\right\}, \tag{4.20}$$

for each normal coordinate y_j. The full width is then defined as the sum of the two components,

$$\Lambda_{\text{lat}} = \left(|x_-| + |x_+|\right). \tag{4.21}$$

Although the presence of significant lateral structure creates relatively wider transitions,

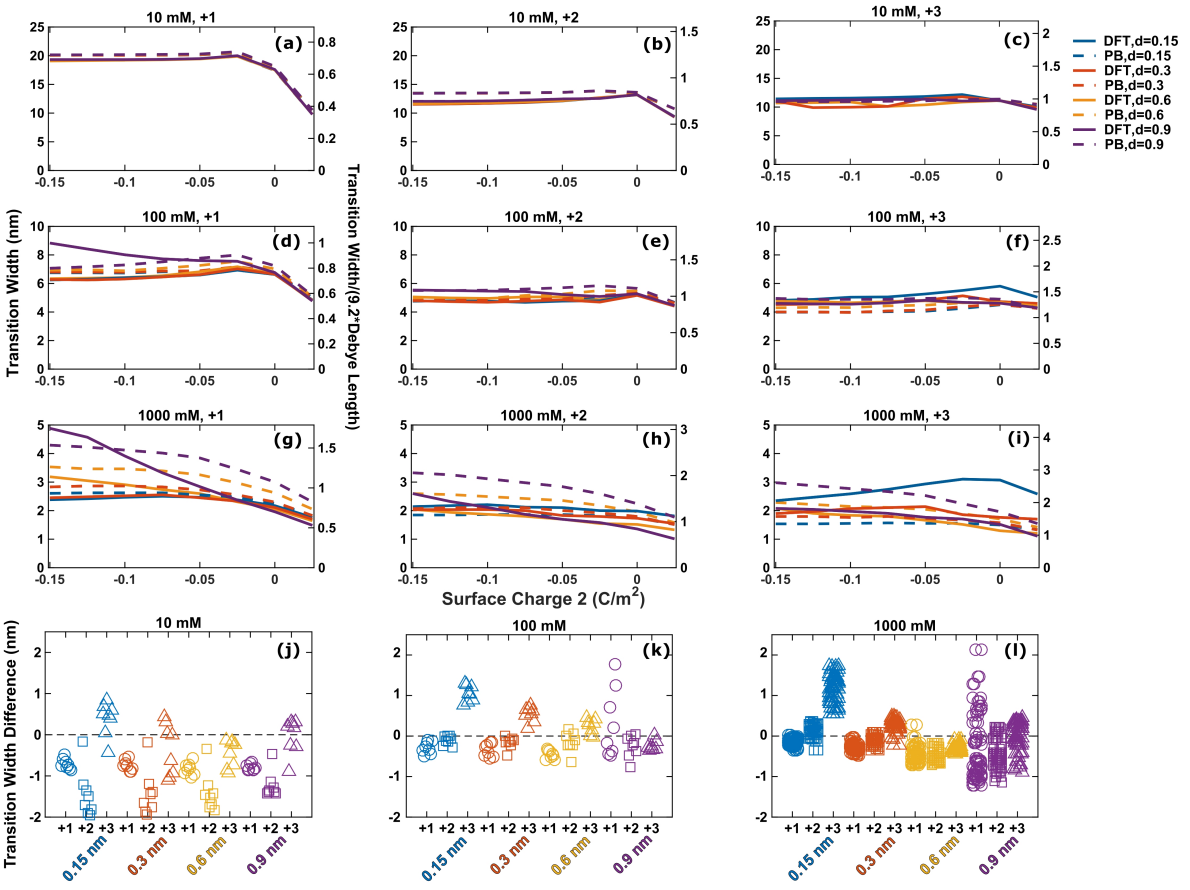

Figure 4.10: (a-i) Effect of surface charge (along each x-axis), ion concentration (10 mM in the top row, 100 mM in the middle row, and 1 M in the bottom row), diameter (different colored curves), and valence (+1 in the first column, +2 in the second, and +3 in the third) on the transition width (left y-axis) and scaled transition width (right y-axis) for DFT (solid lines) and PB (dashed lines), where in all cases $\sigma_1 = +0.05$ C/m^2. Generally, an exponential function (i.e., $f(x) = \exp(-x/\lambda)$) will decay to 0.01 within 4.6λ. Therefore, the transition width is scaled by twice this value to account for the decay on either side of the interface. (j-l) Difference in transition width between DFT and PB versus cation species for (left) 10 mM, (middle) 100 mM, and (right) 1 M concentrations. All points correspond to points in Figure 4.10, and the 1 M data also includes all combinations of two surface charge values from Table 4.1. From an ion-scale perspective, the differences between DFT and PB are a few ion diameters, and, for certain species, such as the small trivalent and large monovalent, a considerable difference is present. Generally, the difference increases for increasing valence and decreasing cation diameter.

we note that the transition width scales roughly with the Debye length,

$$\lambda_{\mathrm{D}} = \left(\frac{\epsilon_r \epsilon_0 kT}{e_0^2 \sum_{i=1}^{\nu} z_i^2 \rho_i^{\mathrm{bath}}} \right)^{1/2}. \tag{4.22}$$

As shown by the right axes of Figure 4.10, after scaling, all curves are near unity, meaning that the thicker the double layer, the larger the transition width. Practically speaking, knowing this relative scale of the transition width (between 2 and 20 nm) gives an invaluable metric of the distance from the heterogeneity at which the lateral profiles cease to vary. Along these lines, understanding the degree to which structure changes the predicted width enables superior device characterization and model utility. Similarly, awareness of the situations in which PB conflicts with DFT is crucial to determining when a more accurate theory must be applied.

Figure 4.10 shows the transition width for DFT as a function of σ_2 where $\sigma_1 = +0.05$ C/m^2. Interestingly, in most cases, each concentration and valence pair yields a relatively similar transition width. The width varies only slightly for each ion size and across surface charges, contrasting with the trends in Figure 4.9. However, the relatively large width of the 100 mM and 1 M 0.9 nm ion cases can be attributed to the development of lateral structure that is not present for the smaller monovalent diameters, as was shown in Figures 4.3 and 4.4. Likewise, while most trivalent species at 1 M exhibit structure (and thus wider transitions, shown in Figures 4.7 and 4.8), the small trivalent at 1 M shows even more structure (Figure 4.2), thus creating a relatively wider transition.

Figure 4.10 directly compares DFT and PB transition widths. Specifically, we show the difference in transition widths between DFT and PB for the different cation species. DFT and PB deviate by less than 0.5 nm for most conditions, implying that PB can adequately predict the transition width on the micro- and mesoscale, although the ion-diameter-scale profiles will not be the same. However, conditions that produce substantial lateral structure (e.g., the 1 M small trivalent and large monovalent) differ by several cation diameters and show a widely scattered arrangement. Therefore, these situations show substantial divergence in transition width between DFT and PB.

4.4 Conclusions

DFT is a valuable tool to investigate both normal and lateral structure. Using DFT, we found substantial structure perpendicular to the wall (ion concentration oscillations and charge inversion), as well as oscillations parallel to the wall in the ion concentration and electrostatic potential profiles, particularly for large and high-valence cations. The deviation in potential with respect to PB is important because the potential determines the fluid flow profile [44] [45] [53]. Specifically, the charge inversion predicted using DFT will create strikingly dissimilar fluid velocity profiles by inducing flow reversal, with practical nanofluidic implications [90]. As shown in Figures 4.3-4.8, this charge inversion and resulting flow reversal, are functions of cation species, as well as surface charge [139]. Therefore, in real systems with many ionic species and heterogeneous surface charge, a complete understanding of the complex and structured 2D transition beyond small monovalent cations necessitates an accurate, efficient theory such as DFT.

Lateral structure can be potentially exploited to perform novel electrochemical ion manipulation. For example, charged species could be manipulated near the interface by tuning surface charges and background electrolyte species. By adding external, lateral electric fields (such as those found in electrokinetics), or even time-varying surface charges (such as with an electrode), the EDL structure will vary spatiotemporally, possibly enabling fine manipulations in the potential and fluid flow. Future work will examine the complex fluid flow at this interface and the behavior of charge species near this heterogeneity.

We would like to thank Prof. Desző Boda (University of Pannonia) for providing us with MC simulation data referred to in the caption of Figure 4.2.

Chapter 5

Fluid Flow in Heterogeneous Nanochannels

In this chapter, I present two studies. First, I present a combined theoretical and experimental study (with experiments performed by Kuang-Hua (Xavier) Chou) in which trivalent species induce charge inversion and flow reversal. Second, I highlight simulations performed to interrogate fluid flow in the region very near to the transition between one surface charge to the next. These calculations are a natural continuation of the Density Functional Theory (DFT) investigation of Chapter 4 since the ion concentration and electrostatic potential are calculate from DFT, after which COMSOL (COMSOL, Inc.) is used to solve for the fluid and sample transport, specifically for complex EDLs. Furthermore, I show that it is possible to avoid performing time-intensive 2D DFT calculations, and instead calculate the 1D profiles for different surface charges and employ a smoothing average to approximate the 2D solution.

5.1 Current Monitoring with Charge-Inverting $LaCl_3$

This investigation utilizes a synergistic approach to combine experiments and theory. We use custom-fabricated nanochannels to probe charge-inverting (and flow reversal inducing) salt species. Specifically, we exploit charge-inverting $LaCl_3$ in order to probe the EDL structure via modified the traditional current monitoring experiments. Nanochannel current and flow rate are measured, allowing for a direct comparison with theory. In order to enhance current theory, experimental results can help fine-tune free variables such as location of the slip plane. Furthermore, theory can be used to better understand experiments, and theory can be updated based on experimental results for use as a predictive tool. We perform experiments in homogeneous straight nanochannels, although moving forward we will also vary the surface potential via an embedded electrode (shown in Figure 5.1).

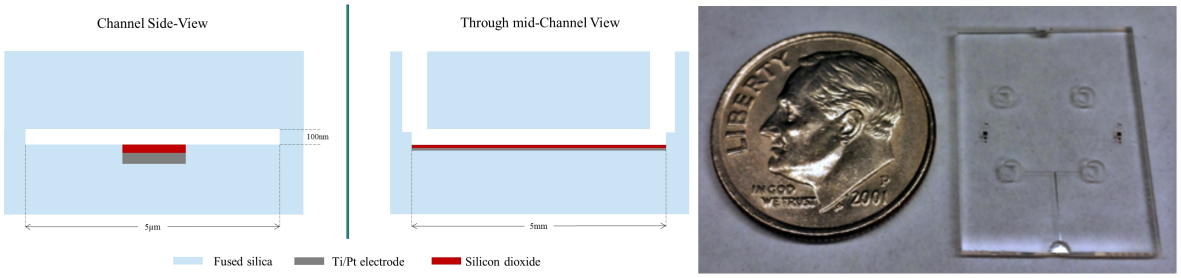

Figure 5.1: An embedded, insulated electrode and nanochannels are patterned and etched into the fused silica substrate using standard photolithography and dry etching techniques. The embedded electrode consists of a 15 nm Ti adhesion layer and 105 nm Pt layer insulated with sputtered silicon dioxide. After embedding the electrode, the nanochannel pattern is dry etched 100 nm into the fused silica substrate. The device is sealed by direct bonding a polished fused silica wafer to the device wafer using nitrogen oxygen surface plasma activation.

5.1.1 Theory

To determine the axial channel position ($\tilde{x}$ in Figure 5.2b), the bulk conductivity, σ_i, and zeta potential, ζ_i, of each species i must be measured. The electric field in each section is then

given by:

$$E_i = \frac{V}{L\sigma_i}\left[\frac{\tilde{x}}{L\sigma_1} + \frac{(1-\tilde{x})}{L\sigma_2}\right]^{-1}, \tag{5.1}$$

where V is the applied potential, L is the channel length, and the subscripts 1 and 2 denote the left and right sections of the channel, respectively. The electroosmotic flow component of each section is

$$u_{i,\text{EOF}} = -E_i \epsilon_r \epsilon_0 \zeta_i / \mu_w, \tag{5.2}$$

where ϵ_r and ϵ_0 are the relative and vacuum permittivity and μ_w is the viscosity of water. Using a simple mass conservation balance (similar to Section 3.4), the pressure at $\tilde{x}$ is

$$P_1 = \frac{-12\mu_w}{h^2}\frac{u_{1,\text{EOF}} - u_{2,\text{EOF}}}{\frac{1}{\tilde{x}} + \frac{1}{L-\tilde{x}}}. \tag{5.3}$$

The pressure-driven flow (PDF) component of each section is then:

$$u_{1,\text{PDF}} = \frac{P_1}{\tilde{x}}\frac{h^2}{12\mu_w} \tag{5.4}$$

$$u_{2,\text{PDF}} = -\frac{P_1}{L-\tilde{x}}\frac{h^2}{12\mu_w}, \tag{5.5}$$

meaning that the total velocity is given by:

$$u_{i,\text{tot}} = u_{i,\text{EOF}} + u_{i,\text{PDF}}, \tag{5.6}$$

where $u_{1,\text{tot}} = u_{2,\text{tot}}$. The total current is

$$I_{i,\text{tot}} = \sigma_i h w E_i, \tag{5.7}$$

where w is the channel width (and $I_{1,\text{tot}} = I_{2,\text{tot}}$).

Practically, after determining the conductivity and zeta potential of each species, $\tilde{x}$ is found by fitting to either experimental velocity or current, although both yield similar results.

5.1.2 Materials and Methods

Figure 5.1 shows a nanofluidic channels with embedded electrode. The key features of our fabrication process is the ability to build planarized nanochannels with embedded electrodes, as well as an optimized room temperature bonding process (Figure 5.1). Specifically, we optimize a two-step plasma activation process which involves an oxygen plasma treatment followed by a nitrogen plasma treatment to increase the fusion bonding strength of fused silica. Our channels do not leak with over 1 MPa of applied pressure after a 24 hour storage time, and the electrode exhibits capacitive behavior with a finite parallel resistance in the upper $\text{M}\Omega$ range for up to a 6.3 Vdc bias.

5.1.3 Experimental Results

We performed modified current monitoring experiments with Tris-EDTA buffer (TE buffer, pH 7) and $LaCl_3$ (also Tris-buffered). Specifically, we loaded the channel with Tris buffer, and replaced the positive well with $LaCl_3$+Tris (this displaced the initial Tris as the solution moves from the positive well to the negative). However, as the channel fills, the $LaCl_3$+Tris flows toward the positive well because of charge inversion.

Using our theoretical analysis, I matched the experimental current and electroosmotic velocity (shown in Figure 5.2) to calculated values, thereby determining the theoretical front position based a simple mass/current conservation balance. The zeta potential for each species is determined from traditional current monitoring experiments, after which $\tilde{x}$ is varied iteratively to best match $I_{\text{tot},j}$ at each point, j, (giving $\tilde{x}_j$ for each point), as well as the mean

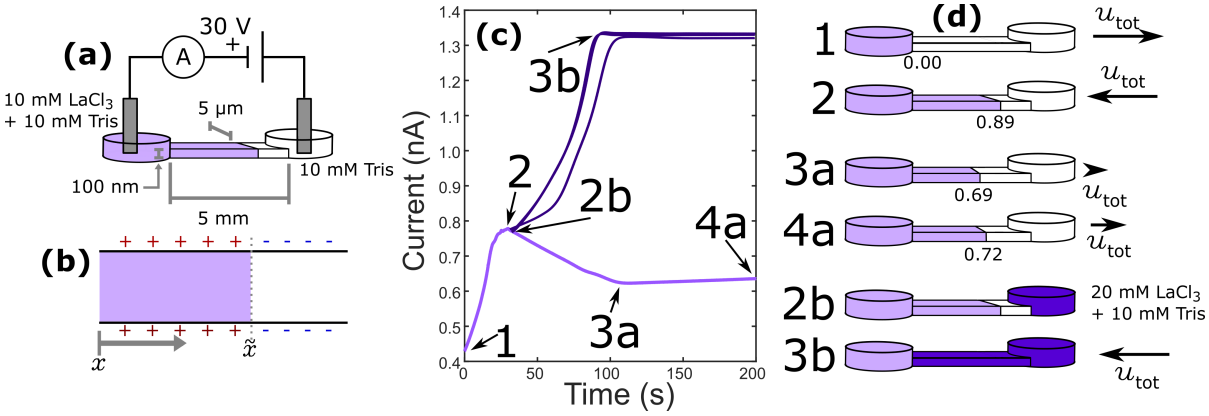

Figure 5.2: This composite figure shows the (a-b) experimental setup and nanochannel solution composition, (c) current versus time for two experiments, and (d) the solution displacement make-up of the different points in (c). In (d), the number under each image is the value of $\tilde{x}$ for that point. Point 1 corresponds to the initial setup with Tris buffer in the channel, and $LaCl_3$+Tris in the positive well. Point 2 shows the $LaCl_3$+Tris partially entering the channel. However, because the La^{3+} induces a sign reversal in the electrostatic wall potential, the solution retreats (from Point 2 to Point 3a). The solutions then reach near-steady-state (with minor creep) from Point 3a to 4a. The values below (d) on the channel indicate the front position. If, however, a higher solution $LaCl_3$+Tris solution is added to the negative reservoir at Point 2b, then both solutions will move to the left, allowing us to extract zeta potential and other key electrokinetic values (shown as multiple trials from Point 2b to 3b).

velocity between each point (mid-point between j and $j+1$ is denoted by $(j+1)/2$:

$$u_{\text{tot},(j+1)/2} = \frac{\tilde{x}_{j+1} - \tilde{x}_j}{t_{j+1} - t_j}. \tag{5.8}$$

Point j	Time (s)	$\tilde{x}/L$	Exp. I_{tot} (nA)	Calc. I_{tot} (nA)	Exp. $u_{\text{tot},(j+1)/2}$ (μm/s)	Calc. $u_{\text{tot},(j+1)/2}$ (μm/s)
1	0	0	0.460	0.459	146	166
2	30	0.89	1.16	1.110	−13.0	−13.1
3a	109	0.69	0.846	0.845	1.65	60.3
4a	200	0.72	0.871	0.877	N/A	N/A

Table 5.1: Current and velocity values from predicted $\tilde{x}$ position at each point in Figure 5.2

Table 5.1 shows the calculated $\tilde{x}$ positions necessary to match the measured and calculated current and velocity values. As illustrated, theory predicts the experimental values quite well (especially the current values). The simple elegance of this method is its true utility, complex

theories are not necessary as the method requires no fit parameters. The front position, $\tilde{x}$, is determined by equally weighting the current and velocity and matching the calculated and experimental values. Because of this methodology, the current values match excellently, while the velocity matches well for the most part. The discrepancy between the experimentally observed and calculated velocity for Point 3a results from longer time-scale effects present (and perhaps ion adsorption and interaction with the surface that alters the zeta potential on longer time-scales).

5.1.4 Conclusions

We successfully monitored the change in current with time for the case of a flow-reversal-inducing trivalent species displacing a buffer solution. We then showed that key inflection points in the current versus time are well-predicted using a simple mass conservation analysis. These preliminary results demonstrate the validity of our setup, and we will continue with more experiments for which the $LaCl_3$ concentration as well as the channel surface charge vary. This complete set will enable greater characterization of the electric double layer and possibly exploitation for novel applications such as in Section 3.4.

5.1.5 Future Work

While Figure 5.2 highlights one case of current monitoring with complex electrolytes, we will pursue a wider set of experiments with $LaCl_3$+Tris, varying $LaCl_3$ concentration as well as surface charge. Similar to van der Heyden et al [84] we will vary the concentration (from as low as 10 μM up to 100 mM) in order to determine the threshold concentration that induces charge inversion. For low concentrations, we expect that La^{3+} does not cause charge inversion; however, as the concentration increases, charge inversion will occur. Moreso, determining this concentration gives allows for feedback into the DFT model, which can be improved

based on empirical data (similar to Hoffman and Gillespie [139]. Additionally, exploiting our newly fabricated nanochannels with embedded electrodes, we will tune the surface charge to determine the effect of surface charge on charge inversion (and flow reversal) as well as channel conductivity. Ultimately, this method will enable changes in the current versus time profile to be directly correlated to changes in zeta potential and front position, $\tilde{x}$.

5.2 Two-Dimensional Fluid Flow with Heterogeneous Surface Charge

The complex fluid flow at a heterogeneous interface is calculated from the ion concentration and electrostatic potential results from DFT and PB using Ohm's Law and Stokes flow equations. This study is a continuation of the initial EDL structure investigation in Section 4, and, currently, COMSOL Multiphysics is used to calculate the flow field, which is the first, to my knowledge, integration of classical DFT into COMSOL. Exploiting COMSOL's immense computational toolbox, complex time-dependent studies are easily achieved, meaning time-dependent sample species transport can be simulated. This combination of DFT and nanofluidic experiments with embedded electrodes allows, for the first time, a true probe of the EDL, which can in turn lead to breakthroughs for complex nanofluidic electrokinetic systems.

To illustrate the complex flow possible at a heterogeneous surface, as well as to compare PB and DFT results, Figure 5.3 presents one example showing 2D electrostatic potential and fluid flow for a small trivalent cation. The electrostatic potential exhibits significant normal-to-the-wall (in the y direction) and lateral (x direction) non-monotonicity. Interestingly, the normal potential profile changes sign, resulting in fluid flow reversal near the wall. This complex interplay is of much interest with potential applications in charged species manipulation near the interface.

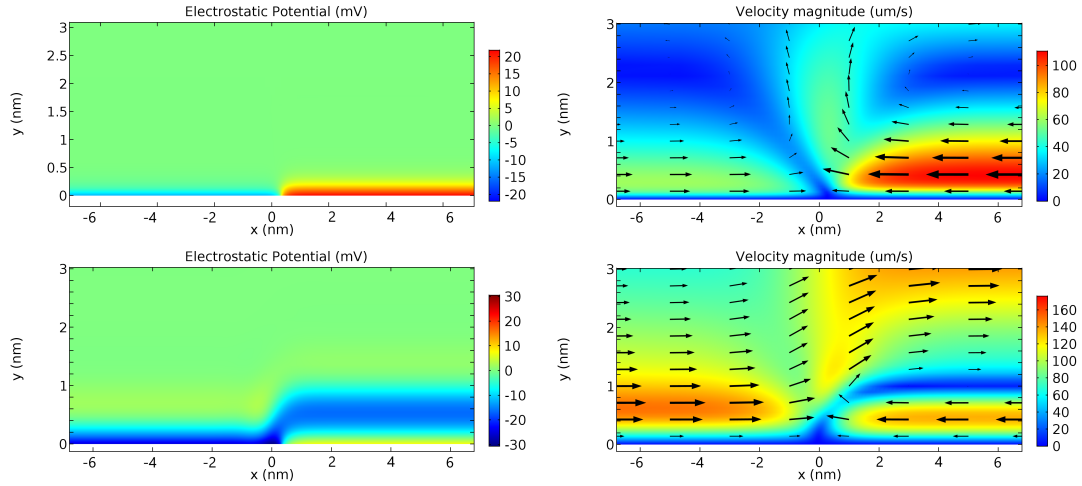

Figure 5.3: (left column) Electrostatic potential and (right column) velocity profile for (top row) PB and (bottom row) DFT for a 0.15 nm diameter trivalent cation (similar to La^{3+}) at 1 M concentration and 0.3 nm monovalent anion for surface charges of ± 0.05 C/m^2 for $\pm x$, respectively.

The only true fitting parameter necessary to match experiments and simulations is the Stern layer height, H_s, or the extent of the immobile region of ions at a charged surface. The size of H_s remains an ongoing topic of interest because it has a significant effect on the fluid flow and current observed. By varying H_s, fluid flow reversal can actually be induced or eliminated for charge-inverting conditions [35]. I modeled a nanochannel with an axial electrode on the top and bottom surfaces, covering the middle (axial) third of the channel. Figure 5.4 shows the effect of varying Stern layer height on the flow rate for varying cation diameter, valence, and concentration for surface charges of $\pm$ 0.05 C/m^2. After experimental measurements are taken, the Stern Layer height is varied in conjunction with DFT calculations, to best match theory and experiments.

As mentioned, certain conditions will exhibit completely different flow rates (even switching from positive to negative) based on the location of the Stern layer. For example, the 0.9 nm cation often induces charge inversion, meaning that the transverse electrostatic potential changes sign instead of decay monotonically to zero. This change in sign is illustrated for a few cases in Section 4, and generally manifests as a slight bump in potential within a cou-

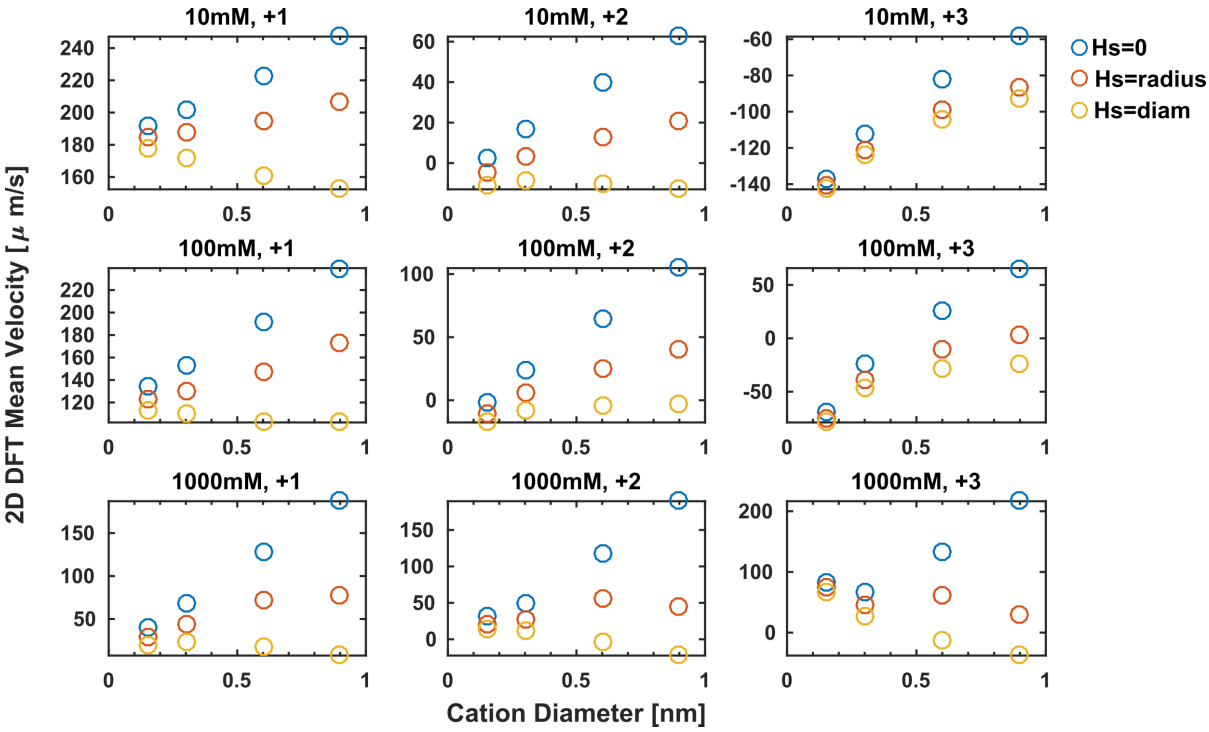

Figure 5.4: Effect of varying Stern layer height, H_s, on mean flow rate for a 10 nm nanochannel with an embedded electrode. A parametric study of cation species was used to illuminate the full effect under different conditions. 3 Stern Layer heights are explored: equal to zero, equal to the ion radius, and equal to the ion diameter. Because the Stern Layer height has such a significant effect on apparent flow rate and even direction, it is instrumental as a fitting parameter.

ple nanometers of the wall. Flow reversal is induced if the Stern layer height overlaps this bump region. Performing experiments and fitting the Stern layer height to match theory and experiments allows us to even better understand the EDL structure.

We explore a parameter set similar to that of Section 4, for which I modeled a nanochannel with an axial electrode on the top and bottom surfaces, covering the middle (axial) third of the channel. While 2D simulations can elucidate nano-scale fluid flow, it would be preferable to simulate a full channel geometry without having to perform 2D DFT calculations. For example, 1D solutions for concentration and potential can be combined into a quasi 2D solution by stacking the 1D solutions and performing a moving average smoothing filter in the lateral dimension, with window size equal to the Debye length. The resulting smoothed concentra-

tion and potential yield a fluid flow profile remarkably similar to the full 2D solution for thin EDLs (data not shown). Even for configurations in which the transition width to channel length ratio is 10%, the apparent zeta potential difference is at most 4 mV, which is practically negligible. The observed conductivity differences are similarly within the experimental error. Moreover, the 2D full and smoothed solutions converge to the same values for higher channel length to transition width ratio, thus highlighting the effect of decreasing transition importance regarding the overall flow. Furthermore, the 1D solution can be calculated in a matter of seconds, while the 2D solution takes tens of minutes.

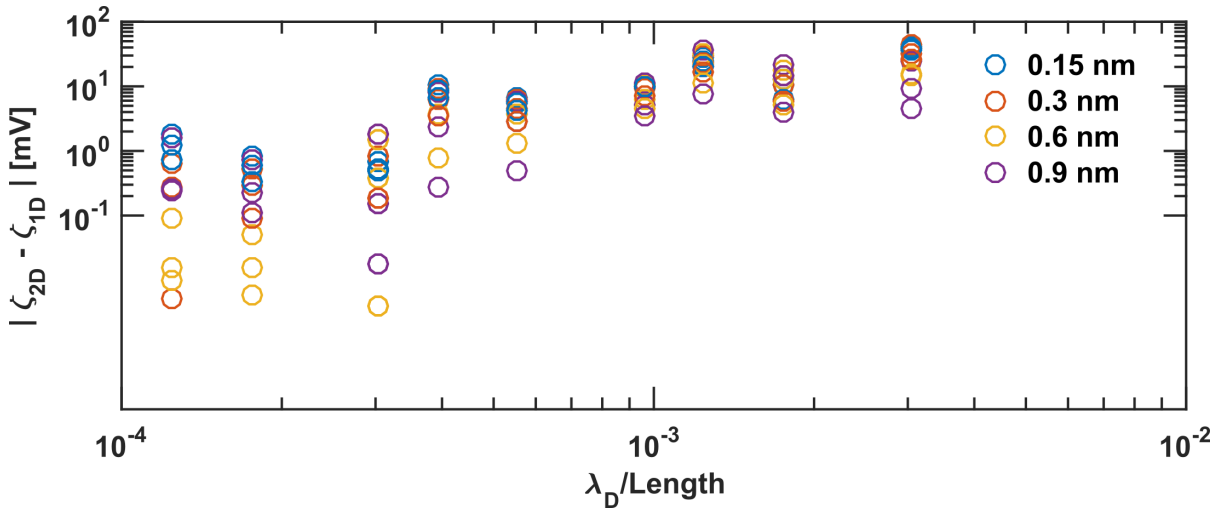

Figure 5.5: (top) Absolute zeta potential difference between 1D and 2D solutions relative to the Debye length to channel length (equal to 1 μm) ratio, and (bottom) absolute conductivity difference between 1D and 2D solutions for a channel height of 10 nm. Four ion diameters at three concentrations ($10, 100,$ and 1000 mM) for surface charges of $\pm$ 0.05 mC/m^2. As the Debye length (and hence transition width) take up more of the channel length, the 1D approximation breaks down as illustrated in terms of zeta potential and channel conductivity.

To further simplify the solution method, the full 2D solution is compared with a true 1D approximation (assuming no transition width). Figure 5.5 illustrates the differences in zeta potential and conductivity relative to the Debye length to channel length ratio between full 2D solutions and the true 1D. As the size of the Debye length becomes significant relative to the channel length (even as little as 1%, corresponding to λ_D/Length of 10^{-3}), the 1D

approximation no longer suffices for any configuration since a zeta potential difference is near or above 10 mV. Below $3 \cdot 10^{-4}$ ($\lambda_D/h = 0.3\%$), though, the zeta potential difference is below 2 and would be practically undetectable.

Moreover, a 1D approximation would enable a quick wide-sweeping parametric study with which corresponding experiments can be used to determine fitting variables such as Stern layer height. Moving forward, we will perform additional experiments with charge-inverting $LaCl_3$ for varying concentration and surface charge in our newly-fabricated nanochannels with embedded electrodes. This will enable a true probe of the electric double layer structure.

Chapter 6

Conclusions and Future Work

6.1 Conclusions

The work I performed for my thesis builds on the wealth of knowledge and achievements in the field of electrokinetics, and I hope that my work can further propel the field toward uncovering groundbreaking phenomena and innovative applications.

The model developed in Chapter 2 allows experimentalists to predict nanochannel behavior better in order extract parameters of interest, such as zeta potential, with greater ease and accuracy, as well as to predict regimes in which dispersion may be significant. This coupling between modeling and experiments motivated further projects. This model, with minor alterations, shows great potential for modeling other configurations such as our recent nanochannel concentration enhancement method with inhomogeneous surface charge, as well as the ongoing project involving fluid flow with complex geometry and ion species.

Chapter 3 covers 3 projects for which I used theory to assist experimentalists in elucidating experimental results. First, we showed that DNA-induced changes in surface charge can be detected in nanochannels, although the nanochannels actually detect any DNA, making them a bit too sensitive. Moving forward with a similar project, Alveo Technologies

in Alameda, CA is developing a DNA sensor that senses changes in ionic composition (and therefore conductivity) when DNA replication takes place. Second, I modeled the convective-diffusion-reaction equation to aid in the understanding of DNA hybridization kinetics under non-equilibrium conditions in micro- and nanochannels. We recently showed that increasing confinement (such as in nanochannels smaller than 100 nm), decreasing the dissociation constant, thus broadening our understanding of evolutionary biology, and the role of confinement in DNA replication and protein synthesis. Last, I modeled and performed experiments to interpret experimentally-observed isotachophoretic-like conditions in nanochannels with complex, charge inversion-inducing species. We follow this study with a similar investigation of charge-inverting species in the presence of an addressable, embedded electrode that enables tuning of the surface potential to better interrogate the EDL.

Chapter 4 presents a systematic study (via Density Functional Theory calculations), showing that varying cation diameter, valence, and concentration as well as surface charges can induce significant lateral (parallel to the wall) EDL structure. Continuing this work, Chapter 5 highlights simulation results of the fluid flow in a heterogeneous surface charge nanochannel with complex ionic species and high surface charge. These results will be used predictively to highlight potential experimental conditions that are worth exploring. Moving forward, we will explore heterogeneous nanochannels experimentally. The experimental results will enable feed-back to theory, thus allowing for fine-tuning and improving of theory, after which theory can be further employed to probe as-yet experimentally impossible regimes.

6.2 Future Work

In electrokinetic micro- and nanofluidic systems, electrolyte interaction with charged surfaces is not entirely understood, meaning that, while experiments have proven quite instrumental in leading to real applications, a complete predictive theory still has yet to be devel-

oped. Indeed, Poisson-Boltzmann (PB) based theories adequately predict ion concentration and electrostatic potential for small ions and dilute systems, but as systems become more complex and confined, the finite size of the ions and near-field screening effects become more significant, necessitating a more complete theoretical approach. Future work includes using a variety of tools to investigate structured electric double layers (EDLs) and atypical electro-osmotic flow (EOF) resulting from complex ions and surface charge heterogeneity in micro- and nano-scale fluidic systems to better understand electrochemical phenomena, contributing to the development of more effective desalination and energy technology systems. A synergistic approach can be employed, combining theory and experiments to systematically explore and develop theories concerning the EDL and EOF to enhance our understanding of the ion-ion and ion-wall interactions in the EDL, as well as aid in the development of novel future applications. This will require both computational/numerical knowledge regarding nano-scale electrochemical systems, as well as an understanding of experimental systems and how to relate experiments to appropriate theories.

6.2.1 Objectives

Building on the established wealth of knowledge in modeling the EDL, it naturally follows to study well-defined fluidic systems with micro- and nano-scale geometries possessing both complex ions and heterogeneous surface charges. Therefore, it is imperative to probe as-yet misunderstood experimental results related to electrolyte transport in nanofluidic systems. *Specifically, a study of merit would explore asymmetric, multivalent ionic species and large surface charge systems, typical to applications such as desalination and electrochemical energy systems, pushing both the experimental and theoretical limits in order to discover unique nano-scale phenomena.*

1. Both experimentally and theoretically, employ density functional theory (DFT) to probe

a wide variety of surface charges in variable nano-scale geometries with different ion species (ion diameter, valence, and concentration) to predict ionic current and EOF. The 2D system will be modeled with DFT [38] [7], investigating large surface charges since the addressable electrodes allow for this freedom, and DFT is particularly well-suited for high surface charge regimes [36].

2. Use experimental results from such systems to fine-tune theory, and use updated theory as a predictive tool for future experimental areas of study. By dissecting experimental data, a more accurate theory can be developed to specifically address issues such as Stern layer height, species mobility, and unforeseen chemical reactions.

3. Apply resulting knowledge to nano-scale ion transport for applications in desalination or energy technology. Specifically, carbon materials such as nanotubes, graphene, and porous electrodes are well-suited for DFT modeling, holding great promise for applications in desalination and energy technology systems. Exploiting DFT to fundamentally understand such materials and the interaction with the EDL is essential for the development of real products and commercializable technologies.

6.2.2 Technical Approach and Expected Results

To achieve the proposed objectives, one must employ a synergistic approach, combining experiments and theory in the following manner:

1. First, one must study ultra-confined nanofluidic systems (< 10 nm) with variable but well-defined heterogeneity in surface charges over a wide parametric ion range to better understand multi-component electrolyte transport. Because we can model random configurations of patterned surface charges (preserving minimum experimental patch sizes of 10 nm), I propose to test as many configurations as possible in search of at least one

configuration that will allow for novel applications such as many-fold charged species concentration enhancement or selective transport through the channel. Specifically, confined channels (< 10 nm) with electrodes of variable size (as small as 10 nm and up to half the full channel length) and spacing (same values as electrode size) can be tested numerically via randomized patterning. Inputs will be voltage, pressure, geometry, and ion species (i.e., diameter, valence, and concentration). Results will include the channel conductivity, zeta potential, and EDL capacitance. From these results, theory is calibrated against well-designed and fabricated experimental microchannels and nanochannels with and without embedded electrodes. These systematic experiments, with diameter ranges of 0.15 to 1 nm, valences up to +3, and concentrations from 1 μM to 1 M have the potential to uncover novel transport, separation, and concentration mechanisms similar to that found in our recent work (submitted), where thick EDLs cause a concentration enhancement mechanism never before explored in such a systematic manner. Regardless, a complete understanding of effect of ion diameter and charge would immensely benefit the field, especially regarding fluid transport (i.e., wall slip), as well as EDL capacitance and ion selectivity.

2. Once calibrated, this theory is employed to explain interesting experimental results and as a predictive tool for potential innovative nanofluidic systems. For example, as our theory was able to predict the combined concentration and charge inversion mechanism involved $Ru(bpy)_3Cl_2$ and $MgCl_2$, we can similarly exploit the theory to understand novel phenomena that arises from experiments. Specifically, one can exploit the new theories to combine DFT charge inversion with time-dependent phenomena such as field-amplified sample stacking [48], isotachophoresis [50], or ion concentration polarization [51] to predict novel focussing, separation, and/or pre-concentration mechanisms. Moreso, experiments will drive updated DFT model development, after which

new theory is exploited and used predictively for potential experiments.

3. Finally, one should model complex nonuniform geometries (i.e., porous media) or ill-defined systems (like matrices of carbon nanotubes or other nano-scale energy conversion devices). Many potential systems exist (such as carbon nanotubes and graphene based systems) with great potential for innovative research and applications. This predictive model will motivate further experiments of such systems by the same synergistic method as objectives 1 and 2.

By building on previous modeling and experimental results, a two year time-frame would allow for a complete study that addresses all 3 objectives. One year should suffice to perform the systematic experiments and run corresponding calculations. Thorough data analysis can be performed concurrently, and overall trends and future experiment planning will take another few months. Finally, exploring extreme areas of predicted significance will consume another few months, and corresponding experiments depend on both collaborators and results.

Bibliography

[1] K. G. H. Janssen, H. T. Hoang, J. Floris, J. de Vries, N. R. Tas, J. C. T. Eijkel, and T. Hankemeier, *Solution Titration by Wall Deprotonation during Capillary Filling of Silicon Oxide Nanochannels*, *Anal. Chem.* **80** (nov, 2008) 8095–8101.

[2] R. F. Probstein, *Physicochemical hydrodynamics: an introduction.* Wiley, New York, NY, 1994.

[3] A. J. Russell, J. T. Del Bonis-O'Donnell, T. M. Wynne, M. T. Napoli, and S. Pennathur, *Separation behavior of short single- and double-stranded DNA in 1 micron and 100 nm glass channels*, *Electrophoresis* **35** (feb, 2014) 412–418.

[4] T. M. Wynne, C. McCallum, J. T. Del Bonis-O'Donnell, P. Crisalli, and S. Pennathur, *Hybridization Thermodynamics of DNA Oligonucleotides during Microchip Capillary Electrophoresis*, *Analytical Chemistry* **87** (mar, 2015) 2811–2818.

[5] J. P. Valleau and G. M. Torrie, *Electrical double layers. V. Asymmetric ion-wall interactions*, *J. Chem. Phys.* **81** (dec, 1984) 6291–6295.

[6] D. Gillespie, M. Valiskó, and D. Boda, *Density functional theory of the electrical double layer: the RFD functional*, *Journal of Physics: Condensed Matter* **17** (oct, 2005) 6609–6626.

[7] R. Roth and D. Gillespie, *Shells of charge: a density functional theory for charged hard spheres*, *Journal of Physics: Condensed Matter* **28** (jun, 2016) 244006.

[8] E. Biddiss, D. Erickson, and D. Li, *Heterogeneous surface charge enhanced micromixing for electrokinetic flows.*, *Analytical Chemistry* **76** (2004), no. 11 3208–13.

[9] R. Karnik, R. Fan, M. Yue, D. Li, P. Yang, and A. Majumdar, *Electrostatic Control of Ions and Molecules in Nanofluidic Transistors*, *Nano Letters* **5** (2005), no. 5 943–948.

[10] X. Jin and N. R. Aluru, *Gated transport in nanofluidic devices*, *Microfluidics and Nanofluidics* **11** (2011), no. 3 297–306.

[11] Y. Ai, J. Liu, B. Zhang, and S. Qian, *Ionic current rectification in a conical nanofluidic field effect transistor*, *Sensors and Actuators B: Chemical* **157** (oct, 2011) 742–751.

[12] F. F. Reuss, *On a new effect of electrochemical*, *Mem. Soc. Imp. Natur. Moscow* **2**.

[13] M. Gouy, *Sur la constitution de la charge électrique à la surface d'un électrolyte*, *J. Phys. Théorique Appliquée* **9** (1910), no. 1 457–468.

[14] D. L. Chapman, *LI. A contribution to the theory of electrocapillarity*, *Philos. Mag. Ser. 6* **25** (apr, 1913) 475–481.

[15] P. Debye and E. Hückel, *On the Theory of Electrolytes. I. Freezing Point Depression and Related Phenomena*, *Phys. Zeitschrift* **24** (1923), no. 9 185–206.

[16] O. Stern, *Theory of the electrical double layer.(in german.)*, *Electrochemistry* **30** (1924) 508–516.

[17] J. Bikerman, *XXXIX. Structure and capacity of electrical double layer*, *The London, Edinburgh, and Dublin Philosophical Magazine and Journal of Science* **33** (may, 1942) 384–397.

[18] D. C. Grahame, *Diffuse Double Layer Theory for Electrolytes of Unsymmetrical Valence Types*, *J. Chem. Phys.* **21** (jun, 1953) 1054–1060.

[19] G. M. Torrie and J. P. Valleau, *A Monte Carlo Study of an Electrical Double Layer*, *Chemical Physics Letters* **65** (aug, 1979) 343–346.

[20] M. Valiskó, D. Henderson, and D. Boda, *Competition between the Effects of Asymmetries in Ion Diameters and Charges in an Electrical Double Layer Studied by Monte Carlo Simulations and Theories*, *The Journal of Physical Chemistry B* **108** (oct, 2004) 16548–16555.

[21] S. Plimpton, *Fast Parallel Algorithms for Short-Range Molecular Dynamics*, *Journal of Computational Physics* **117** (mar, 1995) 1–19.

[22] A. G. Moreira and R. R. Netz, *Computer Simulations of the Electric Double Layer*, in *Novel Methods in Soft Matter Simulations* (M. Karttunen, I. Vattulainen, and A. Lukkarinen, eds.), vol. 640, pp. 245–278. Springer Berlin Heidelberg, Berlin, feb, 2004.

[23] J. W. Lee, R. H. Nilson, J. A. Templeton, S. K. Griffiths, A. Kung, and B. M. Wong, *Comparison of Molecular Dynamics with Classical Density Functional and Poisson-Boltzmann Theories of the Electric Double Layer in Nanochannels*, *Journal of Chemical Theory and Computation* **8** (jun, 2012) 2012–2022, [arXiv:1011.1669].

[24] B. Giera, N. Henson, E. M. Kober, M. S. Shell, and T. M. Squires, *Electric Double-Layer Structure in Primitive Model Electrolytes: Comparing Molecular Dynamics with Local-Density Approximations*, *Langmuir* **31** (mar, 2015) 3553–3562.

[25] R. Evans, *The nature of the liquid-vapour interface and other topics in the statistical mechanics of non-uniform, classical fluids*, *Advances in Physics* **28** (apr, 1979) 143–200.

[26] R. Roth, R. Evans, A. Lang, and G. Kahl, *Fundamental measure theory for hard-sphere mixtures revisited: the White Bear version*, *Journal of Physics: Condensed Matter* **14** (nov, 2002) 12063–12078.

[27] W. Nonner, L. Catacuzzeno, and B. Eisenberg, *Binding and Selectivity in L-Type Calcium Channels: A Mean Spherical Approximation*, *Biophysical Journal* **79** (oct, 2000) 1976–1992.

[28] D. Gillespie, W. Nonner, and R. S. Eisenberg, *Density functional theory of charged, hard-sphere fluids*, *Physical Review E* **68** (sep, 2003) 031503.

[29] B. I. Shklovskii, *Screening of a macroion by multivalent ions: Correlation-induced inversion of charge*, *Physical Review E* **60** (nov, 1999) 5802–5811, [9907351].

[30] C. W. Outhwaite, *A modified poisson-boltzmann equation in the double layer*, *Chem. Phys. Lett.* **7** (dec, 1970) 636–638.

[31] S. Levine and C. W. Outhwaite, *Comparison of theories of the aqueous electric double layer at a charged plane interface*, *J. Chem. Soc. Faraday Trans. 2* **74** (1978) 1670.

[32] C. W. Outhwaite and L. B. Bhuiyan, *An Improved Modified Poisson-Boltzmann Equation in Electric-Double-Layer Theory*, *J. Chem. Soc., Faraday Trans. 2* **79** (1983), no. 5 707–718.

[33] M. Mandel, *The Poisson-Boltzmann Equation for Aqueous Solutions of Strong Polyelectrolytes Without Added Salt: The Cell Model Revisited*, *The Journal of Physical Chemistry* **96** (may, 1992) 3934–3942.

[34] M. Z. Bazant, B. D. Storey, and A. a. Kornyshev, *Double Layer in Ionic Liquids: Overscreening versus Crowding*, *Phys. Rev. Lett.* **106** (jan, 2011) 046102.

[35] R. H. Nilson and S. K. Griffiths, *Influence of atomistic physics on electro-osmotic flow: An analysis based on density functional theory*, *Journal of Chemical Physics* **125** (2006), no. 16 164510.

[36] D. Gillespie, *A review of steric interactions of ions: Why some theories succeed and others fail to account for ion size*, *Microfluidics and Nanofluidics* **18** (may, 2015) 717–738.

[37] R. Roth, *Fundamental measure theory for hard-sphere mixtures: a review*, *Journal of Physics: Condensed Matter* **22** (feb, 2010) 063102.

[38] Y. Rosenfeld, *Free-Energy Model for the Inhomogeneous Hard-Sphere Fluid Mixture and Density-Functional Theory of Freezing*, *Physical Review Letters* **63** (aug, 1989) 980–983.

[39] L. Blum, *Mean spherical model for asymmetric electrolytes*, *Molecular Physics* **30** (nov, 1975) 1529–1535, [arXiv:0806.4051].

[40] M. J. Gordon, X. Huang, S. L. Pentoney, and R. N. Zare, *Capillary Electrophoresis*, *Science* **242** (1988), no. 4876 224–228.

[41] A. E. Herr, J. I. Molho, J. G. Santiago, M. G. Mungal, T. W. Kenny, and M. G. Garguilo, *Electroosmotic Capillary Flow with Nonuniform Zeta Potential*, *Analytical Chemistry* **72** (mar, 2000) 1053–1057.

[42] A. Sze, D. Erickson, L. Ren, and D. Li, *Zeta-potential measurement using the Smoluchowski equation and the slope of the current-time relationship in electroosmotic flow.*, *Journal of Colloid and Interface Science* **261** (may, 2003) 402–10.

[43] M. Napoli, J. C. T. Eijkel, and S. Pennathur, *Nanofluidic technology for biomolecule applications: a critical review*, *Lab on a Chip* **10** (2010), no. 8 957–985.

[44] D. Burgreen and F. R. Nakache, *Electrokinetic Flow in Ultrafine Capillary Slits*, *The Journal of Physical Chemistry* **68** (1964), no. 5 1084–1091.

[45] C. L. Rice and R. Whitehead, *Electrokinetic Flow in a Narrow Cylindrical Capillary*, *The Journal of Physical Chemistry* **69** (nov, 1965) 4017–4024.

[46] S. Pennathur and J. G. Santiago, *Electrokinetic transport in nanochannels. 2. Experiments*, *Analytical Chemistry* **77** (2005), no. 21 6782–6789.

[47] R. Bharadwaj and J. G. Santiago, *Dynamics of field-amplified sample stacking*, *Journal of Fluid Mechanics* **543** (nov, 2005) 57–92.

[48] J. M. Sustarich, B. D. Storey, and S. Pennathur, *Field-amplified sample stacking and focusing in nanofluidic channels*, *Physics of Fluids* **22** (nov, 2010) 112003.

[49] A. Wainright, S. J. Williams, G. Ciambrone, Q. Xue, J. Wei, and D. Harris, *Sample pre-concentration by isotachophoresis in microfluidic devices*, *Journal of Chromatography A* **979** (2002), no. 1 69–80.

[50] T. K. Khurana and J. G. Santiago, *Sample Zone Dynamics in Peak Mode Isotachophoresis*, *Anal. Chem.* **80** (aug, 2008) 6300–6307.

[51] A. Plecis, C. Nanteuil, A.-M. Haghiri-Gosnet, and Y. Chen, *Electropreconcentration with Charge-Selective Nanochannels*, *Anal. Chem.* **80** (dec, 2008) 9542–9550.

[52] W.-l. Hsu, D. W. Inglis, M. A. Startsev, E. M. Goldys, M. R. Davidson, and D. J. Harvie, *Isoelectric Focusing in a Silica Nanofluidic Channel: Effects of Electromigration and Electroosmosis*, *Anal. Chem.* **86** (sep, 2014) 8711–8718.

[53] D. Gillespie and S. Pennathur, *Separation of Ions in Nanofluidic Channels with Combined Pressure-Driven and Electro-Osmotic Flow*, *Analytical Chemistry* **85** (mar, 2013) 2991–2998.

[54] A. Hibara, T. Saito, H.-B. Kim, M. Tokeshi, T. Ooi, M. Nakao, and T. Kitamori, *Nanochannels on a Fused-Silica Microchip and Liquid Properties Investigation by Time-Resolved Fluorescence Measurements*, *Anal. Chem.* **74** (dec, 2002) 6170–6176.

[55] N. R. Tas, J. Haneveld, H. V. Jansen, M. Elwenspoek, and A. van den Berg, *Capillary filling speed of water in nanochannels*, *Appl. Phys. Lett.* **85** (oct, 2004) 3274–3276.

[56] J. Haneveld, N. R. Tas, N. Brunets, H. V. Jansen, and M. Elwenspoek, *Capillary filling of sub-10nm nanochannels*, *J. Appl. Phys.* **104** (jul, 2008) 014309.

[57] L. Li, Y. Kazoe, K. Mawatari, Y. Sugii, and T. Kitamori, *Viscosity and Wetting Property of Water Confined in Extended Nanospace Simultaneously Measured from Highly-Pressurized Meniscus Motion*, *J. Phys. Chem. Lett.* **3** (sep, 2012) 2447–2452.

[58] R. Qiao and N. R. Aluru, *Ion concentrations and velocity profiles in nanochannel electroosmotic flows*, *J. Chem. Phys.* **118** (mar, 2003) 4692–4701.

[59] K. Morikawa, Y. Kazoe, K. Mawatari, T. Tsukahara, and T. Kitamori, *Dielectric Constant of Liquids Confined in the Extended Nanospace Measured by a Streaming Potential Method*, *Anal. Chem.* **87** (feb, 2015) 1475–1479.

[60] R. J. Hunter, *Zeta potential in colloid science: Principles and Applications.* Academic Press Limited, London, second ed., 1981.

[61] X. Huang, M. J. Gordon, and R. N. Zare, *Current-monitoring method for measuring the electroosmotic flow rate in capillary zone electrophoresis*, *Analytical Chemistry* **60** (sep, 1988) 1837–1838.

[62] T. Driehorst, P. O'Neill, P. M. Goodwin, S. Pennathur, and D. K. Fygenson, *Distinct Conformations of DNA-Stabilized Fluorescent Silver Nanoclusters Revealed by Electrophoretic Mobility and Diffusivity Measurements.*, *Langmuir* **27** (jul, 2011) 8923–33.

[63] D. Mampallil, D. van den Ende, and F. Mugele, *A simple method to determine the surface charge in microfluidic channels*, *Electrophoresis* **31** (jan, 2010) 563–9.

[64] A. Lenzi, F. Viola, F. Bonotto, J. Frey, M. Napoli, and S. Pennathur, *Method to determine the effective ζ potential in a microchannel with an embedded gate electrode*, *Electrophoresis* **32** (nov, 2011) 3295–304.

[65] S. Devasenathipathy, R. Bharadwaj, and J. G. Santiago, *Investigation of internal pressure gradients generated in electrokinetic flows with axial conductivity gradients*, *Experiments in Fluids* **43** (nov, 2007) 959–967.

[66] C. McCallum and S. Pennathur, *Accounting for electric double layer and pressure gradient-induced dispersion effects in microfluidic current monitoring*, *Microfluidics and Nanofluidics* **20** (jan, 2016) 13.

[67] C.-O. Ng and P. Suvadip, *On the time development of dispersion in electroosmotic flow through a rectangular channel*, *Acta Mech. Sin.* **28** (2012), no. 3 631–643.

[68] V. G. Levich, S. Technica, *et. al.*, *Physicochemical hydrodynamics*, vol. 689. Prentice-hall Englewood Cliffs, NJ, 1962.

[69] Y.-w. Liu, S. Pennathur, and C. D. Meinhart, *Electrophoretic mobility of a spherical nanoparticle in a nanochannel*, *Physics of Fluids* **26** (nov, 2014) 112002.

[70] J.-P. Hsu and C.-H. Huang, *Analytical expressions for pH-regulated electroosmotic flow in microchannels*, *Colloids and Surfaces B: Biointerfaces* **93** (may, 2012) 260–262.

[71] F. Baldessari, *Electrokinetics in nanochannels: Part II. Mobility dependence on ion density and ionic current measurements*, *Journal of Colloid and Interface Science* **325** (sep, 2008) 539–546.

[72] K. L. Jensen, J. T. Kristensen, A. M. Crumrine, M. B. Andersen, H. Bruus, and S. Pennathur, *Hydronium-dominated ion transport in carbon-dioxide-saturated electrolytes at low salt concentrations in nanochannels*, *Physical Review E* **83** (may, 2011) 056307.

[73] G. Taylor, *Dispersion of Soluble Matter in Solvent Flowing Slowly through a Tube*, *Proceedings of the Royal Society A: Mathematical, Physical and Engineering Sciences* **219** (aug, 1953) 186–203.

[74] R. Aris, *On the Dispersion of a Solute in a Fluid Flowing through a Tube*, *Proceedings of the Royal Society A: Mathematical, Physical and Engineering Sciences* **235** (apr, 1956) 67–77.

[75] R. Datta and V. R. Kotamarthi, *Electrokinetic dispersion in capillary electrophoresis*, *AIChE Journal* **36** (jun, 1990) 916–926.

[76] I. Frankel and H. Brenner, *On the foundations of generalized Taylor dispersion theory*, *J. Fluid Mech.* **204** (1989) 97–119.

[77] S. K. Griffiths and R. H. Nilson, *Hydrodynamic Dispersion of a Neutral Nonreacting Solute in Electroosmotic Flow*, *Analytical Chemistry* **71** (dec, 1999) 5522–5529.

[78] S. K. Griffiths and R. H. Nilson, *Electroosmotic Fluid Motion and Late-Time Solute Transport for Large Zeta Potentials*, *Analytical Chemistry* **72** (oct, 2000) 4767–4777.

[79] A. Ajdari, N. Bontoux, and H. A. Stone, *Hydrodynamic Dspersion in Shallow Microchannels: the Effect of Cross-Sectional Shape*, *Analytical Chemistry* **78** (jan, 2006) 387–92.

[80] E. K. Zholkovskij and J. H. Masliyah, *Hydrodynamic Dispersion due to Combined Pressure-Driven and Electroosmotic Flow Through Microchannels with a Thin Double Layer*, *Analytical Chemistry* **76** (2004), no. 10 2708–2718.

[81] D. E. Huber and J. G. Santiago, *Taylor-Aris dispersion in temperature gradient focusing.*, *Electrophoresis* **28** (jul, 2007) 2333–44.

[82] D. E. Huber and J. G. Santiago, *Ballistic dispersion in temperature gradient focusing*, *Proceedings of the Royal Society A* **464** (mar, 2008) 595–612.

[83] G. M. Torrie and J. P. Valleau, *Electrical Double Layers. IV. Limitations of the Gouy-Chapman Theory*, *Journal of Physical Chemistry* **86** (1982), no. 16 3251–3257.

[84] F. H. J. van der Heyden, D. Stein, K. Besteman, S. G. Lemay, and C. Dekker, *Charge Inversion at High Ionic Strength Studied by Streaming Currents*, *Physical Review Letters* **96** (jun, 2006) 224502.

[85] Y. He, D. Gillespie, D. Boda, I. Vlassiouk, R. S. Eisenberg, and Z. S. Siwy, *Tuning Transport Properties of Nanofluidic Devices with Local Charge Inversion*, *Journal of the American Chemical Society* **131** (apr, 2009) 5194–5202.

[86] S. Prakash, H. A. Zambrano, M. Fuest, C. Boone, E. Rosenthal-Kim, N. Vasquez, and A. T. Conlisk, *Electrokinetic transport in silica nanochannels with asymmetric surface charge*, *Microfluidics and Nanofluidics* **19** (dec, 2015) 1455–1464.

[87] H. A. Zambrano, N. Vásquez, and E. Wagemann, *Wall embedded electrodes to modify electroosmotic flow in silica nanoslits*, *Phys. Chem. Chem. Phys.* **18** (2016), no. 2 1202–1211.

[88] P. Crisalli, C. McCallum, and S. Pennathur, *Label free detection of nucleic acids by modulating nanochannel surfaces*, *Chem. Commun.* **51** (2015), no. 12 2335–2338.

[89] C. McCallum, Y. Lin, J. D. Rutte, I. Chen, and S. Pennathur, *Confinement Effects on Non-Equilibrium Dna Hybridization in Micro and Nanofluidic Channels*, in *20th International Conference on Miniaturized Systems for Chemistry and Life Sciences*, (Dublin, Ireland), pp. 1436–1437, 2016.

[90] J. Loessberg-Zahl, K. G. H. Janssen, C. McCallum, D. Gillespie, and S. Pennathur, *(Almost) Stationary Isotachophoretic Concentration Boundary in a Nanofluidic Channel Using Charge Inversion*, *Analytical Chemistry* **88** (jun, 2016) 6145–6150.

[91] D. Henderson, *Bioterrorism as a Public Health Threat*, *Emerging Infectious Diseases* **4** (1998), no. 3 488–492.

[92] O. Lazcka, F. J. D. Campo, and F. X. Muñoz, *Pathogen detection: A perspective of traditional methods and biosensors*, *Biosensors and Bioelectronics* **22** (2007), no. 7 1205–1217.

[93] R. A. Halvorson and P. J. Vikesland, *Surface-Enhanced Raman Spectroscopy (SERS) for Environmental Analyses*, *Environmental Science Technology* **44** (2010), no. 20 7749–7755.

[94] S. S. Iqbal, M. W. Mayo, J. G. Bruno, B. V. Bronk, C. A. Batt, and J. P. Chambers, *A review of molecular recognition technologies for detection of biological threat agents*, *Biosensors and Bioelectronics* **15** (2000), no. 11-12 549–578.

[95] B. Lam, J. Das, R. D. Holmes, L. Live, A. Sage, E. H. Sargent, and S. O. Kelley, *Solution-based circuits enable rapid and multiplexed pathogen detection*, *Nature Communications* **4** (2013), no. June 2001.

[96] J. Clarke, H.-C. Wu, L. Jayasinghe, A. Patel, S. Reid, and H. Bayley, *Continuous base identification for single-molecule nanopore DNA sequencing*, *Nature Nanotechnology* **4** (2009), no. 4 265–270.

[97] X. Wang and S. Smirnov, *Label-Free DNA Sensor Based on Surface Charge Modulated Ionic Conductance*, *ACS Nano* **3** (apr, 2009) 1004–1010.

[98] R. Y. Lai, E. T. Lagally, S.-H. Lee, H. T. Soh, K. W. Plaxco, and A. J. Heeger, *Rapid, sequence-specific detection of unpurified PCR amplicons via a reusable, electrochemical sensor*, *Proceedings of the National Academy of Sciences of the United States of America* **103** (2006), no. 11 4017–4021.

[99] D. C. Martins, V. Chu, and J. P. Conde, *The effect of the surface functionalization and the electrolyte concentration on the electrical conductance of silica nanochannels*, *Biomicrofluidics* **7** (2013), no. 3 034111.

[100] M. B. Andersen, J. Frey, S. Pennathur, and H. Bruus, *Surface-dependent chemical equilibrium constants and capacitances for bare and 3-cyanopropyldimethylchlorosilane coated silica nanochannels*, *Journal of Colloid and Interface Science* **353** (jan, 2011) 301–310.

[101] H. Deng, V. A. Bloomfield, J. M. Benevides, and G. J. Thomas, *Structural basis of polyamine-DNA recognition: spermidine and spermine interactions with genomic B-DNAs of different GC content probed by Raman spectroscopy.*, *Nucleic Acids Research* **28** (2000), no. 17 3379–3385.

[102] A. Sanchez, T. Ksiazek, P. Rollin, M. Miranda, S. Trappier, A. Khan, C. Peters, and S. Nichols *J. Infect. Dis.* **179** (1999).

[103] A. Macanovic, C. Marquette, C. Polychronakos, and M. F. Lawrence, *Impedance-based detection of DNA sequences using a silicon transducer with PNA as the probe layer*, *Nucleic Acids Research* **32** (2004), no. 2 e20.

[104] M. Berezovski and S. Krylov, *Nonequilibrium capillary Electrophoresis of equilibrium mixtures - A single experiment reveals equilibrium and kinetic parameters of protein-DNA interactions*, *JOURNAL OF THE AMERICAN CHEMICAL SOCIETY* **124** (NOV 20, 2002) 13674–13675.

[105] A. Petrov, V. Okhonin, M. Berezovski, and S. Krylov, *Kinetic capillary Electrophoresis (KCE): A conceptual platform for kinetic homogeneous affinity methods*, *JOURNAL OF THE AMERICAN CHEMICAL SOCIETY* **127** (DEC 7, 2005) 17104–17110.

[106] M. Busch, L. Carels, H. Boelens, J. Kraak, and H. Poppe, *Comparison of five methods for the study of drug-protein binding in affinity capillary Electrophoresis*, *Journal of Chromatography A* **777** (AUG 15, 1997) 311–328.

[107] N. Fang and D. Chen, *Behavior of interacting species in capillary Electrophoresis described by mass transfer equation*, *Analytical Chemistry* **78** (MAR 15, 2006) 1832–1840.

[108] N. Fang, Y. Sun, J. Zheng, and D. D. Y. Chen, *Computer simulation of different modes of ACE based on the dynamic complexation model*, *Electrophoresis* **28** (SEP, 2007) 3214–3222.

[109] V. Andreev, N. Pliss, and P. Righetti, *Computer simulation of affinity capillary Electrophoresis*, *Electrophoresis* **23** (MAR, 2002) 889–895.

[110] V. Okhonin, S. Krylova, and S. Krylov, *Nonequilibrium capillary Electrophoresis of equilibrium mixtures, mathematical model*, *Analytical Chemistry* **76** (MAR 1, 2004) 1507–1512.

[111] S. M. Krylova, P. M. Dove, M. Kanoatov, and S. N. Krylov, *Slow-Dissociation and Slow-Recombination Assumptions in Nonequilibrium Capillary Electrophoresis of Equilibrium Mixtures*, *Analytical Chemistry* **83** (OCT 1, 2011) 7582–7585.

[112] V. Okhonin, A. P. Petrov, M. Berezovski, and S. N. Krylov, *Plug-plug kinetic capillary Electrophoresis: Method for direct determination of rate constants of complex formation and dissociation*, *Analytical Chemistry* **78** (JUL 15, 2006) 4803–4810.

[113] D. E. Huber, M. L. Markel, S. Pennathur, and K. D. Patel, *Oligonucleotide hybridization and free-solution electrokinetic separation in a nanofluidic device*, *Lab on a Chip* **9** (2009), no. 20 2933–2940.

[114] S. Pennathur, F. Baldessari, J. G. Santiago, M. G. Kattah, J. B. Steinman, and P. J. Utz, *Free-Solution Oligonucleotide Separation in Nanoscale Channels*, *Analytical Chemistry* **79** (2007), no. 21 8316–8322.

[115] N. Laachi and K. D. Dorfman, *Theory of band broadening during cycling temperature capillary Electrophoresis*, *Electrophoresis* **28** (FEB, 2007) 665–673.

[116] J. W. Szostak, D. P. Bartel, and P. L. Luisi, *Synthesizing Life*, *Nature* **409** (jan, 2001) 387–390.

[117] M. J. Shon and A. E. Cohen, *Mass action at the single-molecule level*, *Journal of the American Chemical Society* **134** (2012), no. 35 14618–23.

[118] L. Rubinovich and M. Polak, *The Intrinsic Role of Nanoconfinement in Chemical Equilibrium: Evidence from DNA Hybridization*, *Nano Letters* **13** (may, 2013) 2247–2251, [1011.1669].

[119] T. Squires and S. Quake, *Microfluidics: Fluid physics at the nanoliter scale*, *REVIEWS OF MODERN PHYSICS* **77** (JUL, 2005) 977–1026.

[120] B. Rauzan, E. McMichael, R. Cave, L. R. Sevcik, K. Ostrosky, E. Whitman, R. Stegemann, A. L. Sinclair, M. J. Serra, and A. A. Deckert, *Kinetics and Thermodynamics of DNA, RNA, and Hybrid Duplex Formation*, *Biochemistry* **52** (FEB 5, 2013) 765–772.

[121] M. E. Craig, D. M. Crothers, and P. Doty, *Relaxation Kinetics of Dimer Formation by Self-Complementary Oligonucleotides*, *Journal of Molecular Biology* **62** (1971), no. 2 383–&.

[122] M. Mammen, I. Colton, J. Carbeck, R. Bradley, and G. Whitesides, *Representing primary electrophoretic data in the 1/time domain: Comparison to representations in the time domain*, *Analytical Chemistry* **69** (JUN 1, 1997) 2165–2170.

[123] E. Stellwagen and N. Stellwagen, *Determining the electrophoretic mobility and translational diffusion coefficients of DNA molecules in free solution*, *Electrophoresis* **23** (AUG, 2002) 2794–2803.

[124] E. Stellwagen and N. Stellwagen, *The free solution mobility of DNA in Tris-acetate-EDTA buffers of different concentrations, with and without added NaCl*, *Electrophoresis* **23** (JUN, 2002) 1935–1941.

[125] J. Noble, L. Wang, K. Cole, and A. Gaigalas, *The effect of overhanging nucleotides on fluorescence properties of hybridising oligonucleotides labelled with Alexa-488 and FAM fluorophores*, *BIOPHYSICAL CHEMISTRY* **113** (MAR 1, 2005) 255–263.

[126] S. Marras, F. Kramer, and S. Tyagi, *Efficiencies of fluorescence resonance energy transfer and contact-mediated quenching in oligonucleotide probes*, *NUCLEIC ACIDS RESEARCH* **30** (NOV 1, 2002).

[127] M. Gong, K. R. Wehmeyer, P. A. Limbach, and W. R. Heineman, *Unlimited-volume electrokinetic stacking injection in sweeping capillary electrophoresis using a cationic surfactant*, *Analytical Chemistry* **78** (SEP 1, 2006) 6035–6042.

[128] C. Zhang and W. Thormann, *Head-column field-amplified sample stacking in binary system capillary electrophoresis: A robust approach providing over 1000-fold sensitivity enhancement*, *Analytical Chemistry* **68** (AUG 1, 1996) 2523–2532.

[129] F. M. Everaerts, J. L. Beckers, and T. P. E. M. Verheggen, *Isotachophoresis: Theory, Instrumentation, and Applications*. Elsevier Scientific Publishing Company, Amsterdam, 1976.

[130] B. Y. Moghadam, K. T. Connelly, and J. D. Posner, *Isotachophoretic Preconcenetration on Paper-Based Microfluidic Devices*, *ANALYTICAL CHEMISTRY* **86** (JUN 17, 2014) 5829–5837.

[131] J. Reijenga, G. Aben, T. Verheggen, and F. Everaerts, *Effect of electroosmosis on detection in isotachophoresis*, *Journal of Chromatography A* **260** (1983) 241 – 254.

[132] C. A. Keely, R. R. Holloway, T. A. M. Vandegoor, and D. McManigill, *Dispersion in Capillary Electrophoresis with External Flow-Control Methods*, *Journal of Chromatography A* **652** (OCT 15, 1993) 283–289. 5TH International Symposium on High Performance Capillary Electrophoresis (HPCE 93), Orlando, FL, JAN 25-28, 1993.

[133] M. C. Breadmore, *Unlimited-volume stacking of ions in capillary electrophoresis. Part 1: Stationary isotachophoretic stacking of anions*, *Electrophoresis* **29** (MAR, 2008) 1082–1091.

[134] M. Tavares, R. Colombara, and S. Massaro, *Modified electroosmotic flow by cationic surfactant additives in capillary electrophoresis - Evaluation of electrolyte systems for anion analysis*, *Journal of Chromatography A* **772** (JUN 6, 1997) 171–178. 10th International Symposium on Capillary Electrophoresis and Isotachophoresis (ITP 96), Prague, Czech Republic, SEP 17-20, 1996.

[135] G. Danger, R. Pascal, and H. Cottet, *On-line sample stacking of peptides in capillary electrophoresis for the study of prebiotic reactions between alpha,alpha-dialkylated amino acids and amino acid N-carboxyanhydrides*, *Journal of Chromatography A* **1216** (JUL 24, 2009) 5748–5754.

[136] S. D. Noblitt, L. R. Mazzoleni, S. V. Hering, J. L. Collett, Jr., and C. S. Henry, *Separation of common organic and inorganic anions in atmospheric aerosols using a piperazine buffer and capillary electrophoresis*, *JOURNAL OF CHROMATOGRAPHY A* **1154** (JUN 22, 2007) 400–406.

[137] T. Soga, Y. Ueno, H. Naraoka, Y. Ohashi, M. Tomita, and T. Nishioka, *Simultaneous determination of anionic intermediates for Bacillus subtilis metabolic pathways by capillary electrophoresis electrospray ionization mass spectrometry*, *Analytical Chemistry* **74** (MAY 15, 2002) 2233–2239.

[138] M. HAYES and A. EWING, *Electroosmotic Flow-Control and Monitoring with an Applied Radial Voltage for Capillary Zone Electrophoresis*, *Analytical Chemistry* **64** (MAR 1, 1992) 512–516.

[139] J. Hoffmann and D. Gillespie, *Ion Correlations in Nanofluidic Channels: Effects of Ion Size, Valence, and Concentration on Voltage- and Pressure-Driven Currents*, *Langmuir* **29** (jan, 2013) 1303–1317.

[140] G. Danger, R. Pascal, and H. Cottet, *Non-uniform surface charge distributions in CE: Theoretical and experimental approach based on Taylor dispersion*, *Electrophoresis* **29** (NOV, 2008) 4226–4237.

[141] F. Kohlrausch, *Ueber concentrations-verschiebungen durch electrolyse im inneren von lsungen und lsungsgemischen*, *Annalen der Physik* **298** (1897), no. 10 209–239.

[142] D. R. Lide, *CRC Handbook of Chemistry and Physics, 88th ed.* CRC Press, Boca Raton, FL, 2007.

[143] A. Persat, M. E. Suss, and J. G. Santiago, *Basic principles of electrolyte chemistry for microfluidic electrokinetics. Part II: Coupling between ion mobility, electrolysis, and acid-base equilibria*, *Lab on a Chip* **9** (sep, 2009) 2454–69.

[144] M. C. Breadmore and J. P. Quirino, *100 000-fold concentration of anions in capillary zone electrophoresis using electroosmotic flow controlled counterflow isotachophoretic stacking under field amplified conditions*, *Analytical Chemistry* **80** (AUG 15, 2008) 6373–6381.

[145] M. Bercovici, C. M. Han, J. C. Liao, and J. G. Santiago, *Rapid hybridization of nucleic acids using isotachophoresis*, *Proceedings of the National Academy of Sciences of the United States of America* **109** (JUL 10, 2012) 11127–11132.

[146] A. Ajdari, *Electro-Osmosis on Inhomogeneously Charged Surfaces*, *Physical Review Letters* **75** (1995), no. 4 755–759.

[147] A. S. Khair and T. M. Squires, *Surprising consequences of ion conservation in electro-osmosis over a surface charge discontinuity*, *Journal of Fluid Mechanics* **615** (2008) 323.

[148] M. M. Hatlo and L. Lue, *Electrostatic interactions of charged bodies from the weak- to the strong-coupling regime*, *EPL (Europhysics Letters)* **89** (jan, 2010) 25002, [0806.3716].

[149] K. Bohinc, G. Volpe Bossa, S. Gavryushov, and S. May, *Poisson-Boltzmann model of electrolytes containing uniformly charged spherical nanoparticles*, *The Journal of Chemical Physics* **145** (dec, 2016) 234901.

[150] L. J. D. Frink and A. G. Salinger, *Two- and Three-Dimensional Nonlocal Density Functional Theory for Inhomogeneous Fluids*, *Journal of Computational Physics* **159** (apr, 2000) 407–424.

[151] M. Valiskó, D. Boda, and D. Gillespie, *Selective Adsorption of Ions with Different Diameter and Valence at Highly Charged Interfaces*, *The Journal of Physical Chemistry C* **111** (nov, 2007) 15575–15585.

[152] D. Gillespie, A. S. Khair, J. P. Bardhan, and S. Pennathur, *Efficiently accounting for ion correlations in electrokinetic nanofluidic devices using density functional theory*, *Journal of Colloid and Interface Science* **359** (jul, 2011) 520–529.

[153] D. Gillespie, *High Energy Conversion Efficiency in Nanofluidic Channels*, *Nano Letters* **12** (mar, 2012) 1410–1416.

[154] W. Press, S. Teukolsky, W. Vetterling, and B. Flannery, *Numerical Recipes - The Art of Scientific Computing*. Cambridge University Press, Cambridge, 3rd ed., 2007.

[155] G. M. Torrie and J. P. Valleau, *Electrical Double Layers. I. Monte Carlo Study of a Uniformly Charged Surface*, *The Journal of Chemical Physics* **73** (1980), no. 11 5807–5816.

[156] R. Qiao and N. R. Aluru, *Charge Inversion and Flow Reversal in a Nanochannel Electro-osmotic Flow*, *Physical Review Letters* **92** (may, 2004) 198301.

[157] S. L. Carnie and G. M. Torrie, *The Statistical Mechanics of the Electrical Double Layer*, in *Journal of Electroanalytical Chemistry and Interfacial Electrochemistry*, vol. 150, pp. 141–253. jul, 1983.

[158] C. McCallum, S. Pennathur, and D. Gillespie, *Two-Dimensional Electric Double Layer Structure with Heterogeneous Surface Charge*, *Langmuir* (2017). Article ASAP.